KEK Proceedings 2006-4
November 2006
R

Proceedings of the Thirteenth EGS Users' Meeting in Japan

August 8 - 10, 2006.

KEK, Tsukuba, Japan

Edited by

Y. Namito, H. Hirayama and S. Ban

High Energy Accelerator Research Organization

FOREWARD

The Thirteenth EGS Users' Meeting in Japan was held at High Energy Accelerator Research Organization (KEK) from August 8 to 10. The meeting has been hosted by the Radiation Science Center. More than 100 participants attended the meeting.

The meeting was divided into two parts. Short course on EGS was held at the first half of the workshop using EGS5 code. In the later half, 17 talks related EGS were presented. The talk covered the wide fields, like the medical application and the calculation of various detector responses *etc.* These talks were very useful to exchange the information between the researchers in the different fields.

Finally, we would like to express our great appreciation to all authors who have prepared manuscript quickly for the publication of this proceedings.

Hideo Hirayama
Yoshihito Namito
Syuichi Ban
Radiation Science Center
KEK, High Energy Accelerator Research Organization

CONTENTS

AUTOMATED ELECTRON STEP SIZE OPTIMIZATION IN EGS5

S. J. Wilderman
University of Michigan, Ann Arbor, MI, USA

Abstract

The transport mechanics algorithm in EGS5 allows for significantly longer electron transport step-sizes (and hence shorter computation times) than those required in EGS4 to obtain similar accuracy in the simulation of identical problems. But as different classes of problems exhibit differing step-size dependencies in all condensed history Monte Carlo electron transport algorithms, selecting the proper electron step-sizes to optimally exploit the speed advantages of EGS5 in all problems can be challenging for novice users. Thus, an empirical method was devised for the initial official release of EGS5-beta (August, 2005) to automatically optimize step-size selection based on a single, material-dependent input parameter related to the size of problem tally regions. For the more recent release of EGS5-beta (March, 2006), the earlier empirical method, based on energy deposition in the so-called "infinite broomstick" problem, was modified to provide higher accuracy convergence by considering the angular distributions of electrons emerging from the front faces of "finite broomsticks." Additionally, a numerical model for automatically selecting electron energy loss steps was developed and implemented. In this paper we review the general concepts which lead to step-size dependencies in condensed history electron transport algorithms, and we describe the empirical models for selecting optimal electron multiple scattering step sizes used in EGS5. We also describe the method used to determine electron energy loss step-sizes, and we comment on a new technique used for modeling the first multiple scattering step of primary electrons.

1 Introduction

Because of approximations inherent in modeling the cumulative effects of large numbers of individual elastic and inelastic scattering collisions as having occurred in single steps, computations using Monte Carlo electron transport programs based on this "condensed history" [1] algorithm exhibit a dependence on the size of the steps that are used in the simulations. Such step-size driven inaccuracies arise primarily from the uncertainty in models used to define the spatial positions $\Delta x, \Delta y$ and s associated with an electron traveling a total tracklength t through a medium, as shown in Figure 1.

Larsen [4] has noted that if the underlying models used in describing energy loss and multiple elastic scattering distributions are valid for small t, this error vanishes as the step-size t is decreased. Since the computational effort required to solve electron transport problems by Monte Carlo is directly related to the number (and therefore the size) of the multiple scattering steps, an "optimal" step-size in a simulation would therefore be the longest one for which the condensed history error is less than the desired accuracy. In practice, optimal selection of step-sizes is difficult because the intricate interplay between electron step-size and accuracy almost always depends on not only the particular quantity of interest being computed, but also on the fineness or granularity of desired output tallies. For example, a simulation of the spatial energy deposition distribution in a voxelized geometry is a much more fine grain simulation than a computation of bulk energy deposited in a large detector module. Optimization of step-size selection is therefore difficult even for expert users, especially in EGS5, which, because of the complete decoupling of multiple scattering and energy loss in the "dual random hinge" methodology [3, 6], requires the specification of four separate step-size parameters, two for the multiple scattering hinge and two for the energy loss hinge. Even acknowledging that step-size selection necessarily requires some input from the user because of it is inherently problem-dependent, it is clear that requiring the specification of four parameters places an undue burden on the user. It is desirable therefore to provide a method for automation of the

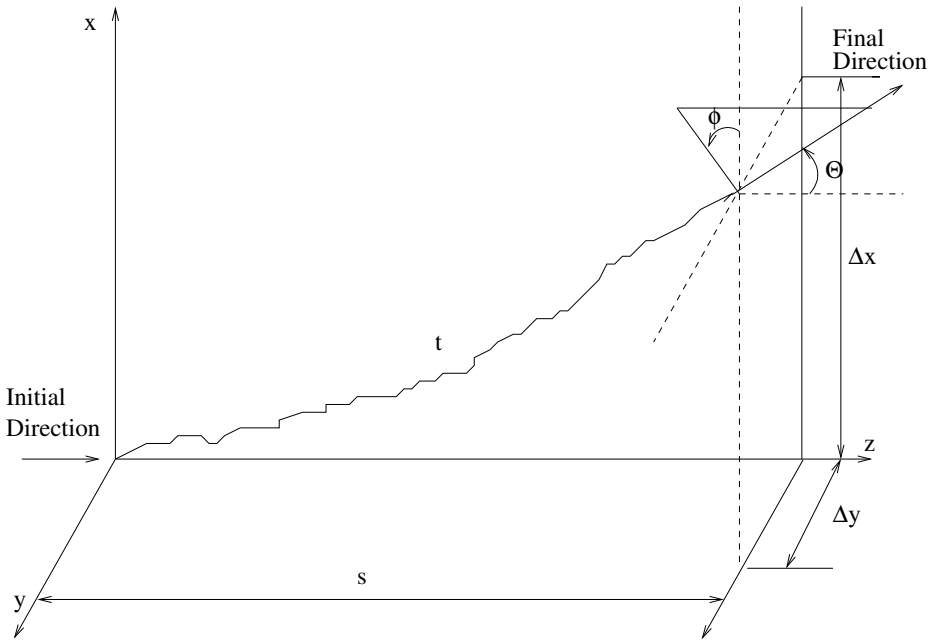

Figure 1: Schematic of electron transport mechanics model.

optimization process with as little input from the user as possible, and so a method for optimization of the multiple scattering hinge step-sizes, based on the dimension of the geometric regions for a given problem, was developed for the EGS5-beta release [6]. In this work we report on a revision to that method, and also present the details of a new method for automatic specification of the energy loss hinge step-size.

2 Multiple Scattering Step-Size Optimization Using Media "Characteristic Dimensions"

The EGS5 model for determining $\Delta x, \Delta y$ and s for an electron traversing a total tracklength t is based on randomly splitting the total track into two segments and applying a scattering "hinge" in between the segments. To accurately account for energy loss over the track [5], the hinge point is not taken randomly in t, but rather randomly in the accumulated scattering strength $K_1(t)$, as given by

$$K_1(t) = \int_0^t dt' G_1(t'). \tag{1}$$

In the above, G_1 is the first transport cross section commonly referred to as the "scattering power," taken from the general formula for the ℓ^{th} transport cross section (or inverse transport mean free path), G_ℓ, which is the ℓ^{th} Legendre moment of the single scattering cross section,

$$G_\ell(t) = 2\pi \int_{-1}^{1} d\mu \Sigma(\mu; t)[1 - P_\ell(\mu)]. \tag{2}$$

Here $\Sigma(\mu; t)$ is the spatially dependent macroscopic single elastic scattering cross section and μ is $\cos(\Theta)$. Thus when we talk about optimizing step-size selection we actually mean that we seek a method for determining the optimal value of K_1, the initial scattering strength, rather the tracklengths t.

Perhaps the most severe test of a Monte Carlo program's electron transport algorithm is the "broomstick" problem, in which electrons normally incident on the planar faces of semi-infinite

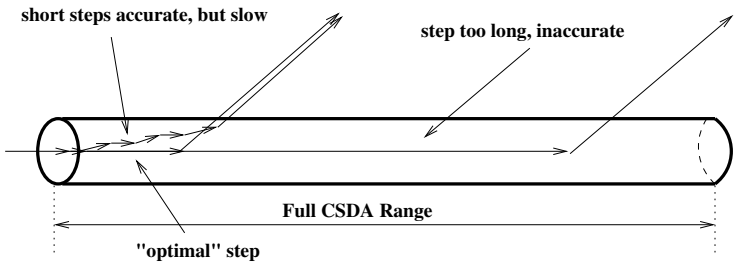

Figure 2: Schematic illustrating the "broomstick" problem.

right-circular cylinders of progressive smaller radii (to isolate the effects of the transport mechanics, hard-collisions are usually ignored in this problem) are simulated. For cylinders of radii approaching infinitesimal thinness, the average total tracklength of incident electrons before they scatter out of the cylinder is given by the single elastic scattering mean-free path, and any Monte Carlo algorithm using a larger step-size would over-estimate the penetration (and hence average total tracklength) in the cylinder. It should be clear then that for cylinders with arbitrary radii, if we begin with results generated by using very small step-sizes and then gradually increase the steps, we will eventually encounter divergence in the computed average electron track-length inside the cylinder, as our model will at some point over-estimate the penetration prior to deflection out toward the sides of the "broomstick." This is illustrated in Figure 2.

Since spatial energy deposition profiles are essentially maps of region-dependent electron tracklengths, and because most problem tallies will be correct if the spatial distribution of electron tracklengths is correct, the largest value of scattering strength K_1 which produces converged results for energy deposition for a given material in a reference geometric volume was initially chosen to be the standard for the EGS5 step-size selection algorithm. Subsequent studies showed, however, that many problems require a more stringent measure of electron tracks than average length, and so a standard based on the average position of track end points for electrons traversing geometric volumes of given reference sizes was adopted. In this new adaptation, instead of computing energy deposition in semi-infinite cylinders, we look at the average lateral deflection $\langle r \rangle$ of electrons emerging from the far face of cylinders with lengths L equal to their diameters D. Values of $\langle r \rangle$ over finite cylinders are clearly more sensitive to multiple scattering step-sizes than values of $\langle t \rangle$, leading to more conservative estimates of the maximum permitted scattering strength and thus better assuring accurate results for problems other than those involving energy deposition.

Using this criteria for defining accuracy, tables of the material and energy dependent values of the largest scattering strengths K_1 yielding, for volumes of a given size, values of $\langle r \rangle$ which are within 1% of the converged results for small K_1 were compiled. Given this data, EGS5 is able to provide a step-size control mechanism based on a single user input parameter in units of length which characterizes the geometric granularity of the problem tallies. This value is called the "characteristic dimension" for the problem, and is set in the user's `MAIN` program by specifying a non-zero value of the variable `CHARD`, which is material dependent. Given this parameter, EGS5 automatically selects the optimal energy dependent values of K_1 by interpolating the compiled data tables of maximum scattering strengths in dimension, material and energy. The tables range in energy from 2 keV[1] up to 1 TeV at values of 2, 3, 5, 7 and 10 in each of the 9 energy decades spanning the energy range. The characteristic geometric dimensions in the data sets range from 10^{-6} times the electron CSDA range at the low end, and up to half of the CSDA range at the high end[2]. (Note that ignoring hard collisions and using unrestricted stopping powers at the upper

[1]For high Z materials for which the Bethe stopping power formula is inaccurate at 2 keV, the tables stop at 10 keV.

[2]An additional constraint on the minimum characteristic dimension in EGS5 is the smallest pathlength for which

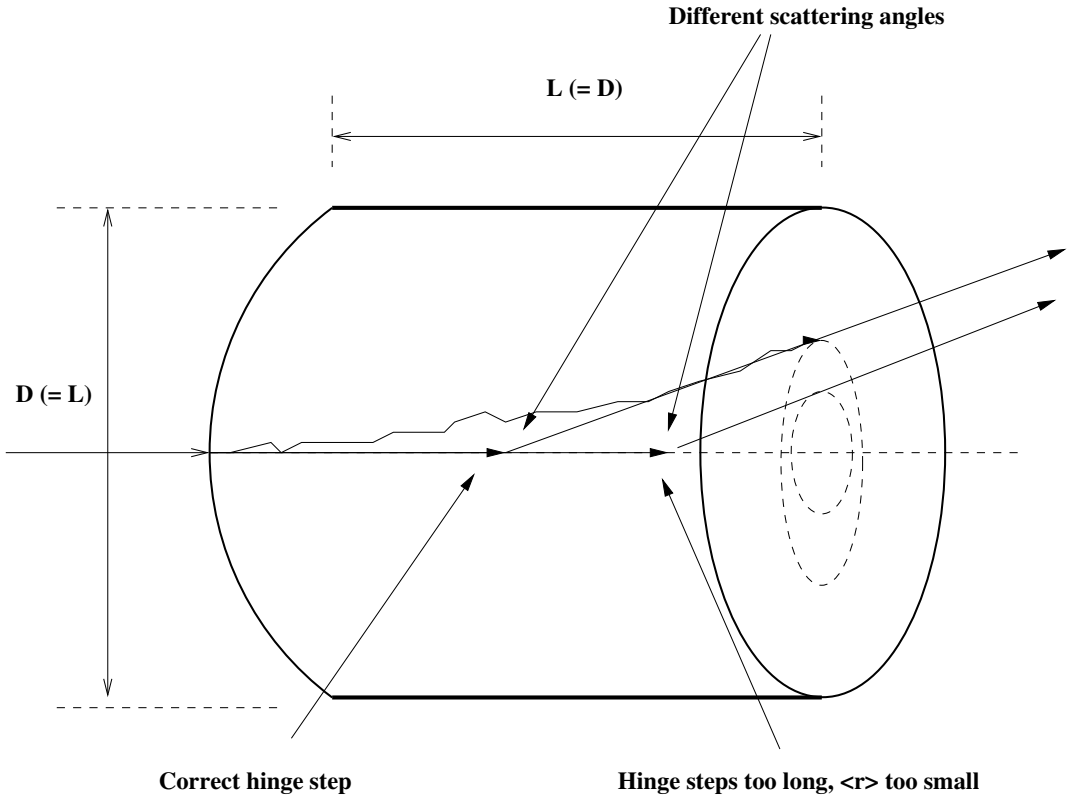

Figure 3: Schematic illustrating the modified "broomstick" problem as used in EGS5.

end of the energy range in question is physically unrealistic. Computations in this energy range were made nonetheless to fill out the tables with overly-conservative estimates of the appropriate step-size.)

Because K_1 is the integral over distance of scattering power, which is proportional to $\rho Z^2/A$ times the integral of the shape of the differential elastic scattering cross section, K_1 should be roughly proportional to $t\rho Z^2/A$, if t is the distance, and that was generally found to be the case. Interpolation in the geometric dimension variable is therefore done in terms of $t\rho$ so that interpolation between materials can be performed in terms of Z^2/A^3. Positron K_1 values are determined by scaling electron scattering strength by the ratio of the positron and electron scattering power. The list of reference materials is given in Table 1.

To generate the data sets, then, for each of the 16 reference materials, 45 reference energies, and 29 broomstick lengths and diameters (*i.e.*, characteristic dimension) a series of Monte Carlo simulations were performed, using up to 25 different values of fractional energy loss (called `EFRACH` in EGS5), covering the range from 30% to 0.001% (except when such steps exceeded the theoretical lower limits of the Molière distribution). Energy loss hinges were set to the lesser of `EFRACH` and 4% fractional energy loss, and 100,000 histories were simulated, resulting in relative statistical uncertainties in the computed values of $\langle r \rangle$ at 2σ of around 0.3%. Tallies were made of the the average track length inside the volume, the average lateral displacement of the particles escaping the end of the volume, the average longitudinal displacement of particles escaping the sides of

the Molière multiple scattering distribution produces viable results. Bethe [2] has suggested that paths which encompass at least 20 elastic scattering collisions are necessary, though EGS5 will compute the distribution using as few as e collisions, which is a numerical limit that simply assures positivity.

[3]To account for the effect of soft collision electron scattering, interpolations are actually done in terms of $Z(Z+1)$ instead of Z.

Table 1: Materials used in reference tables of scattering strength vs. characteristic dimension at various energies.

Material	Z	$Z(Z+1)$	A	ρ	$Z(Z+1)/A$
Li	3	12	6.93900	0.5340	1.7294
C	6	42	12.01115	2.2600	3.4968
H_2O	10	76	18.01534	1.0000	4.2186
Al	13	182	26.98150	2.7020	6.7454
S	16	272	32.06435	2.0700	8.4829
Ti	22	506	47.90000	4.5400	10.5637
Cu	29	870	63.54000	8.9333	13.6922
Ge	32	1056	72.59000	5.3600	14.5475
Zr	40	1640	91.22000	6.4000	17.9785
Ag	47	2256	107.87000	10.5000	20.9141
La	57	3306	138.91000	6.1500	23.7996
Gd	64	4160	157.25000	7.8700	26.4547
Hf	72	5256	178.49000	11.4000	29.4470
W	74	5550	183.85000	19.3000	30.1877
Au	79	6320	196.98700	19.3000	32.0833
U	92	8556	232.03600	18.9000	36.8736

the broomstick, and the fractional energy deposited, backscattered and escaping from the side of the broomstick. Computations of the number of hinges expected for the scattering strength being tested given the broomstick dimension, were also made for each run, and the anticipated number of collisions per hinge were also determined and stored.

Illustrative plots showing the divergence in the results as step-sizes are increased in Copper at 5 MeV for several different broomstick thicknesses are shown in Figures 4 (results of energy deposition) and 5 (results of lateral spread).

Approximately 20,000 such plots were generated from over 500,000 simulations to encompass the desired ranges of materials, energies, and characteristic dimensions. The data was then analyzed to determine the maximum fractional energy loss which showed convergence within the statistical uncertainty of the data, using a least-squares fit to a line with slope zero and intercept given by the converged value at short paths. The initial scattering strengths K_1 corresponding to the determined maximum fractional energy losses were computed using Equation 1 cast in terms of an integral over energy instead of over pathlength,

$$K_1(E_0) = \int_{E_1}^{E_0} dE' G_1(E') \left|\frac{dE}{dx}\right|^{-1}, \tag{3}$$

where E_0 is the initial energy, E_1 the energy after the determined maximum fractional energy loss, G_1 the scattering strength and $\left|\frac{dE}{dx}\right|$ the stopping power of the medium. Plots of these maximum values of K_1 to assure convergence as a function of broomstick diameter for several energies in titanium are shown in Figure 6.

The expected nearly linearly relationship between K_1 and t and the appropriate scaling of K_1 with E is clearly evident in Figure 6. We also see in that figure, however, several artifacts of our method. First, we see that our estimation process did not always produce monotonic results, primarily because of noise in the data due to the Monte Carlo statistics (given the large number of runs, some outlier points were to be expected). Additionally, the plots exhibit some discrete jumps

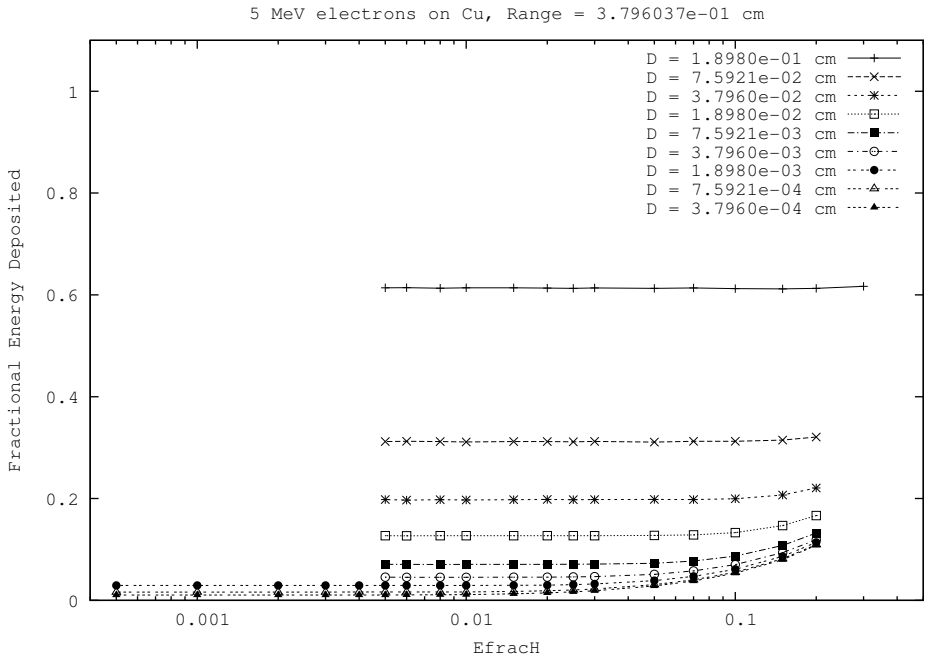

Figure 4: Convergence of energy deposition as a function of step-size (in terms of fractional energy loss) for the broomstick problem with varying diameters D in copper at 5 MeV.

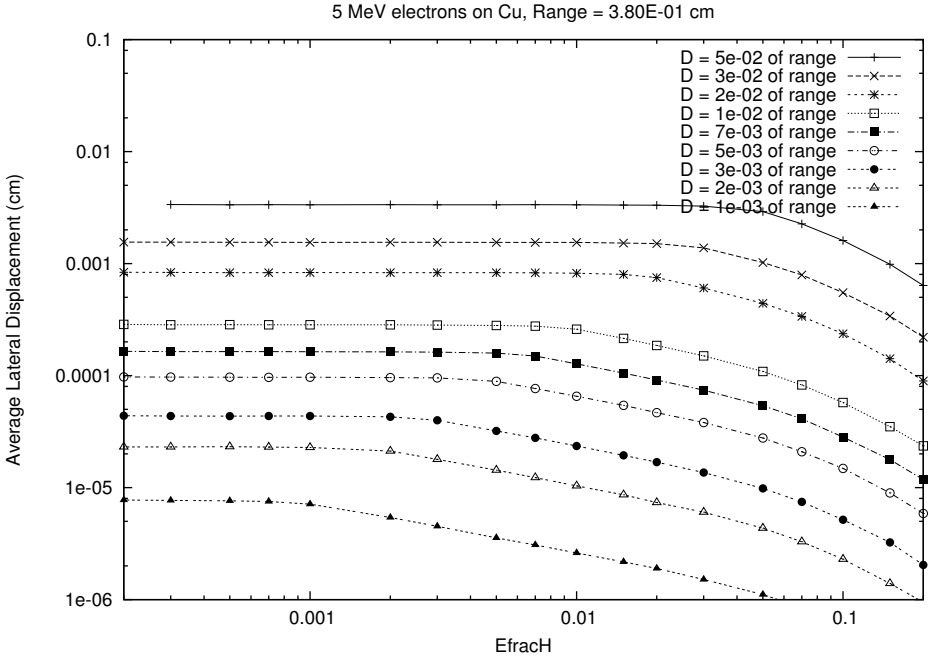

Figure 5: Convergence of average lateral displacement as function of step-size (in terms of fractional energy loss) for the broomstick problem with varying diameters D in copper at 5 MeV.

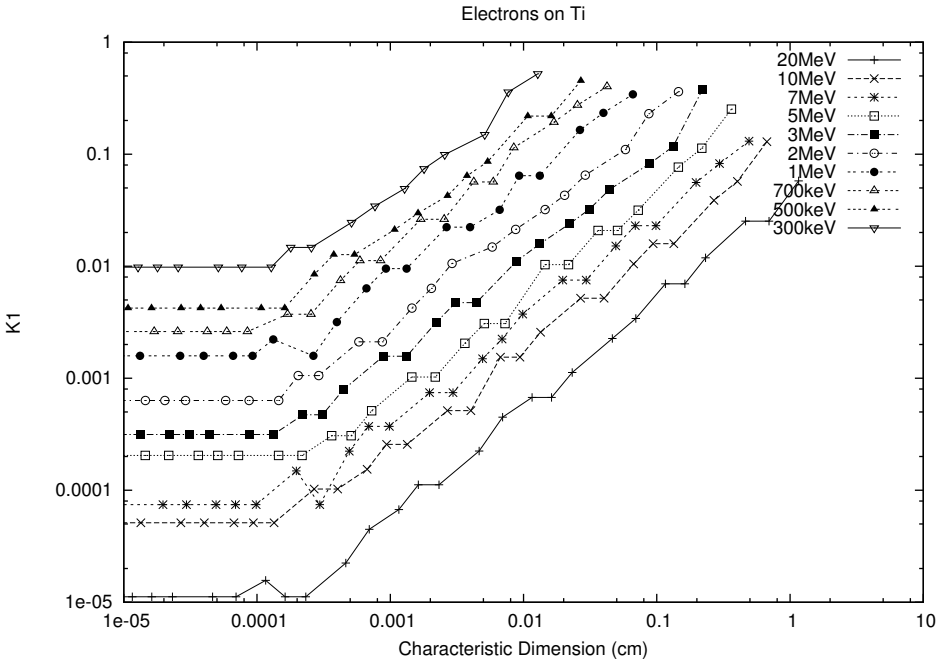

Figure 6: Optimal initial scattering strength K_1 vs. broomstick diameter (equivalent to the characteristic dimension) in titanium at various energies.

because of the finite number of possible K_1 values tested in the parameter study. An additional artifact can be seen in the top plot of Figure 7, which shows converged scattering strength data vs. characteristic dimension for a variety of elements at 100 MeV. Because we limited the test runs to a maximum of 30% fractional energy loss, we see a plateauing of the plots for high energies. Other data sets show a corresponding artifact caused by numerical limits on the minimum step-size at low energies. Note also from Figure 7 that the scaling of K_1 in $Z(Z+1)/A$ rather than Z is evident in the comparison of the plots for water and carbon.

Despite the approximations involved in the definition and determination of convergence, the plots of our computed values of the maximum K_1 which still assures accurate $\langle r \rangle$ as a function of the broomstick dimension exhibits for the most part the behavior we expected. Especially for a given element at a given energy, the log-log K_1 plots can generally be described as being roughly linear in t, though possibly plateauing at either end. Thus each curve (representing one energy for a given element) can be wholly defined by the characteristic dimensions corresponding to the onset (if any) of plateaus at either end, the values of K_1 at those points, and the slope of line on a log-log between those plateau points. All of the curves were inspected numerically and corrected to assure monotonicity, to eliminate the more significant artifacts caused by having a limited set of discrete data points and also to eliminate any physically unrealistic trends in K_1 as a function of t or E for the same material. Using these corrected plots, the five parameters defining each line were determined, with a least squares fit applied to calculate the slopes. The full set of these parameters has been compiled into a single data file `K1.dat` provided with the EGS5 distribution. Thus, for any material, characteristic dimension, and energy, an easy three-way linear interpolation can be performed to determine the appropriate value of K_1. This is done in a new EGS5 routine `RK1` which is called by `HATCH`, and which maps a piece-wise linear fit of $K_1(E)$ onto the same global energy ladder used by the other electron data variables in EGS.

The sample problem `tutor4` included in the EGS5 distribution illustrates the effectiveness of the automated step-size selection method. Table 2 gives the values of reflected and transmitted

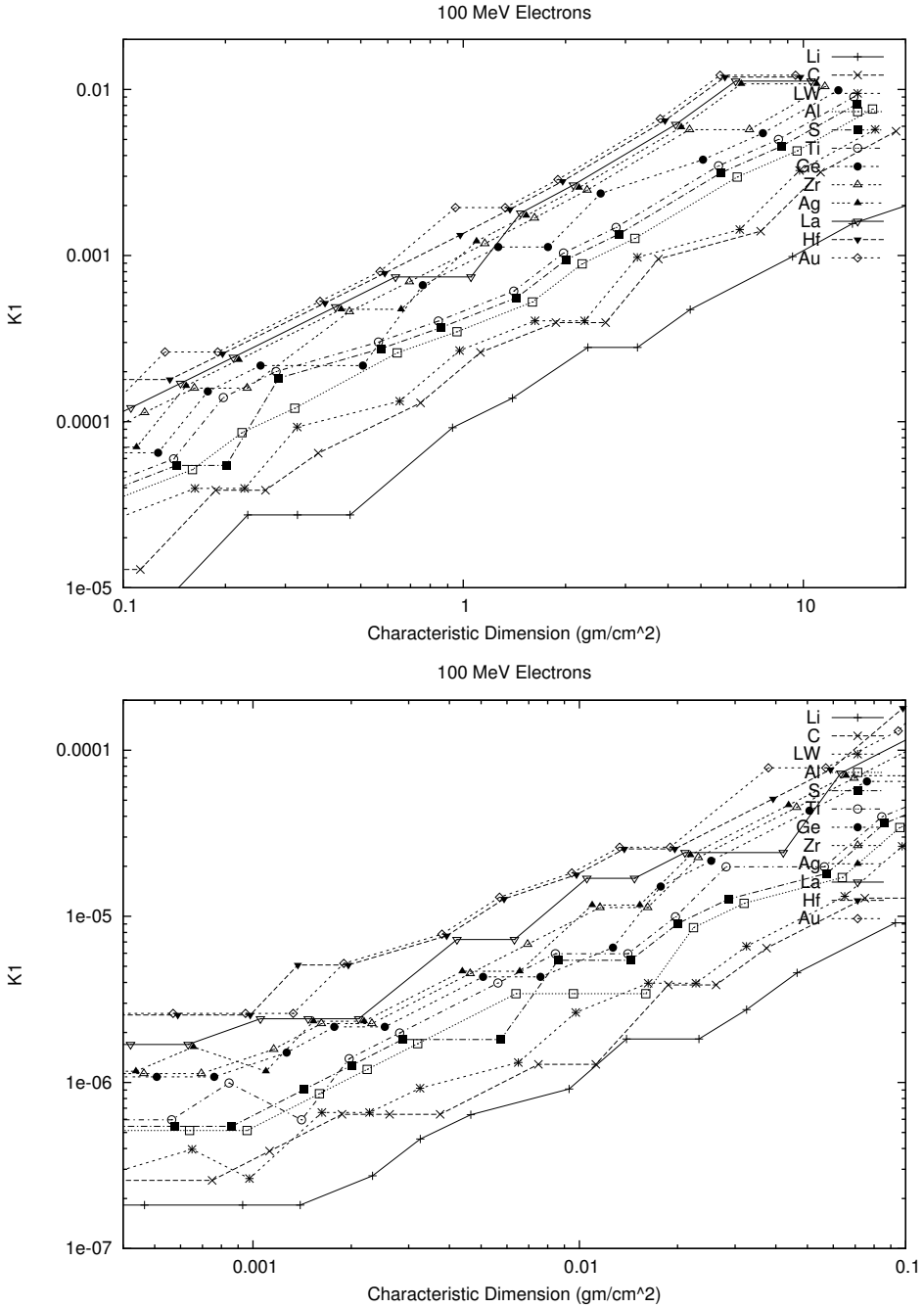

Figure 7: Optimal initial scattering strength K_1 vs. broomstick diameter for various elements at 100 MeV. The upper figure is for values of ρt greater than 0.1, and the lower figure for smaller characteristic dimensions.

Table 2: Reflected and transmitted energy for 2 MeV electrons incident on 2 mm of silicon using EGS4 and EGS5 with various step-sizes

	Reflected E	Transmitted E
EGS4 default	1.3%	49.2%
EGS4 1% `ESTEPE`	6.4%	61.3%
EGS5 30% `ESTEPE`	8.1%	66.5%
EGS5 1% `ESTEPE`	7.3%	64.4%
EGS5 2 mm `charD`	7.4%	64.8%

energy computed for 2 MeV electron beams incident on 2 mm of silicon using various input electron step-sizes with EGS4 and EGS5. Also included are EGS5 results using an input value of 2 mm for the characteristic dimension, which are seen to agree with the EGS5 results using very small step-sizes to within 1%. Note that the results based on the characteristic dimension approach were generated in 1/3 of the CPU time required to generate the small step (1% fractional energy loss per step), illustrating the optimization provided by the new method.

3 Step-Size Specification for Energy Hinges

In the dual hinge formalism of EGS5, the energy steps provide no function other than assuring accurate numerical integration over energy-dependent variables (such as energy loss, scattering strength, *etc.*). For any such quantity f which varies with energy through a step of total length t, if the energy hinge occurs at a distance h, the EGS5 random energy hinge methodology gives for the integration of f over distance variable s through t

$$\begin{aligned} F(t{:}h) &= \int_0^t ds\, f(s) \\ &= h f(E_0) + (t-h) f(E_1) \end{aligned} \tag{4}$$

where E_0 is the initial energy and E_1 the energy at the end of the energy hinge step t. As implemented in EGS5, the energy hinges distances are uniformly distributed in energy, so if ζ is a random number, we have $h = \zeta \Delta E |\frac{dE}{dx}|^{-1}$ and $(t-h) = (1-\zeta)\Delta E |\frac{dE}{dx}|^{-1}$, giving us in practice

$$F(t{:}h) = \zeta \Delta E\, f(E_0) \left|\frac{dE}{dx}\right|_{E_0}^{-1} + (1-\zeta)\Delta E\, f(E_1) \left|\frac{dE}{dx}\right|_{E_1}^{-1} \tag{5}$$

Since the energy hinges are uniformly distributed over t, the average values of the integrated quantities are given by

$$\begin{aligned} \overline{F(t)} &= \int_0^t dh\, F(t{:}h)\, p(h) \\ &= \int_0^1 d\zeta \left(\zeta \Delta E\, f(E_0) \left|\frac{dE}{dx}\right|_{E_0}^{-1} + (1-\zeta)\Delta E\, f(E_1) \left|\frac{dE}{dx}\right|_{E_1}^{-1} \right) \\ &= \frac{\Delta E}{2} \left(f(E_0) \left|\frac{dE}{dx}\right|_{E_0}^{-1} + f(E_1) \left|\frac{dE}{dx}\right|_{E_1}^{-1} \right) \end{aligned} \tag{6}$$

Thus, the random energy hinge step distances are limited by the accuracy which can be achieved in numerically integrating energy dependent quantities of interest using the trapezoid rule. This limit suggests a prescription for determining the energy hinge step-sizes in EGS5: we take t as

the longest step-size which assures that Equation 7 is accurate to within a given tolerance ϵ_{fE} when applied to the integration of the following: the stopping power to compute the energy loss; the scattering power to compute the scattering strength; and the hard collision cross section to compute the hard collision total scattering probability and mean free path. Thus, in general, if $\overline{\Delta F|_{anal}}$ is the analytic integral of one of our functions f over t, we wish to satisfy

$$\overline{\Delta F|_{anal}} - \overline{F(t)} \leq \epsilon_{fE} \tag{7}$$

or

$$\int_0^t ds\, f(t)\Big|_{anal} - \left[\frac{t}{2}\left(f(E_0) + f(E_1)\right)\right] \leq \epsilon_{fE} \tag{8}$$

or

$$\int_{E_0}^{E_1} dE f(E) \left|\frac{dE}{dx}\right|^{-1}\Big|_{anal} - \left[\frac{R_C(E_0) - R_C(E_1)}{2}\left(f(E_0) + f(E_1)\right)\right] \leq \epsilon_{fE} \tag{9}$$

where $R_C(E)$ is the CSDA range for an electron with energy E.

For the scattering strength, the function f is the scattering power G_1, and for energy loss f is the stopping power, in which case the analytical expression reduces simply to ΔE. Note that in the case of the electron mean free path and total scattering probability, the expressions for both the analytical function and the random hinge results are somewhat different from the results described above, as the integrands for those quantities contain the spatial distribution of the collision distances. For the random energy hinge methodology, the probability per unit path of an interaction taking place over a step of length t is given by

$$p(s\!:\!h) = \begin{array}{ll} \Sigma_0 e^{-s\Sigma_0} & s \leq h, \\ \Sigma_1 e^{-h\Sigma_0} e^{-(s-h)\Sigma_1} & s > h \end{array} \tag{10}$$

where h is the hinge distance, Σ_0 the cross section at the initial energy, and Σ_1 the cross section after the energy hinge. The random hinge mean free path over t is then given as

$$\begin{aligned}
\lambda_{Eh}(t) &= \frac{1}{P_{Eh}(t)} \int_0^t ds\, s\, p(s) \qquad (11)\\
&= \frac{1}{P_{Eh}(t)} \int_0^t ds\, s \int_0^s dh\, p(s\!:\!h)\, p(h) \\
&= \frac{1}{P_{Eh}(t)} \int_0^t ds\, s \int_0^s dh \left[\frac{\Sigma_0(t-s)}{st} e^{-s\Sigma_0} + \frac{\Sigma_1}{t} e^{-h\Sigma_0} e^{-(s-h)\Sigma_1}\right] \\
&= \frac{1}{P_{Eh}(t)} \int_0^t ds\, s \left[\frac{\Sigma_0(t-s)}{t} e^{-s\Sigma_0} + \frac{\Sigma_1 e^{-s\Sigma_1}\left(1 - e^{-s(\Sigma_0 - \Sigma_1)}\right)}{t(\Sigma_0 - \Sigma_1)}\right] \\
&= \frac{1}{P_{Eh}(t)} \left[\frac{1}{\Sigma_0} - \frac{e^{-t\Sigma_1}\left(1 - e^{-t(\Sigma_0 - \Sigma_1)}\right)}{(\Sigma_0 - \Sigma_1)}\left(1 + \frac{1}{t\Sigma_1}\right) + \frac{(\Sigma_0 - \Sigma_1)\left(1 - e^{-t\Sigma_0}\right)}{t\Sigma_0^2 \Sigma_1}\right]
\end{aligned}$$

where $P_{Eh}(t)$ is the probability that there is a hard collision of any kind over t, $p(h)$ is uniform and given by $1/s$, with the probability for a given s that we have yet to encounter the hinge given by $(t-s)/t$ and the probability that we are past the hinge given by s/t. $P_{Eh}(t)$ is given by

$$\begin{aligned}
P_{Eh}(t) &= \int_0^t ds \int_0^s dh\, p(s\!:\!h)\, p(h) \qquad (12)\\
&= \int_0^t ds \int_0^s dh \left[\frac{\Sigma_0(t-s)}{st} e^{-s\Sigma_0} + \frac{\Sigma_1}{t} e^{-h\Sigma_0} e^{-(s-h)\Sigma_1}\right]
\end{aligned}$$

$$
\begin{aligned}
&= \int_0^t ds \left[\frac{\Sigma_0(t-s)}{t} e^{-s\Sigma_0} + \frac{\Sigma_1 e^{-s\Sigma_1}\left(1 - e^{-s(\Sigma_0-\Sigma_1)}\right)}{t(\Sigma_0-\Sigma_1)} \right] \\
&= 1 - \frac{e^{-t\Sigma_1}\left(1 - e^{-t(\Sigma_0-\Sigma_1)}\right)}{t(\Sigma_0-\Sigma_1)}
\end{aligned}
$$

Note that the distribution of collision distances, $p(s)$, for the random energy hinge can be seen from the integrand in the above expressions to be

$$
p(s) = \frac{\Sigma_0(t-s)}{t} e^{-s\Sigma_0} + \frac{\Sigma_1 e^{-s\Sigma_1}\left(1 - e^{-s(\Sigma_0-\Sigma_1)}\right)}{t(\Sigma_0-\Sigma_1)} \tag{13}
$$

In the exact case for electrons passing through media with varying cross sections, we have, of course,

$$
\lambda(t) = \frac{1}{P(t)} \int_0^t ds\, s\, \Sigma(s) \exp\left\{ - \int_0^s ds' \Sigma(s') \right\} \tag{14}
$$

with the expression for $P(t)$, the probability of any scatter,

$$
P(t) = \int_0^t ds\, \Sigma(s) \exp\left\{ - \int_0^s ds' \Sigma(s') \right\} \tag{15}
$$

Expressed in terms of energy loss steps rather than distance these become

$$
\lambda(t) = \int_{E_0}^{E_1} dE \left(R_C(E_0) - R_C(E)\right) \left|\frac{dE}{dx}\right|^{-1} \Sigma(E) \exp\left\{ - \int_{E_0}^{E} dE' \left|\frac{dE'}{dx}\right|^{-1} \Sigma(E') \right\} \tag{16}
$$

and

$$
P(t) = \int_{E_0}^{E_1} dE \left|\frac{dE}{dx}\right|^{-1} \Sigma(E) \exp\left\{ - \int_{E_0}^{E} dE' \left|\frac{dE'}{dx}\right|^{-1} \Sigma(E') \right\} \tag{17}
$$

Note that in the above, we have described energy hinge steps in both terms of the change in energy loss (from E_0 to E_1) and also in terms of distance traveled t, as convenient. In EGS5 we use a simple prescription for relating the two and for switching back and forth. For a given initial energy E_0 and a pathlength t, E_1 is given as $E_0 - \Delta E(t)$ with $\Delta E(t)$ computed as follows. A table of electron CSDA ranges $R_C(E)$ is constructed as a function of energy as

$$
R_C(E) = \int_0^E dE' \left|\frac{dE}{dx}\right|^{-1}. \tag{18}
$$

Since the CSDA range is uniquely defined monotonic function of energy, its inverse, the energy of an electron with a given CSDA range, $E_C(R)$, can be trivially determined. Thus we have

$$
\Delta E(t) = E_0 - E_C(R_C(E_0) - t) \tag{19}
$$

By interpolating tabulated values of $R_C(E)$ and $E_C(R)$, relating energy loss to distance traveled is straightforward.

Implementation We begin with the energy loss integration, for which case we are looking for the largest ΔE for which

$$
1 - \frac{1}{t}\frac{\Delta E}{2}\left(\left|\frac{dE}{dx}(E_0)\right|^{-1} + \left|\frac{dE}{dx}(E_1)\right|^{-1} \right) < \epsilon_E \tag{20}
$$

where $t = R_C(E_0) - R_C(E_1)$, the pathlength as determined from the range tables, and represents the analytical value we wish to preserve within a relative error tolerance given by ϵ_E. We use an iterative process, beginning with a value of ΔE that is 50% of E_0 and step down in 5% increments until the inequality is satisfied. We next look at scattering power, starting with the value of ΔE required by the stopping power integration. In this case, we numerically compute the integral of stored values of $G_1(E_0)$ times the stopping power for $K_1(\Delta E)$ and compare that value to that from the energy hinge trapezoidal integration,

$$\frac{\Delta E}{2}\left(\left|\frac{dE}{dx}\right|^{-1}(E_0)G_1(E_0) + \left|\frac{dE}{dx}\right|^{-1}(E_1)G_1(E_1)\right)$$

If the difference is greater than ϵ_E, we reduce ΔE by 5% and continue until the difference is less than ϵ_E.

The treatment for the maximum hinge steps which preserve the mean free path (using Equations 14 and 12) and total scattering probability (using Equations 13 and 15) for hard collisions to within ϵ_E is still being developed.

4 Treatment of Initial Steps of Primary Electrons

It must be noted that not all classes of problems are guaranteed to be modeled accurately whenever the average tracklength or average lateral deflection is modeled correctly in given region volumes. In particular, problems using tallies which have a spatial or directional dependence on secondary particle production occurring prior to the first multiple scattering hinge point (such as deep penetration shower simulations) can exhibit step-size artifacts not present in EGS4, since high energy bremsstrahlung directions can be correlated with electron directions. In such cases, while EGS4 always imposes multiple scattering prior to secondary particle production, the random hinge methodology of EGS5 does not always assure at least some deflection prior to secondary particle generating, sometimes leading to over-estimation of particles in the forward direction.

To counter this problem and still permit EGS5 to take very very long steps as often as possible, for all problems in which secondary particles are being produced and the primary source particles are electrons, a mechanism has been introduced in EGS5 to force very small initial multiple scattering hinge steps. If and only if an electron is determined by EGS subroutine `SHOWER` to be a primary particle on its very first track, its initial multiple scattering step is automatically set to be that used for the smallest characteristic dimension treated in the data set. (This in effect is usually the distance corresponding to the smallest value of K_1 for which the Molière distribution is defined.) Subsequent multiple scattering steps for such particles are then taken to be the minimum of twice the previous step and the default step given the characteristic dimension of the problem. This approach is still approximate, however, and may be replaced by a single scattering model.

5 Conclusions

A new prescription for automatic control of multiple scattering step-sizes by relating them to problem geometry dimensions has been devised. This new technique guarantees that values of the average electron lateral deflections over given steps will be accurate to at least 1% of empirically determined values for the given characteristic dimensions. Additionally, a technique for assuring that the transport distances t between energy loss and multiple scattering hinges as determined from stopping and scattering powers in EGS5 agree to within a given error tolerance (the default is set to 0.1%) with the corresponding distances calculated in PEGS by accurate numerical integration.

References

[1] M. J. Berger. Monte Carlo calculation of the penetration and diffusion of fast charged particles. In B. Adlu, S. Fernbach, and M. Rotenberg, editors, *Methods in Computational Physics Vol. I*, pages 135–215. Academic Press, New York, 1963.

[2] H. A. Bethe. Molière's theory of multiple scattering. *Phys. Rev.*, 89:1256–1266, 1953.

[3] H. Hirayama, Y. Namito, A. F. Bielajew, S. J. Wilderman, and W. R. Nelson. The EGS5 Code System. Report SLAC-R-730, Stanford Linear Accelerator Center, Stanford, CA, 2005.

[4] E. W. Larsen. A theoretical derivation of the condensed history algorithm. *Ann. Nucl. Energy*, 19:701–714, 1992.

[5] J. Sempau, S. J. Wilderman, and A. F. Bielajew. DPM, a fast, accurate Monte Carlo code optimized for photon and electron radiotherapy treatment planning dose calculations. *Phys. Med. Biol.*, 45:2263–2291, 2000.

[6] S. J. Wilderman and A. F. Bielajew. Modified Random Hinge Transport Mechanics and Multiple Scatteringstep-Size Selection in EGS5. In *Proceedings of the 12th EGS Users' Meeting in Japan*, Japan, 2005. (KEK Proceedings 2005-10).

UPGRADE OF CGVIEW
(PARTICLE TRAJECTORY AND GEOMETRY DISPLAY PROGRAM)

A. Takamura[1], T. Sugita[1], Y. Namito[2], H. Hirayama[2]

[1]Science System Laboratory, Ibaraki 309-1716 JAPAN
[2]High Energy Accelerator Research Organization, Ibaraki 305-0801 JAPAN

Abstract

In a calculation using the EGS code, it is important and convenient to check geometry for calculation and particle trajectory visually for validating of the calculation conditions. Also, a graphical interface is useful for understanding the interactions. For these purposes, EGS particle trajectory and geometry 3D-display program CGVIEW has made.

1. Introduction

We have released CGVIEW and accumulated experience. As a result, some requests for improvement are picked up. Also the new CG(Combinatorial Geometry) bodies are added in EGS. So the view function of CGVIEW is extended too. And, we have tried to improve the operation.

2. Outline of new functions

2.1 Add CG bodies

The latest version is available to use next CG bodies in EGS. But, read a manual about old CG bodies (RPP, RCC, TRC, SPH, TOR).

2.1.1 BOX – Arbitrarily oriented orthogonal box

All corners are 90 degree (Fig.1).

[Format] Px Py Pz A1x A1y A1z A2x A2y A2z A3x A3y A3z

Argument	Description
Px Py Pz	= x, y, z coordinates of corner
A1x A1y A1z	= vector of 1st side
A2x A2y A2z	= vector of 2nd side
A3x A3y A3z	= vector of 3rd side

2.1.2 WED – Wedge

A right-angle wedge has a right triangle for a base defined by A1, A2, and a height A3. The vectors A1, A2, and A3 are orthogonal to each other (Fig.2).

[Format] Px Py Pz A1x A1y A1z A2x A2y A2z A3x A3y A3z

Argument	Description
Px Py Pz	= x, y, z coordinates of wedge vertex
A1x A1y A1z	= vector of 1st side of triangular base
A2x A2y A2z	= vector of 2nd side of triangular base
A3x A3y A3z	= height vector

2.1.3 REC – Right Elliptical Cylinder

REC has elliptical for a base defined by A1, A2. The vectors A1, A2, and H are orthogonal to each other (fig.3).

[Format] Px Py Pz Hx Hy Hz A1x A1y A1z A2x A2y A2z

Argument	Description
Px Py Pz	= x, y, z coordinates of ellipse bottom
Hx Hy Hz	= cylinder axis height vector
A1x A1y A1z	= ellipse major axis vector(normal to Hx Hy Hz)
A2x A2y A2z	= ellipse minor axis vector(orthogonal to H and A1)

2.1.4 HAF – Half space with a planer surface

HAF is specified half space with a planer surface (Fig.4).

[Format] Nx Ny Nz L

Argument	Description
Nx Ny Nz	= vector of space direction
L	= length from origin(0,0,0) to a planer surface

2.1.5 TEC – Truncated Elliptical Cone

TEC has elliptical for a base defined by A1, A2. The vectors A1, A2, and H are orthogonal to each other (Fig.5).

[Format] Px Py Pz Hx Hy Hz A1x A1y A1z A2x A2y A2z W

Argument	Description
Px Py Pz	= x, y, z coordinates of ellipse bottom
Hx Hy Hz	= cylinder axis height vector
A1x A1y A1z	= ellipse major axis vector(normal to Hx Hy Hz)
A2x A2y A2z	= ellipse minor axis vector(orthogonal to H and A1)
W	= ratio = top ellipse size/base ellipse size

2.1.6 HEX – Hexagonal Prism

HEX has a hexagon for a base. The vectors A, and H are orthogonal to each other (Fig.6).

[Format] Px Py Pz Hx Hy Hz W Ax Ay Az

Argument	Description
Px Py Pz	= x, y, z coordinates of hexagon bottom
Hx Hy Hz	= cylinder axis height vector
W	= hexagon width
Ax Ay Az	= vector 1st surface direction

2.1.7 ELL – Ellipsoid by relation

ELL is ellipse-sphere (Fig.7).

[Format] P1x P1y P1z P2x P2y P2z R

Argument	Description
P1x P1y P1z	= 1st foci coordinate
P2x P2y P2z	= 2nd foci coordinate
R	= length of major axis

2.1.8 ARB – Arbitrary Polyhedron

There must be eight triplets of entries input for the ARB to describe the (x, y, z) of the corners, although some may not be used (just use zero triplets of entries). These are followed by six more entries, S which follow the prescription: each entry is a four-digit integer that defines a side of the ARB in terms of the corners for the side (Fig.8).

[Format] P1x P1y P1z P2x P2y P2z P3x P3y P3z P4x P4y P4z P5x P5y P5z P6x P6y P6z P7x P7y P7z
P8x P8y P8z S1 S2 S3 S4 S5 S6

Argument	Description
P1…P8	= x, y, z coordinates of eight corners of polyhedron. There must be eight x, y, z triplets to describe the eight corners of the polyhedron.

S1…S6	= four-digit number describing a side of the polyhedron in terms of it's corresponding two corners.(e.g. S1=1278 is a plane / side bounded by corners 1,2,7 & 8)

2.2 File Format change to use input and output.

CGVIEW reads a particle trajectory file (PICT), and makes a geometry file (GEO). These files are changed by follow point. The particle trajectory file only use `.pic` extension name, and fixed format. But, it has no limit of extension name, and it can read free format and CSV format. The geometry file only use `.geo` extension name, and free format. But, it has no limit of extension name, and it can read CSV format.

EGS outputs a particle trajectory file by plotxyz routine. Change NPRECI to 3 for getting a free format output file.

NPRECI	Cylinder Slab	CG	Medium	Format of particle information	Program
0	○	×	×	I5	EGSWIN32
1	○	×	×	I8	EGSWIN32
2	○	○	○	1PE13.6	CGVIEW(Fixed Format)
3	○	○	○	1PE14.6	CGVIEW(Free Format)

2.3 Edit function add in make geometry dialog.

The making geometry function of CGVIEW inputs number on grid. But, there have not delete and insert function, so that operation is no good. So we try to improve operation by edit function which using general software.

[Edit on cell]

It shows a pop-up menu on cell can be used as follow the functions.

[DELETE] [INSERT]

[Edit on row]

The fixed area by the left on row clicked for selecting row area. So, it shows a pop-up menu on row can be used as follow the functions.

[CUT] [COPY] [PASTE] [INSERT PASTE] [ROW DELETE] [ROW INSERT]

2.4 Correspond to four-digit zone number.

The latest version has used the four-digit zone number (Z0000 or Z0018) in EGS. So, CGVIEW has extended to use four-digit zone number. Also, zone number is automatically assigned in Make Geometry Dialog.

2.5 Extended function to particle view.

The usual CGVIEW specified a particle history range for viewing on open view dialog. So, it is defective for particle trajectory in order of history. So, we have extended CGVIEW to show particle trajectory in order of history with showing history change by front or behind button in a legend box (fig.9). But this function is effective of checked [Specify] in environment for display dialog.

If specify history range is 11-11 then next history 10-10 or 12-12.

If specify history range is 11-15 then next history 6-10 or 16-20.

2.6 Extended function to change geometry line.

The usual CGVIEW becomes coarse by view at zoom up geometry. Because CGVIEW had 1 pixel line width at line view. So we added geometry line change function to any line width. It is specified line width in environment for display dialog. A show line width is specified line width pixels. Default is 1.

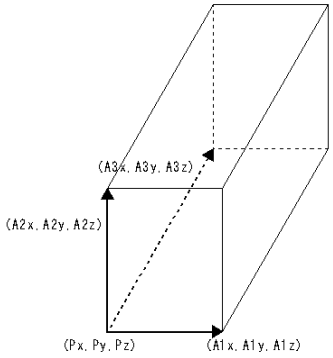

Fig.1 BOX

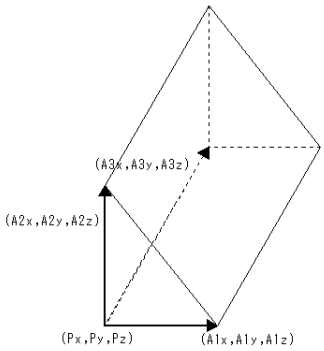

Fig.2 WED

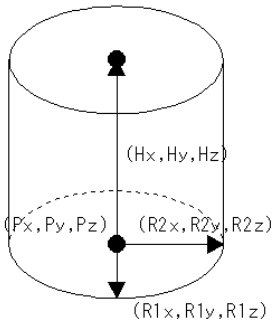

Fig.3 REC

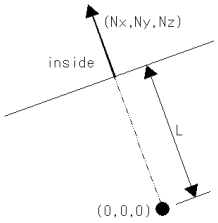

Fig.4 HAF

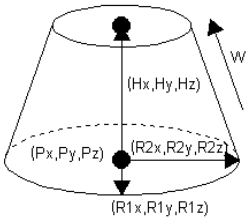

Fig.5 TEC

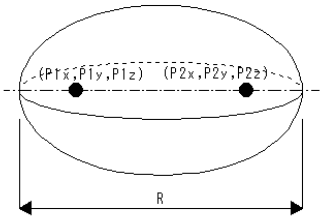

Fig.6 ELL

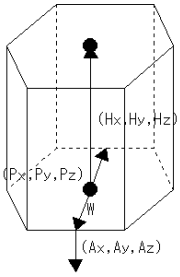

Fig.7 HEX

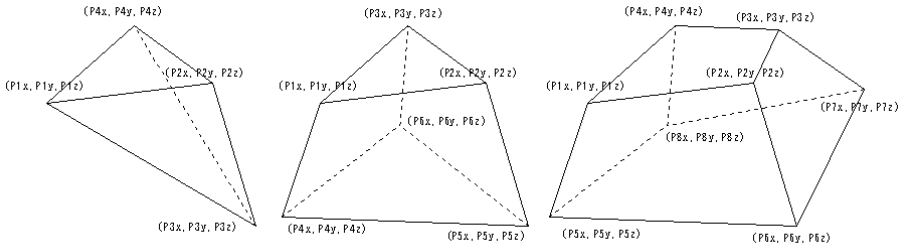

Fig.8 ARB

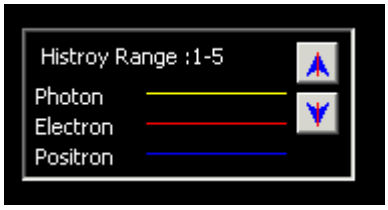

Fig.9 Legend box

MOLIÈRE DISTRIBUTIONS DERIVED FROM NUMERICAL FUNCTIONAL TRANSFORMS AND THE SIMULTANEOUS DISTRIBUTION BETWEEN THE DEFLECTION ANGLE AND THE SPATIAL DISPLACEMENT

T. Nakatsuka, K. Okei†, and N. Takahashi†
Okayama Shoka University, Okayama 700-8601, Japan
†*Dept. of Natural Science, Okayama University, Okayama 700-8530, Japan*

Abstract

Numerical method of functional transforms is examined by comparing its results with those results derived by analytical method. We propose analytical solutions of Molière's series function of higher orders both for the spatial and the projected distributions and confirm the accuracy by comparing them with those derived by numerical transforms. Convergence of the numerical transforms is examined by comparing the results with analytical error predictions by Takahashi and Mori. The simultaneous distribution between the deflection angle and the lateral displacement is derived by applying the numerical functional transforms.

1 Introduction

Molière theory is one of the most accurate theories giving the angular and the lateral distributions of charged particles penetrating through substances [1, 2, 3, 4]. Moliere distribution is expressed by series expansion characterized by the expansion parameter B and the scale angle θ_{M}. Only the first three series functions are indicated by Molière. We propose the analytical solutions for series function of higher orders up to the seventh term both for spatial and the projected distributions. Our results are compared with the same results for spatial distribution derived numerically by Andreo et al. [5] using mathematical library tools, and with the results derived through our numerical functional transforms.

Convergence of our derivation by numerical transforms is examined by Takahashi-Mori error analyses based on complex analyses [6].

Numerical method of functional transforms is applied on deriving the simultaneous distribution between the deflection angle and the lateral displacement solved through Kamata-Nishimura formulation [7, 8] of the Moliere theory.

2 Analytical solutions for Moliere's series function of higher orders

Moliere expressed the spatial angular distribution by series function:

$$f(\vartheta) = f^{(0)}(\vartheta) + B^{-1} f^{(1)}(\vartheta) + B^{-2} f^{(2)}(\vartheta) + \ldots, \tag{1}$$

where B denotes the expansion parameter and ϑ is the deflection angle measured in Molière's scale angle θ_{M}, and the series function $f^{(n)}(\vartheta)$ is determined as

$$f^{(n)}(\vartheta) = \frac{1}{n!} \int_0^\infty y dy J_0(\vartheta y) e^{-\frac{y^2}{4}} \left(\frac{y^2}{4} \ln \frac{y^2}{4} \right)^n. \tag{2}$$

Likewise, he expressed the projected angular distribution by series function:

$$f_{\rm P}(\varphi) = f_{\rm P}^{(0)}(\varphi) + B^{-1} f_{\rm P}^{(1)}(\varphi) + B^{-2} f_{\rm P}^{(2)}(\varphi) + \ldots, \tag{3}$$

where the series function $f_{\rm P}^{(n)}(\varphi)$ is determined as

$$f_{\rm P}^{(n)}(\varphi) = \frac{2}{\sqrt{\pi} n!} \int_0^\infty dy \cos(\varphi y) e^{-\frac{y^2}{4}} \left(\frac{y^2}{4} \ln \frac{y^2}{4} \right)^n. \tag{4}$$

Molière described the series functions $f^{(n)}(\vartheta)$ and $f_{\rm P}(\varphi)$ for general n in complex integral as

$$f^{(n)}(\vartheta) = \frac{1}{n!} \int_0^\infty d\xi e^{-\xi} \xi^n \frac{1}{i\pi} \int_C \frac{d\eta}{\eta^{n+1}(1+\eta)} \left[\ln \frac{\eta}{\xi} - i\pi \right]^n e^{-\frac{\vartheta^2}{1+\eta}}, \tag{5}$$

$$f_{\rm P}^{(n)}(\varphi) = \frac{2}{\sqrt{\pi} n!} \int_0^\infty d\xi e^{-\xi} \xi^n \frac{1}{2\pi i} \int_C \frac{d\eta}{\eta^{n+1}\sqrt{1+\eta}} \left[\ln \frac{\eta}{\xi} - i\pi \right]^n e^{-\frac{\varphi^2}{1+\eta}}, \tag{6}$$

but indicated the explicit expressions only for the first three terms up to $n = 2$.

Modifying the integral variable by $1 - t = 1/(1+\eta)$ as Molière did [2], we have

$$\begin{aligned} f^{(n)}(\vartheta) &= \frac{2}{n!} \int_0^\infty d\xi e^{-\xi} \xi^n \frac{e^{-\vartheta^2}}{2\pi i} \oint \frac{(1-t)^n}{t^{n+1}} \left[\ln \frac{t}{t-1} - \ln \xi \right]^n e^{t\vartheta^2} dt, \\ &= \frac{2}{n!} \int_0^\infty d\xi e^{-\xi} \xi^n \frac{e^{-\vartheta^2}}{2\pi i} \oint \frac{dt}{t^{n+1}} (1-t)^n e^{t\vartheta^2} \sum_{j=0}^n {}_nC_j \left(\ln \frac{t}{t-1} \right)^j (-\ln \xi)^{n-j}, \end{aligned} \tag{7}$$

$$\begin{aligned} f_{\rm P}^{(n)}(\varphi) &= \frac{2}{\sqrt{\pi} n!} \int_0^\infty d\xi e^{-\xi} \xi^n \frac{e^{-\varphi^2}}{2\pi i} \oint \frac{(1-t)^{n-\frac{1}{2}}}{t^{n+1}} \left[\ln \frac{t}{t-1} - \ln \xi \right]^n e^{t\varphi^2} dt, \\ &= \frac{2}{\sqrt{\pi} n!} \int_0^\infty d\xi e^{-\xi} \xi^n \frac{e^{-\varphi^2}}{2\pi i} \oint \frac{dt}{t^{n+1}} (1-t)^{n-\frac{1}{2}} e^{t\varphi^2} \sum_{j=0}^n {}_nC_j \left(\ln \frac{t}{t-1} \right)^j (-\ln \xi)^{n-j}, \end{aligned} \tag{8}$$

where the complex integral with t are performed along a closed path surrounding $t = 0$ and $t = 1$.

Integrals with ξ are evaluated as

$$\int_0^\infty d\xi e^{-\xi} \xi^n (\ln \xi)^{n-j} = \Gamma^{(n-j)}(n+1), \tag{9}$$

and complex integrals for $n \geq 1$ are evaluated as

$$\begin{aligned} T_{\rm n} &\equiv \frac{1}{2\pi i} \oint f(s) \left[\ln \frac{s-\alpha}{s-\beta} \right]^n ds = \frac{1}{2\pi i} \oint ds f(s) \left[\int_\alpha^\beta \frac{du}{s-u} \right]^n \\ &= \int_\alpha^\beta \cdots \int_\alpha^\beta du_1 du_2 \cdots du_n \frac{1}{2\pi i} \oint \frac{f(s)}{(s-u_1)(s-u_2)\cdots(s-u_n)} ds \\ &= \int_\alpha^\beta du_1 \int_\alpha^\beta du_2 \cdots \int_\alpha^\beta du_n \frac{1}{2\pi i} \oint ds f(s) \sum_{k=1}^n \frac{a_k}{s-u_k}, \end{aligned} \tag{10}$$

where

$$a_k = \prod_j^{j \neq k} \frac{1}{u_k - u_j}. \tag{11}$$

Then, for a function $f(s)$ to have poles within a certain area, the Cauchy integral enclosing the area is expressed as [9]

$$\frac{1}{2\pi i} \oint \frac{f(s)}{s-z} ds = f(z) - \sum_{\rm pole} {\rm PP} \equiv f^*(z), \tag{12}$$

where PP denotes the principal part or the terms with negative power for poles in the area. Also we have

$$\int_\alpha^\beta \frac{du_2}{u_1-u_2} = \Big[\ln(u_1-u_2)\Big]_{u_2=\beta}^{u_2=\alpha} = \ln\frac{u_1-\alpha}{\beta-u_1} \pm \pi i, \tag{13}$$

where the sign $\pm$ is determined by the mutual relation between the location u_1 and the path of u_2 from α to β on the complex plane, so

$$\begin{aligned} T_{\rm n} &= \int_\alpha^\beta dt f^*(t)\left\{\left(\ln\frac{t-\alpha}{\beta-t}+\pi i\right)^{n-1} + \left(\ln\frac{t-\alpha}{\beta-t}+\pi i\right)^{n-2}\left(\ln\frac{t-\alpha}{\beta-t}-\pi i\right)+\cdots \right. \\ &\qquad \left. + \left(\ln\frac{t-\alpha}{\beta-t}-\pi i\right)^{n-1}\right\} \\ &= \frac{1}{2\pi i}\int_\alpha^\beta \left\{\left(\ln\frac{t-\alpha}{\beta-t}+\pi i\right)^n - \left(\ln\frac{t-\alpha}{\beta-t}-\pi i\right)^n\right\} f^*(t)dt \\ &= \sum_{k=1}^{[(n+1)/2]} {}_nC_{2k-1}(-\pi^2)^{k-1}\int_\alpha^\beta f^*(t)\left(\ln\frac{t-\alpha}{\beta-t}\right)^{n-2k+1} dt, \end{aligned} \tag{14}$$

where $[x]$ denotes the largest integer not exceeding x.

Thus we have the solution for general terms of Molière series, expressed explicitly by definite integrals in the real space:

$$\begin{aligned} f^{(n)}(\vartheta) &= 2e^{-\vartheta^2}\frac{\Gamma^{(n)}(n+1)}{\Gamma(n+1)}\sum_{j=0}^{n} {}_nC_j(-\vartheta^2)^j/j! \\ &\qquad + 2e^{-\vartheta^2}\int_0^1 \left\{\frac{(1-t)^n}{t^{n+1}}e^{\vartheta^2 t}\right\}^* \sum_{j=0}^{n-1} {}_nM_j\left(\ln\frac{t}{1-t}\right)^{n-1-j} dt, \end{aligned} \tag{15}$$

$$\begin{aligned} f_{\rm P}^{(n)}(\varphi) &= \frac{2}{\sqrt{\pi}}e^{-\varphi^2}\frac{\Gamma^{(n)}(n+1)}{\Gamma(n+1)}\sum_{j=0}^{n} {}_{n-\frac{1}{2}}C_{j-\frac{1}{2}}(-\varphi^2)^j/j! \\ &\qquad + \frac{2}{\sqrt{\pi}}e^{-\varphi^2}\int_0^1 \left\{\frac{(1-t)^{n-\frac{1}{2}}}{t^{n+1}}e^{\varphi^2 t}\right\}^* \sum_{j=0}^{n-1} {}_nM_j\left(\ln\frac{t}{1-t}\right)^{n-1-j} dt, \end{aligned} \tag{16}$$

where

$${}_nM_j \equiv {}_nC_{j+1}(-)^j \sum_{k=0}^{[j/2]} {}_{j+1}C_{2k+1}\frac{\Gamma^{(j-2k)}(n+1)}{\Gamma(n+1)}(-\pi^2)^k. \tag{17}$$

The results for the spatial distribution are listed in Table 1 for n of 0 to 6 and indicated in Fig. 1 for n of 0 to 4. Our results up to $n = 6$ agree well with those derived by Andreo et al. from numerical functional transforms [5]. Also, the results for the projected distribution are listed in Table 2 for n of 0 to 6 and indicated in Fig. 2 for n of 0 to 4.

3 Moliere series functions derived by numerical functional transforms

We evaluate the Hankel transforms (2) and the Fourier transforms (4) by numerical integrals of trapezoidal method;

$$f^{(n)}(\vartheta) \simeq \frac{h^2}{n!}{\sum_{k=0}^{\infty}}' kJ_0(\vartheta hk)e^{-\frac{h^2k^2}{4}}\left(\frac{h^2k^2}{4}\ln\frac{h^2k^2}{4}\right)^n, \tag{18}$$

$$f_{\rm P}^{(n)}(\varphi) \simeq \frac{2h}{\sqrt{\pi}n!}{\sum_{k=0}^{\infty}}' \cos(\varphi hk)e^{-\frac{h^2k^2}{4}}\left(\frac{h^2k^2}{4}\ln\frac{h^2k^2}{4}\right)^n, \tag{19}$$

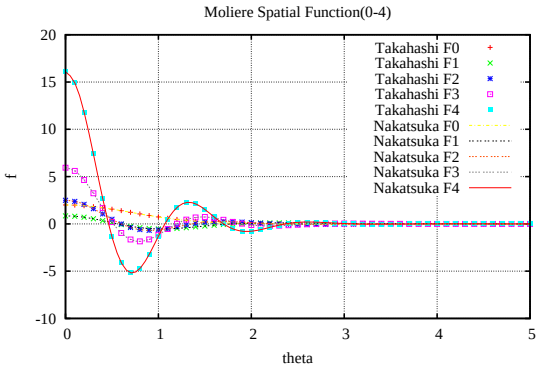

Figure 1: Molière series function $f^{(n)}(\vartheta)$ with n from 0 to 4 for spatial angular distribution, derived from analytical solution (continuous line) and from numerical method (dot symbol).

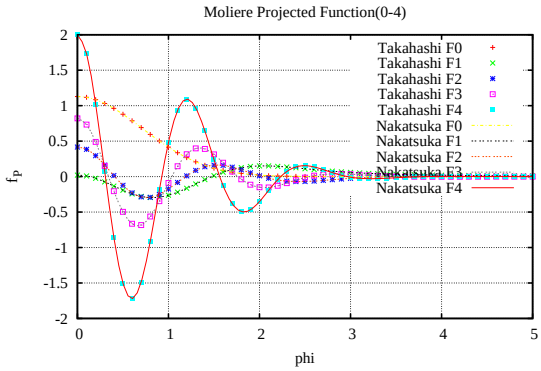

Figure 2: Molière series function $f_{\mathrm{p}}^{(n)}(\varphi)$ with n from 0 to 4 for projected angular distribution, derived from analytical solution (continuous line) and from numerical method (dot symbol).

where $\sum'$ denotes the values are taken half at both sides of sum region.

The results for spatial distribution and projected distribution derived by numerical transforms for n of 0 to 4 are compared with those derived by analytical methods in Fig. 1 and Fig. 2, respectively. They agree very well.

4 Error analyses of numerical transforms by Takahashi and Mori theory

Integration

$$I \equiv \int_a^b f(x)dx \tag{20}$$

can be approximated by summation

$$I_a \equiv \sum A_k f(a_k). \tag{21}$$

Takahashi and Mori evaluated errors of approximation in this case, using complex functional analyses [6]. The integrand can be expressed as

$$f(x) = \frac{1}{2\pi i}\oint \frac{f(z)}{z-x}dz \tag{22}$$

by Cauchy integral. Then the error ΔI of numerical integration can be evaluated as

$$\begin{aligned}
\Delta I &\equiv I - I_a = \frac{1}{2\pi i}\left(\int_a^b dx \oint \frac{f(z)}{z-x}dz - \sum \frac{A_k}{z-a_k}f(z)\right) \\
&= \frac{1}{2\pi i}\oint \left(\ln\frac{z-a}{z-b} - \sum \frac{A_k}{z-a_k}\right) f(z)dz \\
&\equiv \frac{1}{2\pi i}\oint \Phi(z)f(z)dz,
\end{aligned} \tag{23}$$

where $\Phi(z)$ called as the characteristic function is determined by the method of approximation and not depends on the integrand function.

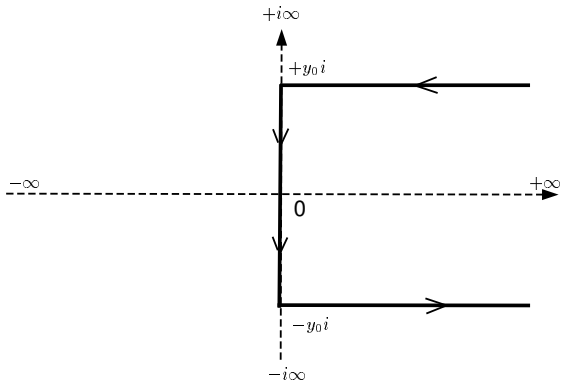

Figure 3: The path of complex integral.

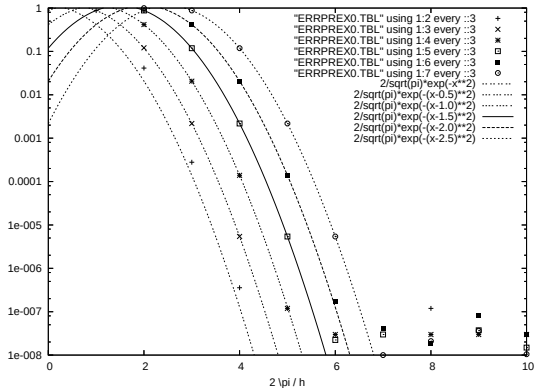

Figure 4: $\Delta I_{\rm P}^{(0)}(\varphi)$

When we approximate a semi-infinite integral by the trapezoidal method

$$I = \int_0^\infty g(x)dx \simeq h \sum_{k=0}^{\infty}{}' g(hk), \tag{24}$$

the error is evaluated as

$$\Delta I = \frac{1}{2\pi i} \oint \Phi(z) g(z) dz, \tag{25}$$

where

$$\Phi(z) = -\frac{\pi}{2} \left\{ i \ \mathrm{Sign}(\mathrm{Im}\ z) + \cot \frac{\pi z}{h} \right\}. \tag{26}$$

The path of complex integral is taken as indicated in Fig. 3, where $\pm y_0 i \simeq \pm(4\pi/h)i$ almost agree with the saddle point [8] of the integrand $\Phi(z)g(z)$.

According to the Takahashi-Mori theory, we can predict the errors of numerical transforms of the n-th expansion function, $\Delta I_{\rm P}^{(n)}(\varphi)$ for projected distribution and $\Delta I^{(n)}(\vartheta)$ for spatial distribution:

$$\Delta I_{\rm P}^{(0)}(\varphi) = \frac{1}{2\pi i} \oint \frac{2\Phi(z)}{\pi} \cos(\phi z) e^{-\frac{z^2}{4}} dz \simeq -\frac{2}{\sqrt{\pi}} e^{-\frac{y_0^2}{4}}, \tag{27}$$

$$\begin{aligned} \Delta I_{\rm P}^{(n)}(\varphi) &= \frac{1}{2\pi i} \int_{y_0 i}^{-y_0 i} \frac{2\Phi(z)}{\pi n!} \cosh(\varphi y) e^{-\frac{z^2}{4}} \left(\frac{z^2}{4} \ln \frac{z^2}{4} \right)^n dz \\ &\simeq -2n(2n-1)!! \zeta(2n+1) \left(\ln \frac{2\pi}{h} \right)^{n-1} \left(\frac{2\pi}{h} \right)^{-2n-1}, \end{aligned} \tag{28}$$

$$\begin{aligned} \Delta I^{(n)}(\vartheta) &= \frac{1}{2\pi i} \int_{y_0 i}^{-y_0 i} \frac{\Phi(z)}{n!} z J_0(\vartheta z) e^{-\frac{z^2}{4}} \left(\frac{z^2}{4} \ln \frac{z^2}{4} \right)^n dz \\ &\simeq \frac{1}{n!} |B_{2n+2}| \left(\ln \frac{2\pi}{h} \right)^n \left(\frac{2}{h} \right)^{-2n-2}, \end{aligned} \tag{29}$$

where $\zeta(n)$ denotes ζ-function and B_n denote Bernoulli numbers [10].

We want to confirm the convergence of our results of numerical transforms by comparing the feature of our convergence with the prediction from Takahashi-Mori theory. The both agree well as indicated in Figs. 4, 5, 6, and 7.

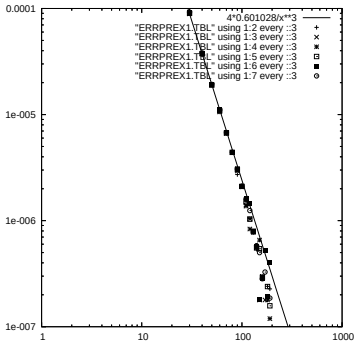

Figure 5: $\Delta I_{\rm P}^{(1)}$

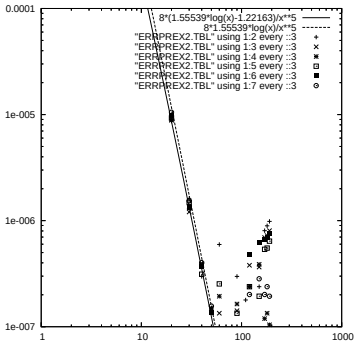

Figure 6: $\Delta I_{\rm P}^{(2)}$

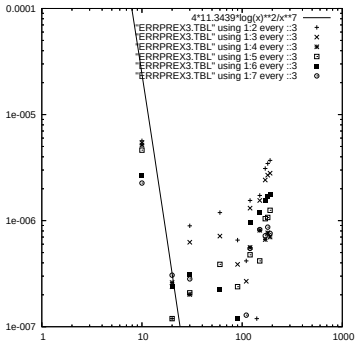

Figure 7: $\Delta I_{\rm P}^{(3)}$

5 Simultaneous distribution between the deflection angle and the lateral displacement

We derive the simultaneous distribution between the deflection angle and the lateral displacement in y-θ_y plane by numerical Fourier transforms. According to the Kamata-Nishimura formulation of the Moliere theory, the diffusion equation can be described as

$$\frac{\partial}{\partial t}\tilde{f}(\zeta,\eta) = \eta\frac{\partial}{\partial \eta}\tilde{f} - \frac{K^2\zeta^2}{4E^2}\tilde{f}\left\{1 - \frac{1}{\Omega}\ln\frac{K^2\zeta^2}{4E^2}\right\}, \tag{30}$$

where ζ and η denote Fourier variables corresponding to θ and y, respectively. This equation gives the solution

$$\begin{aligned}
\ln 2\pi\tilde{f} &= -\frac{K^2t}{4E^2}\frac{1}{3\eta t}\left\{(\zeta+\eta t)^3 - \zeta^3\right\} - \frac{1}{\Omega}(\frac{2}{3} - \ln\frac{K^2}{4E^2})\frac{K^2t}{4E^2}\frac{1}{3\eta t}\left\{(\zeta+\eta t)^3 - \zeta^3\right\} \\
&\qquad + \frac{1}{\Omega}\frac{K^2t}{4E^2}\frac{1}{3\eta t}\left\{(\zeta+\eta t)^3\ln(\zeta+\eta t)^2 - \zeta^3\ln\zeta^2\right\} \\
&= \frac{1}{\Omega}\frac{K^2t}{4E^2}\frac{1}{3\eta t}\left\{(\zeta+\eta t)^3\ln\frac{K^2(\zeta+\eta t)^2}{4E^2e^{2/3+\Omega}} - \zeta^3\ln\frac{K^2\zeta^2}{4E^2e^{2/3+\Omega}}\right\},
\end{aligned} \tag{31}$$

equivalent with Moliere's 1955 result, his Eq. (3.3') [11]. The simultaneous distribution can be obtained by applying Fourier double transforms as

$$f(\theta,y)d\theta dy = \frac{d\theta dy}{2\pi}\iint e^{-\theta\zeta - y\eta}\tilde{f}(\zeta,\eta)d\zeta d\eta. \tag{32}$$

The results derived through FFT integration is indicated in Fig. 8.

The exact result is derived as θ_y distribution with $y = 0$ from

$$f(\theta_y,0)d\theta dy = \frac{d\theta dy}{\pi}\int_0^\infty d\zeta\cos(\theta_y\zeta)\int_{-\infty}^\infty \tilde{f}(\zeta,\eta)d\eta, \tag{33}$$

as indicated in Fig. 9. At the large angle region, the distribution is well explained by a model of screened single scattering,

$$\frac{N}{A}\sigma_{\rm P}(\theta_y)d\theta_y dx = \frac{1}{2\Omega}\frac{K^2}{E^2}\frac{1}{\theta_y^3}d\theta_y dt \qquad (\theta_y \geq \theta_0,\ \text{where}\ \theta_0 \simeq \sqrt{e}\chi_a), \tag{34}$$

or another screening model of

$$\frac{N}{A}\sigma_{\rm P}(\theta_y)d\theta_y dx = \frac{1}{2\Omega}\frac{K^2}{E^2}\frac{1}{(\theta_y^2+\chi_a^2)^{3/2}}d\theta_y dt, \tag{35}$$

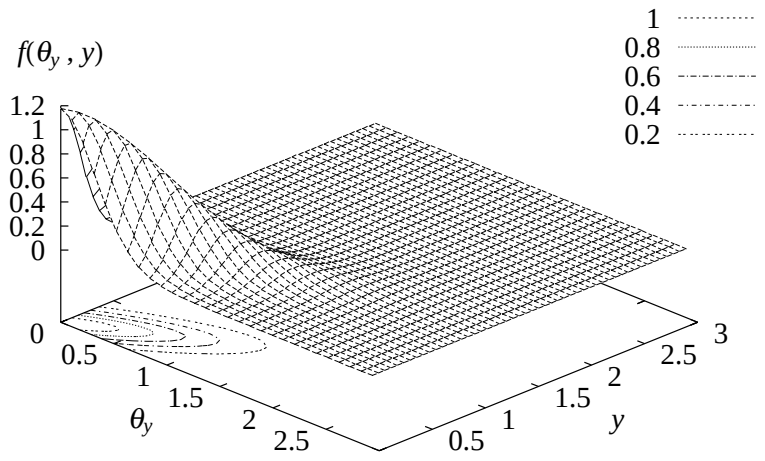

Figure 8: The simultaneous distribution between the deflection angle and the lateral displacement, derived through FFT integrations. $K^2/E^2 = t = 1$ and $\Omega = 15$.

following after the Fermi distribution of multiple scattering [12],

$$f(\theta, y)d\theta dy = \frac{2\sqrt{3}E^2}{\pi K^2 t^2} \exp\left[-\frac{4E^2}{K^2}\left(\frac{\theta^2}{t} - \frac{3y\theta}{t^2} + \frac{3y^2}{t^3}\right)\right] d\theta dy, \tag{36}$$

as

$$\begin{aligned} & f(\theta_y, 0)d\theta dy \\ \simeq\ & \frac{d\theta_y dy}{2\Omega}\frac{K^2}{E^2}\int_0^t dt' \int_{-\infty}^{\infty} \frac{2\sqrt{3}E^2}{\pi K^2 t'^2} \exp\left\{-\frac{4E^2}{K^2 t'}\left(\theta'^2 - \frac{3(t-t')\theta_y\theta'}{t'} + \frac{3(t-t')^2\theta_y^2}{t'^2}\right)\right\}(\theta_y - \theta')^{-3} d\theta' \\ =\ & \frac{\sqrt{3}d\theta_y dy}{\pi\Omega}\int_0^t \frac{dt'}{t'^2}\int_{-\infty}^{\infty} \frac{1}{|\theta_y - \theta'|^3} \exp\left\{-\frac{4E^2}{K^2 t'}\left(\theta'^2 - \frac{3(t-t')\theta_y\theta'}{t'} + \frac{3(t-t')^2\theta_y^2}{t'^2}\right)\right\} d\theta'. \end{aligned} \tag{37}$$

In the central region it agrees with the Fermi distribution (36),

$$f(\theta_y, 0)d\theta dy \simeq \frac{\sqrt{3}}{2\pi} e^{-\theta_y^2} d\theta dy. \tag{38}$$

Simultaneous probability density for arbitrary combination between θ_y and y can be obtained from the same calculus with ζ-η coordinetes rotated by an adequate angle. Especially by an angle of $\pi/2$, we get y distribution with $\theta_y = 0$:

$$f(0, y)d\theta dy = \frac{d\theta dy}{\pi}\int_0^{\infty} d\eta \cos(y\eta) \int_{-\infty}^{\infty} \tilde{f}(\zeta, \eta) d\zeta. \tag{39}$$

The result is indicated in Fig. 10. At the large displacement region, the distribution is well explained by the successive twice single-scatterings with the same value of opposite sign:

$$f(0, y)d\theta dy \simeq d\theta dy \int_0^{\infty} t' \left\{\frac{1}{2\Omega}\frac{K^2}{E^2}\frac{(t-t')^3}{y^3}\right\}^2 \frac{1}{t-t'} dt' = \frac{t^7}{42}\left(\frac{1}{2\Omega}\frac{K^2}{E^2}\frac{1}{y^3}\right)^2. \tag{40}$$

In the central region it agrees with the Fermi distribution (36),

$$f(0, y)d\theta dy \simeq \frac{\sqrt{3}}{2\pi} e^{-3y^2} d\theta dy. \tag{41}$$

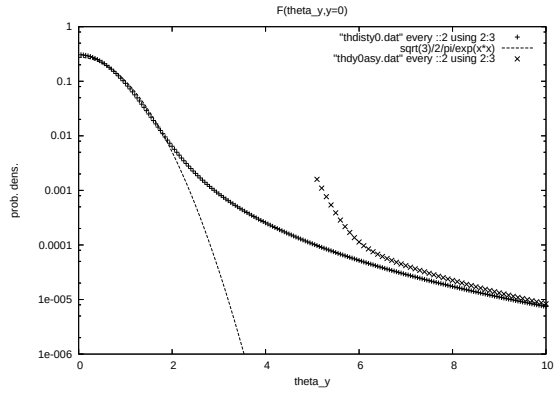

Figure 9: θ_y distribution with $y = 0$. $K^2/(4E^2) = t = 1$ and $\Omega = 10$.

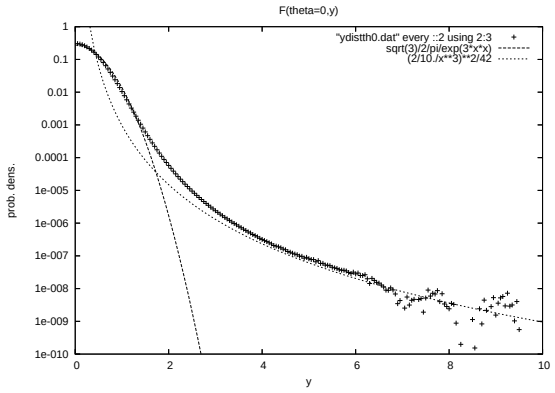

Figure 10: y distribution with $\theta_y = 0$. $K^2/(4E^2) = t = 1$ and $\Omega = 10$.

6 Conclusions

Analytical solutions for Moliere's series function of higher orders are proposed. The results agree well with Andreo et al.'s numerical result for the spatial distribution and our numerical result for the projected distribution. Convergence of numerical transforms is confirmed by comparing our results with Takahashi and Mori's theoretical prediction for the converging errors. Numerical method of functional transforms is applied to derive simultaneous distribution between the deflection angle and the lateral displacement under the Moliere process. The asymptotic property of distribution at the large variable region is well explained by taking account the screened single scattering and the result at the central variable region agrees well with the Fermi distribution predicted under the gaussian approximation.

References

[1] G. Molière, Z. Naturforsch. **2a**, 133(1947).

[2] G. Molière, Z. Naturforsch. **3a**, 78(1948).

[3] H.A. Bethe, Phys. Rev. **89**, 1256(1953).

[4] W.T. Scott, Rev. Mod. Phys. **35**, 231(1963).

[5] P. Andreo, J. Medin, and A.F. Bielajew, Med. Phys. **20**, 1315(1993).

[6] H. Takahashi and M. Mori, Report of the Computer Center, University of Tokyo, **3**, 41(1970).

[7] K. Kamata and J. Nishimura, Prog. Theor. Phys. Suppl. **6**, 93(1958).

[8] J. Nishimura, in *Handbuch der Physik, Band 46*, edited by S. Flügge (Springer, Berlin, 1967), Teil **2**, p. 1.

[9] T. Nakatsuka, Phys. Rev. **D35**, 210(1987).

[10] *Handbook of Mathematical Functions with Formulas, Graphs, and Mathematical Tables*, edited by M. Abramowitz and I. A. Stegun (Dover, New York, 1965).

[11] G. Molière, Z. Naturforsch. **10a**, 177(1955).

[12] B. Rossi and K. Greisen, Rev. Mod. Phys. **27**, 240(1941).

Table 1: Molière series function for spatial distribution, $f^{(n)}(\vartheta)$.

ϑ	$n=0$	$n=1$	$n=2$	$n=3$	$n=4$	$n=5$	$n=6$
0.0	2.000000	0.845568	2.492920	5.942900	16.064640	46.76560	144.24120
0.1	1.980100	0.808982	2.382209	5.596667	14.922664	42.84408	130.31842
0.2	1.921579	0.703825	2.069377	4.635929	11.810137	32.34528	93.69899
0.3	1.827862	0.542471	1.601407	3.238605	7.407681	17.90483	44.74223
0.4	1.704288	0.343678	1.048789	1.666699	2.695466	3.23009	-2.38178
0.5	1.557602	0.129532	0.489563	0.192650	-1.371420	-8.31053	-35.69315
0.6	1.395353	-0.077667	-0.004416	-0.957694	-4.092345	-14.58373	-48.92124
0.7	1.225253	-0.258374	-0.379370	-1.648647	-5.170559	-15.17296	-42.86177
0.8	1.054585	-0.398090	-0.606831	-1.852528	-4.734953	-11.25875	-24.07355
0.9	0.889716	-0.488658	-0.685178	-1.640092	-3.242532	-5.01627	-1.73378
1.0	0.735759	-0.528482	-0.635874	-1.149528	-1.306124	1.20250	15.91188
1.1	0.596395	-0.521762	-0.495913	-0.544868	0.491066	5.59840	24.12222
1.2	0.473855	-0.477025	-0.308644	0.024077	1.738152	7.33947	22.48126
1.3	0.369039	-0.405297	-0.115105	0.450691	2.263378	6.58437	14.01306
1.4	0.281717	-0.318272	0.052454	0.684478	2.121297	4.19348	3.28229
1.5	0.210798	-0.226753	0.174023	0.728221	1.521558	1.28595	-5.58626
1.6	0.154609	-0.139564	0.242221	0.623667	0.733315	-1.16950	-10.21908
1.7	0.111152	-0.062974	0.260288	0.431999	-0.001453	-2.60786	-10.33058
1.8	0.078328	-0.000610	0.238649	0.215136	-0.523384	-2.92450	-7.22223
1.9	0.054104	0.046264	0.191128	0.022140	-0.773010	-2.37078	-2.86618
2.0	0.036631	0.078229	0.131619	-0.117490	-0.775881	-1.37040	0.97138
2.1	0.024310	0.097115	0.071744	-0.194070	-0.609511	-0.33896	3.26117
2.2	0.015814	0.105414	0.019637	-0.213476	-0.366956	0.43588	3.81399
2.3	0.010084	0.105799	-0.020266	-0.190820	-0.128259	0.83562	3.05977
2.4	0.006302	0.100782	-0.046722	-0.144212	0.055008	0.88674	1.69029
2.5	0.003861	0.092498	-0.060794	-0.090028	0.162421	0.70156	0.33978
2.6	0.002318	0.082618	-0.064886	-0.040236	0.198394	0.41492	-0.59906
2.7	0.001365	0.072347	-0.061896	-0.001633	0.181883	0.13785	-1.00944
2.8	0.000787	0.062474	-0.054602	0.023537	0.136336	-0.06414	-0.98039
2.9	0.000445	0.053456	-0.045306	0.036268	0.082423	-0.17110	-0.69702
3.0	0.000247	0.045505	-0.035685	0.039326	0.034365	-0.19566	-0.34391
3.1	0.000134	0.038666	-0.026807	0.036016	-0.000682	-0.16612	-0.04872
3.2	0.000071	0.032882	-0.019228	0.029362	-0.021288	-0.11237	0.13227
3.3	0.000037	0.028044	-0.013134	0.021676	-0.029614	-0.05736	0.20001
3.4	0.000019	0.024020	-0.008470	0.014455	-0.029384	-0.01421	0.18697
3.5	0.000010	0.020681	-0.005051	0.008482	-0.024382	0.01269	0.13334
3.6	0.000005	0.017906	-0.002643	0.004008	-0.017624	0.02481	0.07187
3.7	0.000002	0.015593	-0.001012	0.000951	-0.011085	0.02637	0.02199
3.8	0.000001	0.013655	0.000052	-0.000936	-0.005782	0.02202	-0.00927
3.9	0.000000	0.012023	0.000699	-0.001950	-0.002021	0.01548	-0.02321
4.0	0.000000	0.010638	0.001074	-0.002367	0.000313	0.00917	-0.02499
4.1	0.000000	0.009456	0.001266	-0.002411	0.001532	0.00424	-0.02028
4.2	0.000000	0.008441	0.001339	-0.002248	0.001986	0.00096	-0.01348
4.3	0.000000	0.007565	0.001339	-0.001988	0.001980	-0.00085	-0.00726
4.4	0.000000	0.006804	0.001296	-0.001700	0.001740	-0.00162	-0.00272
4.5	0.000000	0.006140	0.001229	-0.001422	0.001413	-0.00174	0.00001
4.6	0.000000	0.005557	0.001151	-0.001173	0.001087	-0.00152	0.00129
4.7	0.000000	0.005044	0.001068	-0.000960	0.000802	-0.00118	0.00164
4.8	0.000000	0.004591	0.000986	-0.000782	0.000572	-0.00084	0.00148
4.9	0.000000	0.004189	0.000907	-0.000635	0.000397	-0.00055	0.00114
5.0	0.000000	0.003831	0.000833	-0.000516	0.000268	-0.00034	0.00077

Table 2: Molière series function for projected distribution, $f_{\mathrm{p}}^{(n)}(\varphi)$.

φ	$n=0$	$n=1$	$n=2$	$n=3$	$n=4$	$n=5$	$n=6$
0.00	1.128379	0.020587	0.416704	0.820752	1.997350	5.320833	15.22461
0.10	1.117152	0.008840	0.384501	0.732435	1.734165	4.490547	12.48501
0.20	1.084135	-0.024586	0.294098	0.489115	1.022164	2.285668	5.33868
0.30	1.031261	-0.074567	0.162722	0.149698	0.068714	-0.546837	-3.45096
0.40	0.961541	-0.133533	0.014793	-0.205723	-0.855940	-3.070553	-10.58471
0.50	0.878783	-0.192738	-0.123357	-0.497175	-1.503418	-4.504399	-13.56488
0.60	0.787243	-0.243656	-0.228920	-0.664980	-1.720654	-4.477483	-11.63224
0.70	0.691275	-0.279262	-0.286923	-0.683165	-1.488306	-3.131038	-5.92863
0.80	0.594986	-0.294970	-0.292506	-0.562865	-0.914224	-1.020702	1.12260
0.90	0.501969	-0.289100	-0.250831	-0.345673	-0.188301	1.115862	6.88629
1.00	0.415107	-0.262828	-0.174896	-0.089895	0.482526	2.629149	9.54287
1.10	0.336480	-0.219708	-0.082008	0.145694	0.935868	3.160676	8.65805
1.20	0.267344	-0.164888	0.010132	0.315855	1.093094	2.715990	5.12882
1.30	0.208208	-0.104204	0.086801	0.397260	0.967366	1.600955	0.62561
1.40	0.158942	-0.043318	0.138460	0.389978	0.643330	0.268450	-3.16051
1.50	0.118930	0.012959	0.161524	0.312963	0.239924	-0.854879	-5.13313
1.60	0.087229	0.061104	0.157817	0.195882	-0.129028	-1.497137	-5.05543
1.70	0.062711	0.099042	0.133105	0.070142	-0.384181	-1.591335	-3.43880
1.80	0.044192	0.126079	0.095212	-0.038424	-0.493521	-1.246754	-1.18338
1.90	0.030525	0.142667	0.052201	-0.113808	-0.468959	-0.671405	0.83225
2.00	0.020667	0.150071	0.010962	-0.150723	-0.351744	-0.083259	2.04630
2.10	0.013716	0.150030	-0.023610	-0.152830	-0.193886	0.357420	2.31564
2.20	0.008922	0.144440	-0.048862	-0.129455	-0.041977	0.578448	1.84120
2.30	0.005689	0.135118	-0.064163	-0.092014	0.072776	0.590071	0.99674
2.40	0.003556	0.123644	-0.070406	-0.051074	0.137432	0.456120	0.15167
2.50	0.002178	0.111280	-0.069409	-0.014523	0.154558	0.258465	-0.44708
2.60	0.001308	0.098951	-0.063351	0.013096	0.136453	0.068014	-0.71233
2.70	0.000770	0.087274	-0.054342	0.030322	0.098904	-0.071052	-0.68808
2.80	0.000444	0.076608	-0.044155	0.037983	0.056287	-0.143751	-0.48812
2.90	0.000251	0.067117	-0.034095	0.038216	0.018802	-0.157494	-0.23487
3.00	0.000139	0.058825	-0.024999	0.033602	-0.008250	-0.131600	-0.01875
3.10	0.000076	0.051672	-0.017300	0.026536	-0.023746	-0.087573	0.11640
3.20	0.000040	0.045547	-0.011125	0.018882	-0.029333	-0.042673	0.16747
3.30	0.000021	0.040323	-0.006401	0.011867	-0.027953	-0.007265	0.15605
3.40	0.000011	0.035869	-0.002941	0.006136	-0.022683	0.014877	0.11171
3.50	0.000005	0.032064	-0.000513	0.001885	-0.016042	0.024670	0.06006
3.60	0.000003	0.028801	0.001111	-0.000975	-0.009726	0.025438	0.01727
3.70	0.000001	0.025990	0.002140	-0.002685	-0.004627	0.021033	-0.01014
3.80	0.000001	0.023554	0.002741	-0.003530	-0.001026	0.014689	-0.02263
3.90	0.000000	0.021431	0.003047	-0.003784	0.001184	0.008558	-0.02424
4.00	0.000000	0.019571	0.003156	-0.003669	0.002296	0.003732	-0.01979
4.10	0.000000	0.017932	0.003140	-0.003351	0.002647	0.000509	-0.01326
4.20	0.000000	0.016480	0.003046	-0.002946	0.002538	-0.001284	-0.00714
4.30	0.000000	0.015189	0.002907	-0.002524	0.002195	-0.002017	-0.00259
4.40	0.000000	0.014035	0.002746	-0.002126	0.001773	-0.002083	0.00020
4.50	0.000000	0.013000	0.002576	-0.001771	0.001360	-0.001803	0.00154
4.60	0.000000	0.012068	0.002405	-0.001465	0.001001	-0.001397	0.00190
4.70	0.000000	0.011226	0.002239	-0.001207	0.000711	-0.000993	0.00172
4.80	0.000000	0.010464	0.002081	-0.000994	0.000489	-0.000654	0.00133
4.90	0.000000	0.009771	0.001931	-0.000818	0.000324	-0.000398	0.00091
5.00	0.000000	0.009139	0.001792	-0.000673	0.000207	-0.000218	0.00055

Comparison of multiple Coulomb scattering distributions: numerical calculation, Molière theory and Monte Carlo sampling

K. Okei[†], N. Takahashi[†] and T. Nakatsuka[‡]
[†]*Okayama University, Okayama 700-8530, Japan*
[‡]*Okayama Shoka University, Okayama 700-8601, Japan*

Abstract

The exact multiple Coulomb scattering distribution under the small angle approximation was calculated by numerical integration. Molière's theory and our Monte Carlo sampling method were compared for the small step size cases. It was found that the accuracy of our Monte Carlo method is better than that of Molière's theory in the cases where the expected total number of scattering, $\mu \leq 100$.

1 Introduction

To simulate the transport of high energy charged particles in matter, Monte Carlo codes such as EGS4 or GEANT3 [1, 2] use Molière's theory [3, 4, 5] to simulate the multiple Coulomb scattering. However, the Molière distribution is inaccurate for the case of vary small or large step sizes where the scattering cannot be regarded as "multiple", the small angle approximation is not valid or energy loss during the step is not negligible.

We have mainly been reported on subjects which are important for the large step size case, such as the Molière distribution with ionization or Monte Carlo sampling method [6, 7, 8, 9, 10]. In this work, we calculate the exact multiple Coulomb scattering distribution and examine the Molière distribution and our Monte Carlo method for the small step size cases.

2 Molière's theory

In this section, we briefly review Molière's theory according to Bethe's paper[5]. Under the small angle approximation, the probability density function $f(\theta, t)$ of scattering into an angle θ after traversing a thickness t is

$$f(\theta,t) = \int_0^\infty \eta d\eta J_0(\eta\theta) \exp\left[-Nt\int_0^\infty \sigma(\chi)\chi d\chi \left\{1 - J_0(\eta\chi)\right\}\right], \tag{1}$$

where notation is the same as ref. [5].

Assuming $\chi_0 \ll \chi_c$ and introducing the characteristic screening angle χ_a, Bethe approximated and transformed the above equation into

$$f(\theta)\theta d\theta = \vartheta d\vartheta \int_0^\infty u du J_0(\vartheta u) \exp\left[-\frac{1}{4}u^2\left\{1 - \frac{1}{B}\ln\left(\frac{1}{4}u^2\right)\right\}\right]. \tag{2}$$

This function is expanded in a power series in $1/B$

$$f(\theta)\theta d\theta = \vartheta d\vartheta[f^{(0)}(\vartheta) + B^{-1}f^{(1)}(\vartheta) + B^{-2}f^{(2)}(\vartheta) + \cdots] \tag{3}$$

where

$$f^{(n)}(\vartheta) = \frac{1}{n!}\int_0^\infty u du J_0(\vartheta u) \exp\left(-\frac{1}{4}u^2\right)\left[\frac{1}{4}u^2\ln\left(\frac{1}{4}u^2\right)\right]^n. \tag{4}$$

For the projected distributions, equations corresponding to eq. (1), (3) and (4) are

$$f_{\rm p}(\phi,t) = \frac{2}{\pi}\int_0^\infty d\eta\cos(\eta\phi)\exp\left[-2Nt\int_0^\infty \sigma_{\rm p}(\chi)d\chi\{1-\cos(\eta\chi)\}\right] \quad (5)$$

$$f_{\rm p}(\phi)\phi d\phi = \varphi d\varphi[f_{\rm p}^{(0)}(\varphi)+B^{-1}f_{\rm p}^{(1)}(\varphi)+B^{-2}f_{\rm p}^{(2)}(\varphi)+\cdots] \quad (6)$$

$$f_{\rm p}^{(n)}(\varphi) = \frac{2}{\pi n!}\int_0^\infty du\cos(\varphi u)\exp\left(-\frac{1}{4}u^2\right)\left[\frac{1}{4}u^2\ln\left(\frac{1}{4}u^2\right)\right]^n \quad (7)$$

respectively.

3 The exact distribution

To calculate the exact multiple Coulomb scattering distribution, we use the screened Rutherford cross section with the small angle approximation

$$Nt\sigma(\chi)\chi d\chi = 2\chi_c^2\frac{\chi d\chi}{(\chi^2+\chi_a^2)^2}, \quad (8)$$

or

$$Nt\sigma_{\rm p}(\chi)d\chi = \frac{\chi_c^2 d\chi}{2(\chi^2+\chi_a^2)^{\frac{3}{2}}} \quad (9)$$

and numerically integrate eq. (1) or (5) by using the double exponential (DE) method [11, 12]. To stabilize the integration, the equation is transformed as

$$\begin{aligned} f(\theta,t) &= \int_0^\infty \eta d\eta J_0(\eta\theta)\exp\left[-Nt\int_0^\infty \sigma(\chi)\chi d\chi\,\{1-J_0(\eta\chi)\}\right] \\ &= \int_0^\infty \eta d\eta J_0(\eta\theta)g(\eta,\mu) \\ &= \int_0^\infty \eta d\eta J_0(\eta\theta)\{g(\eta,\mu)-\exp(-\mu)\}+\int_0^\infty \eta d\eta J_0(\eta\theta)\exp(-\mu) \\ &= \int_0^\infty \eta d\eta J_0(\eta\theta)\{\exp[-\mu\{1-\eta K_1(\eta)\}]-\exp(-\mu)\}+\exp(-\mu)\frac{\delta(\theta)}{\theta} \end{aligned} \quad (10)$$

where $\mu=\chi_c^2/\chi_a^2$ is the expected total number of scattering and K_1 is the first order modified Bessel function of the second kind [13, 14, 15, 16].

To test the numerical Fourier (Hankel) transform with the DE method, the following integrals were computed (figure 1)

$$F(\eta)=\int_0^\infty \frac{\chi J_0(\eta\chi)d\chi}{(\chi^2+1)^2}=\frac{\eta}{2}K_1(\eta), \quad F_{\rm p}(\eta)=\int_0^\infty \frac{\cos(\eta\chi)d\chi}{2(\chi^2+1)^{\frac{3}{2}}}=\frac{\eta}{2}K_1(\eta).$$

Figure 1 shows that the numerical solutions, $F(\eta)$ and $F_{\rm p}(\eta)$ coincide with $\frac{\eta}{2}K_1(\eta)$ down to the limit of double precision. Furthermore, the numerical integrations (NI) of eq. (5) were performed for $\mu=0.25$, 1, 5, 25 and 125, and compared with the direct Monte Carlo simulation (MC) of the screened Rutherford scattering. Figure 2 shows the relative difference between MC and NI and no systematic effect can be seen. From these results, we regard that NI with the DE method is reliable.

Figure 3 and 4 show NI of eq. (1) for $\mu=0.01$, 0.1, 1, 2, 5, 100 and 10^5. In figure 4, distributions are multiplied by ϑ^2 and compared with Gaussian (dotted curve). These figures show the transition from single to plural scattering or from plural to multiple scattering.

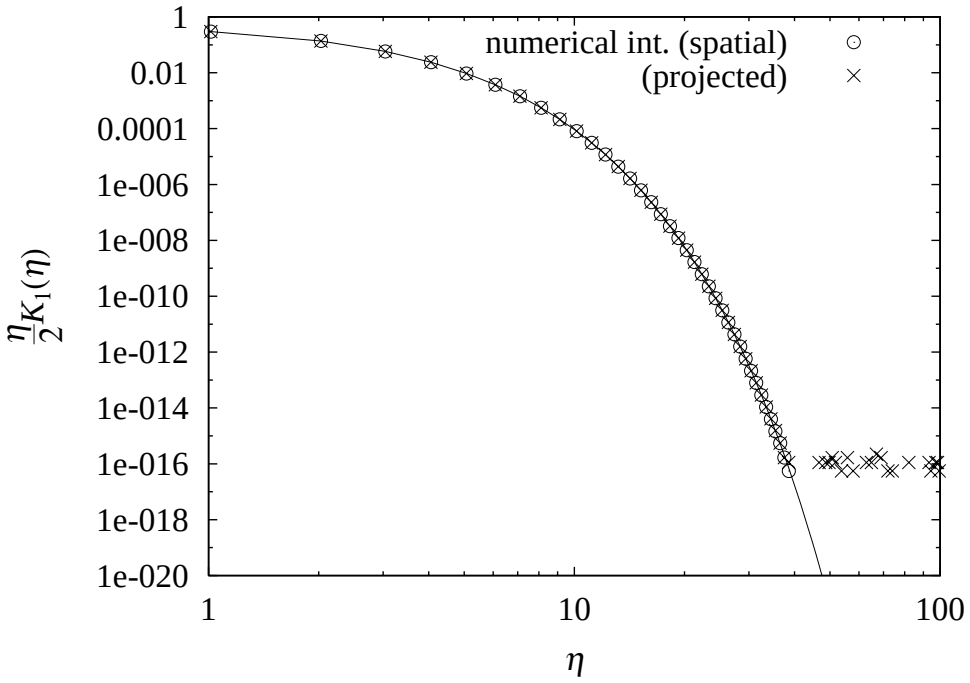

Figure 1: Comparison of $F(\eta)$ (circle), $F_{\rm p}(\eta)$ (cross) and $\frac{\eta}{2}K_1(\eta)$ (solid curve).

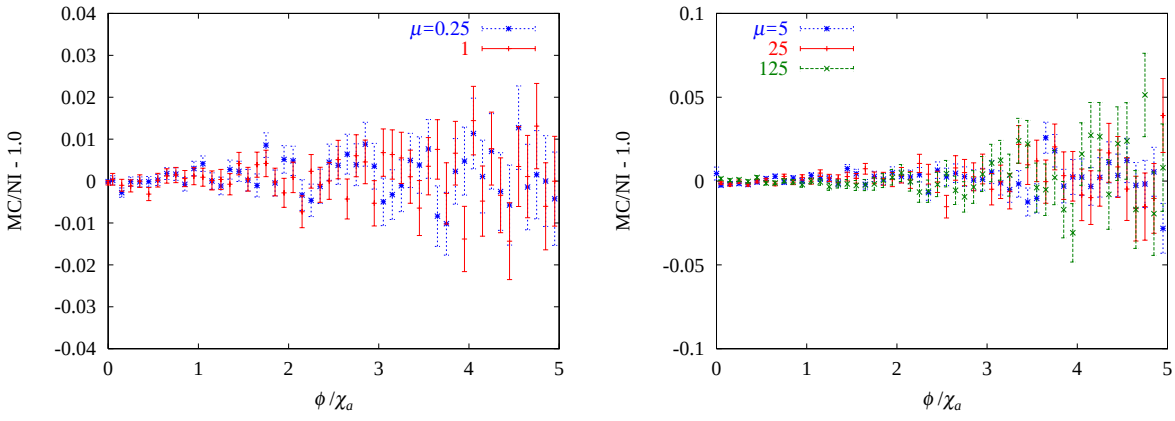

Figure 2: Comparison of the numerical integration of eq. (5) and the direct Monte Carlo simulation for $\mu = 0.25$, 1, 5, 25 and 125.

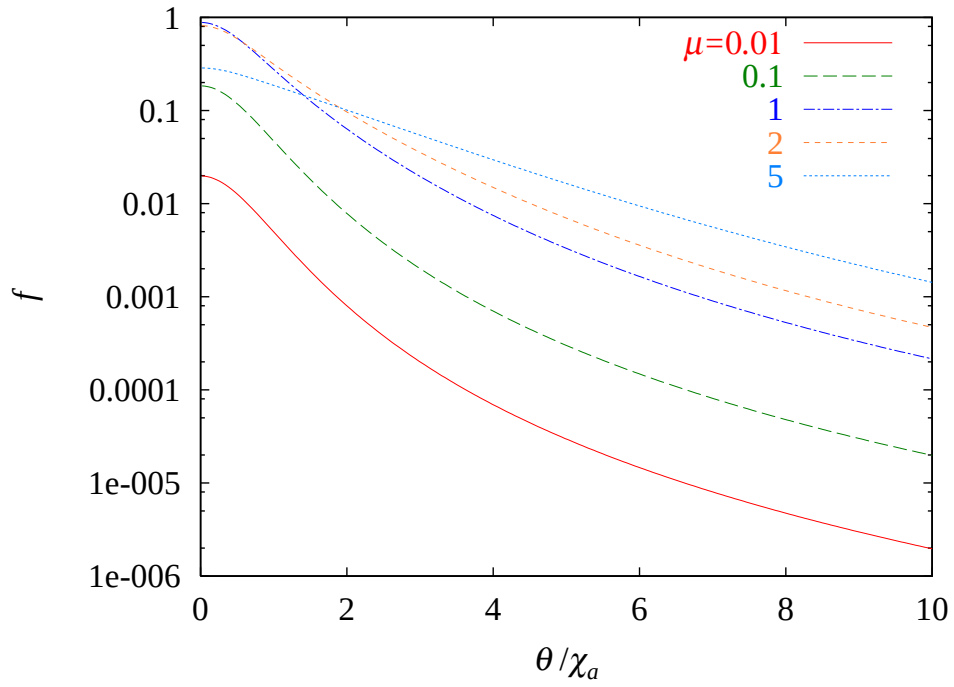

Figure 3: NI of eq. (1) for $\mu = 0.01$, 0.1, 1, 2 and 5

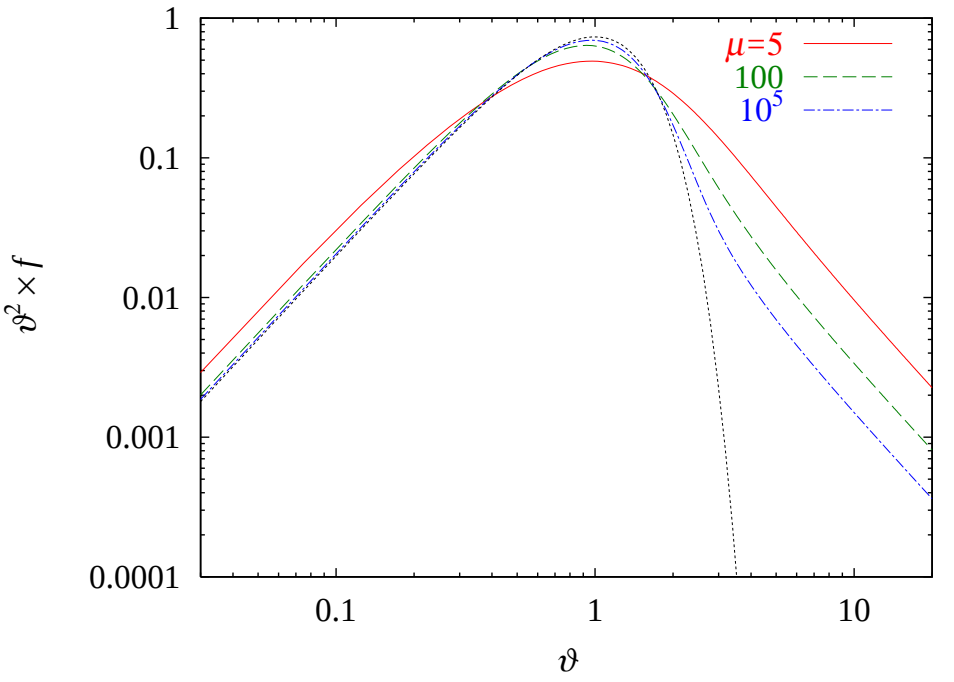

Figure 4: NI of eq. (1) for $\mu = 5$, 100 and 10^5.

Table 1: The maximum error of the multiple Coulomb scattering distribution.

μ	20	100	1000
Molière theory	~ 5 %	~ 2 %	~ 0.8 %
Monte Carlo	~ 2 %	~ 1 %	~ 0.7 %

4 Results

Using the exact multiple Coulomb scattering distribution, we examine the error of multiple Coulomb scattering distribution obtained by the Molière theory and by our Monte Carlo method [9]. To calculate the Molière distribution, three terms $f^{(0)}$ to $f^{(2)}$ are used since the additional terms do not improve the accuracy for the small step size cases [17]. (If the number of scattering is not very large, the assumption $\chi_0 \ll \chi_c$ used for deriving eq. (2) is not very good.)

Figures 5, 6 and 7 show the error of the projected angular distribution for $\mu = 20$, 100 and 1000 respectively. The maximum values of the error are tabulated in table 1. It can be seen that the accuracy of our Monte Carlo method is better than that of Molière's theory for $\mu \leq 100$. For $\mu = 1000$, the errors in the central region ($\varphi < 2$) of the both distributions are less than one percent. (We neglect the relatively large statistical error of the Monte Carlo distribution in the tail region since large angle scattering is sampled exactly according to the cross section [7, 9].)

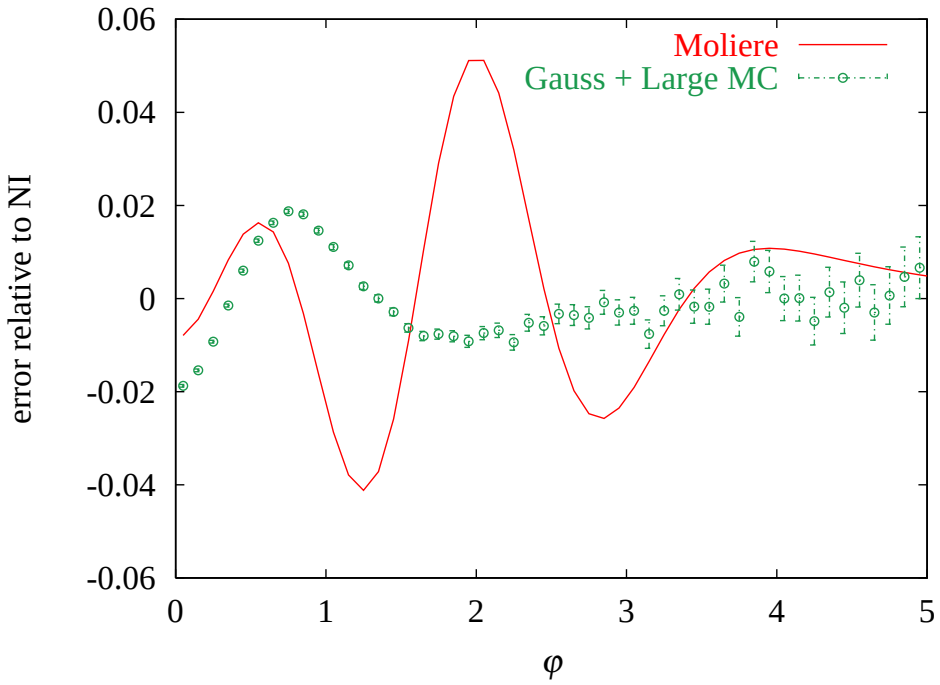

Figure 5: The error of multiple Coulomb scattering distribution obtained by the Molière theory (solid curve) and by our Monte Carlo method (circle) for $\mu = 20$.

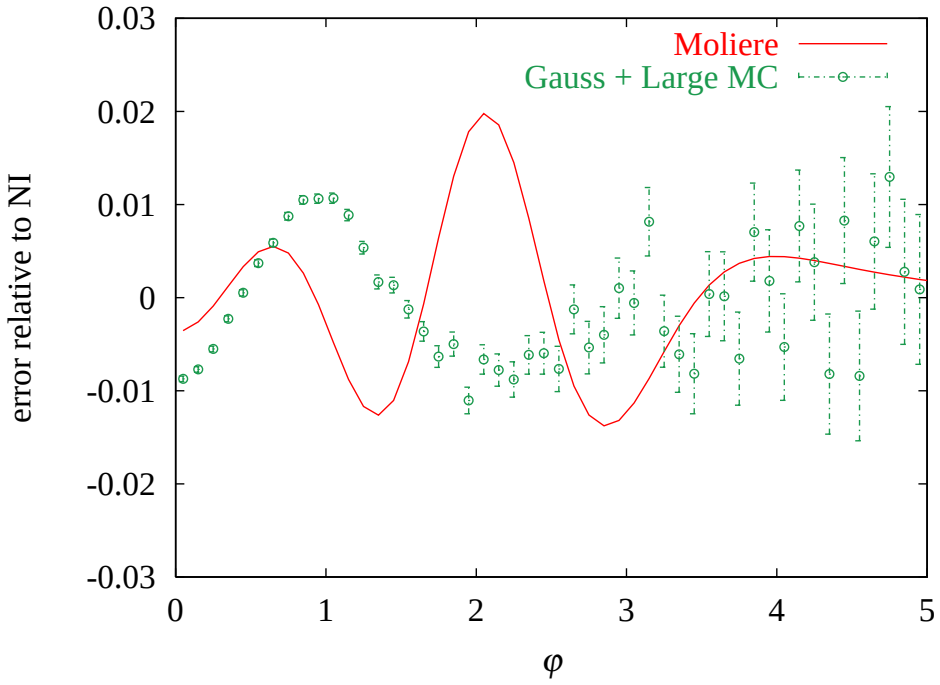

Figure 6: The error of multiple Coulomb scattering distribution obtained by the Molière theory (solid curve) and by our Monte Carlo method (circle) for $\mu = 100$.

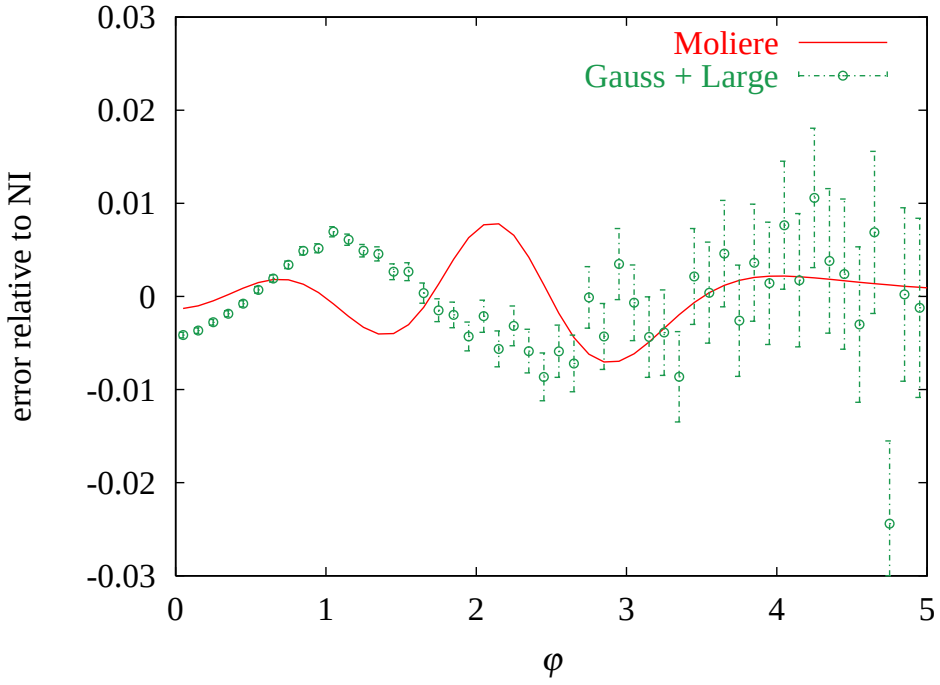

Figure 7: The error of multiple Coulomb scattering distribution obtained by the Molière theory (solid curve) and by our Monte Carlo method (circle) for $\mu = 1000$.

References

[1] W.R. Nelson, D.W.O. Rogers and H. Hirayama, *The EGS4 Code System*, Stanford Linear Accelrator report SLAC-265 (1985).

[2] *GEANT Detector Description and Simulation Tool*, CERN Program Library Long Writeup, PHYS325 (1993).

[3] G. Molière, *Z. Naturforsch.* **2a**, 133 (1947).

[4] G. Molière, *Z. Naturforsch.* **3a**, 78 (1948).

[5] H.A. Bethe, *Phys. Rev.* **89**, 1256 (1953).

[6] T. Nakatsuka and K. Okei, *Proc. 11th EGS4 User's Meeting in Japan*, KEK Proceedings 2003-15, 1 (2004).

[7] K. Okei and T. Nakatsuka, *Proc. 11th EGS4 User's Meeting in Japan*, KEK Proceedings 2003-15, 9 (2004).

[8] T. Nakatsuka and K. Okei, *Proc. 3rd International Workshopn on EGS*, KEK Proceedings 2005-3, 47 (2005).

[9] K. Okei and T. Nakatsuka, *Proc. 3rd International Workshopn on EGS*, KEK Proceedings 2005-3, 57 (2005).

[10] T. Nakatsuka and K. Okei, *Proc. 12th EGS User's Meeting in Japan*, KEK Proceedings 2005-10, 1 (2005).

[11] T.Ooura and M.Mori, *Journal of Computational and Applied Mathematics* **38**, 353 (1991).

[12] T.Ooura and M.Mori, *Journal of Computational and Applied Mathematics* **112**, 229 (1999).

[13] M. Abramowitz and I.A. Stegun, *Handbook of mathematical functions*, Dover pub. (1972).

[14] I.S. Gradshteyn and I.M. Ryzhik, *Table of Integrals, Series, and Products 6th edition*, Academic press (2000).

[15] W.T. Scott, *Rev. Mod. Phys.* **35**, 231 (1963).

[16] A.F. Bielajew, *Nucl. Instr. and Meth. in Phys. Res. B* **86**, 257 (1994).

[17] P. Andreo, J. Medin and A.F. Bielajew, *Med. Phys.* **20**, 1315 (1993).

Investigation of the Variation of the Reading Value by Absorbed Dose in the Glass Rod Dosimeter Using EGS4

Y. Shiota[1)], K. Tabushi[1)], N. Kadoya[1)] and Y. Aoyama[1)]

[1)] *Department of Radiological Technology, Graduate School of Medicine, Nagoya University, 461-8673, Japan*
e-mail: y.shiota@gmail.com

Abstract

A radiophotoluminescent (RPL) glass dosimeter is used for the radiation dosimetry in various energy. The measurement principles and properties of a RPL glass are similar to a thermoluminescent dosimeter (TLD). The commercialized system is composed of the RPL glass rod dosimeter (GRD) and the reading system [2]. The RPL GRD has the variation in the reading value such as TLD. This paper reports the variation from the reading system in dosimetry of radiotherapy. It is difficult to calculate the amount of the RPL, and it is known there is a proportional relation between the absorbed dose and the amount. Therefore the reading value was regarded as the total absorbed dose in the excitation area. The reading value was estimated from the absorbed dose calculated by EGS4.The reading value was estimated from the absorbed dose calculated by EGS4 and the absorbed dose was the total absorbed dose in the area of reading out that was in the absorbed dose distribution in the glass. The variation of the reading value was about 1 %, because the automatic reading system does not read the RPL at the same position every time. However, the magnitude of the variation is small. Therefore the accuracy of a measurement would not widely be affected.

1. Introduction

A radiophotoluminescent (RPL) glass dosimeter is used for the radiation dosimetry in various energy. When the RPL glass is irradiated, a RPL center is generated. It emits the orange RPL when it is excited by the radiation of the ultraviolet beam. The amount of the emitted orange RPL is proportional to the absorbed dose of the RPL glass [1]. The measurement principles and properties of the RPL glass are similar to a thermoluminescent dosimeter (TLD). The advantage of the RPL glass is that the repetitive reading is possible. The commercialized system is composed of the RPL glass rod dosimeter (GRD) and the reading system [2]. The RPL GRD is used to measure absorbed dose at extreme small volume in radiotherapy because the size is small and the energy dependence is good [3]. However, the RPL GRD has the variation in the reading value such as TLD. The detail of the variation is significant to understand the RPL GRD properties.

The RPL GRD system automatically reads the value with the special magazine and the N_2 gas laser for excitation of RPL center. The diameter of the laser is smaller than that of the GRD. The excitation area in the RPL glass changes due to the position where the laser passes. Moreover, it brings a change of emitted orange RPL amount. This paper reports the variation from the reading system in dosimetry of radiotherapy.

2. Materials and method

2.1 EGS4 simulation

In this work, we simulated the model GD-301 glass rod dosimeter (Asahi Techno Glass Corporation, Shizuoka, Japan) by Monte Carlo code EGS4 [2, 4]. Its size was 1.5 mm in diameter and 8.5 mm in length (Figure 1). The geometry was typical condition, the source surface distance (SSD) was 100 cm and the phantom size was 30 x 30 x 30 cm^3 (Figure 2). The phantom material was polymethylmethacrylate (PMMA) because the GRD was small and it was difficult to set it accurately in the water on actual measurement. The incident beam was Cobalt-60 gamma-rays (1.17, 1.33 MeV), 4 MV, and 10MV X-rays [5], and the size of irradiation field was 10 x 10 cm^2 on the phantom surface. The ECUT and the PCUT were 0.521 (include the rest energy) and 0.001 MeV, respectively. The material properties such as densities, ECUT and PCUT were shown in Table 1. The GRD was located at 0.5 and 5.0 cm depth in PMMA phantom and the dose distribution in the glass region was calculated.

2.2 Estimation of the variation in the reading value

It is difficult to calculate the amount of the orange RPL, and it is known there is a proportional relation between the absorbed dose and the amount. Therefore the reading value was regarded as the total absorbed dose in the excitation area. The reading value was estimated from the absorbed dose calculated by EGS4. The area of reading out is 1 mm diameter in the RPL glass, because the diameter of the N_2 gas laser in the RPL GRD system is 1 mm. The variation of the reading value was evaluated by the fluctuation of the total dose from the shift of the 1 mm diameter region. The shift wide was selected 0.1 mm, and the schematic diagram is presented in Figure 3. The relative error was calculated by the following formula. The direction of the shift was applied to only the beam axis, because this situation was the maximum fluctuation.

$$Rerative \;\; error = \frac{D_{shift} - D_{center}}{D_{center}} \times 100 \;\; [\%]$$

where, D_{center} is the total absorbed dose in the excitation area at the center position, and D_{shift} is that at the shift position.

3. Results and discussions

3.1 Dose distributions in the glass rod dosimeter

Figure 4 shows absorbed dose distributions with each incident energy at 0.5 cm depth and Figure 5 shows them at 5.0 cm depth. These data were normalized the dose at the 0.075 mm depth on the central axis in the GRD. The dose profile curves on the beam axis are shown in Figure 6. These profile had the gradient, and its range is 10 ~ 20 %. In the left side of Figure 6, a build-up observed only in 10 MV X-ray. If 4 or 10 MV X-ray is irradiated to the water phantom, 0.5 cm depth is in the build up region. However, the central axis depth dose of 4 MV X-ray decreased as the depth was deeper. This is concerned with the average energy of initial photon. The average energy of 4 MV and 10 MV are about 1.4 and 3.1 MeV, respectively. The average energy of 4 MV is nearly equal to that of Cobalt-60. Therefore, the dose profile curve of 4 MV is similar to that of Cobalt-60.

3.2 The variation of the reading value

Table 2 shows the relative error caused by the shift of the excitation area. The variation of the reading value was about 1 %, because the automatic reading system does not read the RPL at the same position every time. However, the magnitude of the variation is small. Therefore the accuracy of a measurement would not widely be affected.

4. Conclusion

By EGS4 simulation, we calculated the dose distributions in the RPL GRD. The gradient of the dose profile curves were obtained in the very small 1.5 mm diameter of the GRD. The accuracy of a measurement would not widely be affected because the magnitude of the variation is small.

References

1) Masayuki Tsuda, "A Few Remarks on Photoluminescence Dosimetry with High Energy X-Rays" Jpn.J.Med.Phys Vol.20. No.3, 2000
2) Asahi Techno Glass Corporation, "Explanation material of RPL glass dosimeter: small element system" Tokyo, Japan, 2003
3) Fujio Araki et al, "Dosimetric properties of radioluminesecent glass rod detector in high-energy photon beams from a linear accelerator and Cyber-Knife" Med.Phys.31, July 2004
4) R. Nelson, H. Hirayama, and D. W. O. Rogers, "The EGS4 Code System" SLAC-265 (Stanford Linear Accelerator Center), Stanford, Ca, 1985
5) Daryoush Sheikh-Bagheri and D. W. O. Rogers, "Monte Carlo calculation of nine megavoltage photon beam spectra using the BEAM code" Med.Phys.29, March 2002

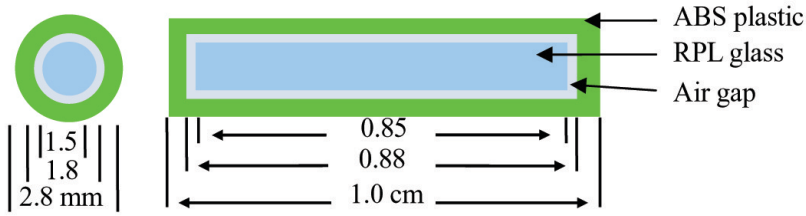

Figure 1.The schema of the model GD-301.

Table 1. Material data

	Density [g/cm^3]	ECUT [MeV]	PCUT [MeV]
AIR	0.12 × 10^{-2}	0.521	0.001
PMMA	1.19		
ABS Plastic	1.05		
RPL Glass	2.61		

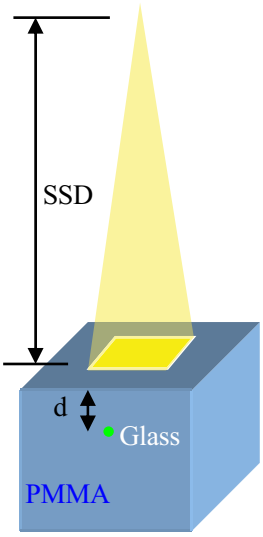

Figure 2. Geometry

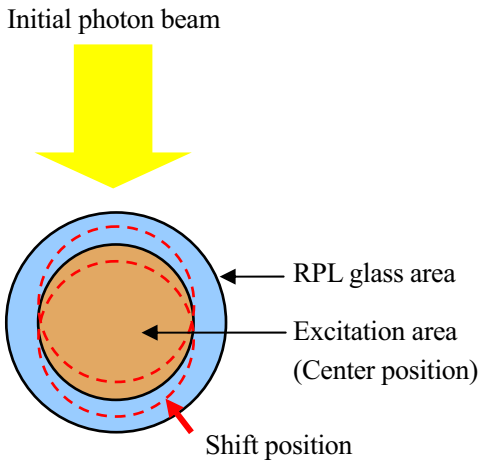

Figure 3. The schematic diagram of the shift

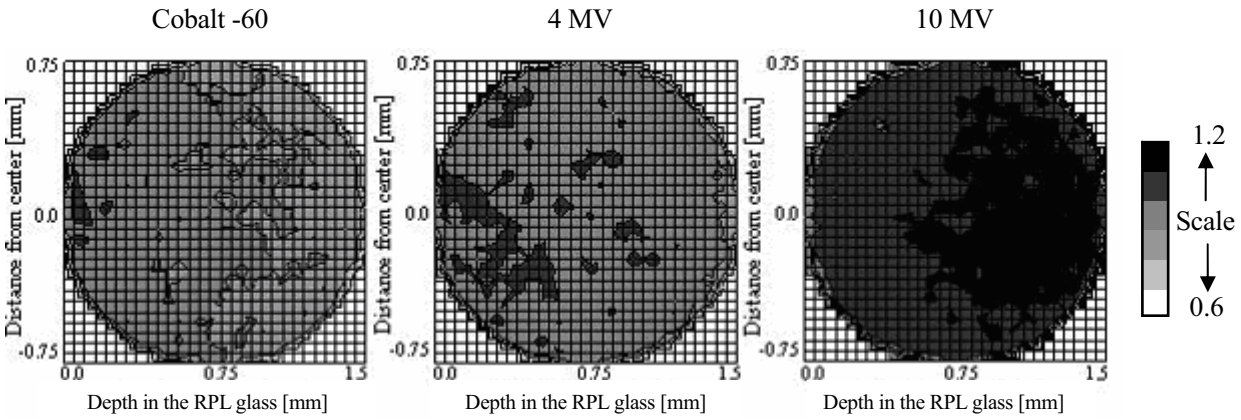

Figure 4. The dose distribution in the RPL glass at 0.5 cm depth in the phantom.

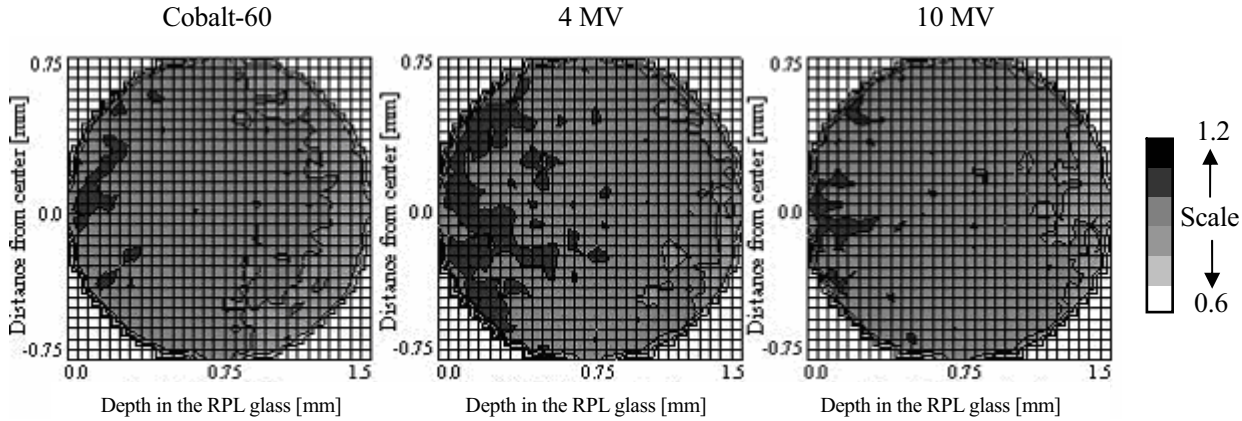

Figure 5. The dose distribution in the RPL glass at 5.0 cm depth in the phantom.

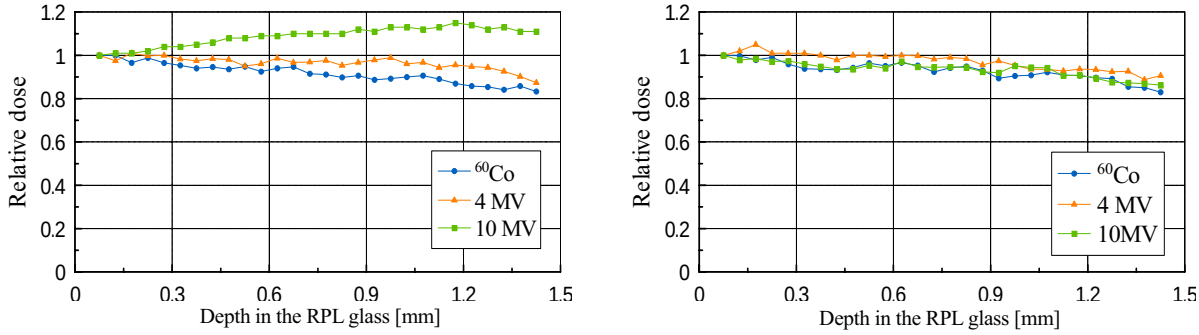

Figure 6. Depth dose profile in the RPL glass. The left side is at 0.5 cm depth of the GRD, and the right side is at 5.0 cm depth of the one.

Table 2. The relative error caused by the shift of excitation area

		The shift wide [mm]	
		- 0.1	0.1
0.5 cm depth	^{60}Co	1.05 %	- 0.95 %
	4MV	0.33 %	- 0.61 %
	10MV	- 1.03 %	0.71 %
5.0 cm depth	^{60}Co	0.92 %	- 0.88 %
	4MV	0.79 %	- 1.10 %
	10MV	0.69 %	- 0.75 %

Effective energy evaluation in the low-energy X-rays domain by an OSL dosimeter

Akira Suzuki *,Kichirou Koshida, Kimiya Noto, Ikuo Kobayashi[1)]

[*]Tel: +81-76-234-4366
Email: hokumeiryou@hotmail.co.jp

Division of Health science , Graduate School of Health Sciences,
Kanazawa University, Kanazawa, Japan
[1)]Nagase Lannauer . Ltd.

Abstract

Optically stimulated luminescence (OSL) individual exposure dosimeters (InLight Badge) are used for management of low-energy X-ray exposure. When using these dosimeters, the effective energy must be estimated based on the response ratio between filters irradiated with discrete photons. However, X-ray irradiation is really a continuous-spectrum energy source. Therefore, it is thought that there will be errors in estimation of the effective energy based on calculations using single energy photons. We calculated the effective energy formula from an actual survey of mammography X-ray apparatus and single energy photons, and compared the precision of effective energy estimation using an OSL dosimeter under irradiation with single energy photons and with continuous-spectrum energy. Since it was found that the value would be reduced if the ratio of response using the formula for single energy photons irradiation were used with continuous-spectrum energy, compensation for this error is required.

1. Introduction

Breast cancer is the most common type of cancer in women and the incidence is increasing. Therefore, the requirement for medical checkups for breast cancer is also increasing. However, it is possible that medical staff, i.e., radiological technologists, etc., will be exposed to low-energy X-rays with a tube voltage of 23-35 kV (effective energy 15-21 keV) generated from the X-ray mammography equipment. Optically stimulated luminescence (OSL) individual exposure dosimeters (InLight Badge) are used for management of low-energy X-ray exposure, but these dosimeters estimate the effective energy based on the response ratio between filters irradiated with discrete photons. However, X-ray irradiation is really a continuous-spectrum energy source. Therefore, it is thought that there will be errors in estimation of the effective energy based on calculations using single energy photons. We calculated the effective energy formula from an actual survey of mammography X-ray apparatus and single energy photons, then compared the precision of effective energy estimation using the OSL dosimeter under irradiation with single energy photons and with continuous-spectrum energy.

2. Materials

GE mammography X-ray apparatus was used (GE Company DMG). The dosimeters were irradiated under the following conditions: Mo-Mo 23 kV-35 kV (17.78 keV-19.84 keV), Mo-Rh 27 kV-35 kV (19.76 keV-20.66 keV), Rh-Rh 29 kV-35 kV (19.97 keV-21.34 keV). We used BL14C1 of the synchrotron orbital radiation facilities of the High Energy Accelerator Research Organization in survey of the single photon. The irradiation energy was 8 - 40keV. We used an OSL dosimeter (InLightBadge) with aluminum and plastic filters. In addition, we used an EGS4 cord provided by the High Energy Accelerator Research Organization for Monte Carlo simulation. One million or more photons were generated in the simulation. Standard deviation was less than ±10%. The irradiation conditions of the simulation were set to 15 keV-21 keV. We investigated the continuous-spectrum energy using the formula proposed by Boone.

3. Methods

The simulation involved irradiation with continuous-spectrum energy and single energy photons under the conditions described above. Using the response ratio between the two filters, we determined the formula for

effective energy estimation. We substituted the response ratio of the continuous-spectrum energy determined in the calculation for each formula and examined the precision criteria of the calculation formula. In the survey of single energy photons, we respectively irradiated three OSL dosimeters at each effective energy under the conditions described above. In the survey of continuous-spectrum energy, we respectively irradiated five OSL dosimeters at each effective energy under the conditions described above. We used the response ratio between filters to determine the effective energy calculation formula. We substituted the response ratio between filters, which was obtained from the calculation formula, then determined the precision criteria of the calculation.

4. Results

The effective energy calculation formula was investigated by simulation of single energy photons. Fig. 1 shows the approximated curve from each effective energy calculation formula. The calculation formula to determine the effective energy was obtained from the ratio of the response without the filter to that with an aluminum filter.

$$E = -0.3287x(No/Al)^4 - 4.3023\ x(No/Al)^3 + 21.345x(No/Al)^2 - 49.003x(No/Al) + 60.741$$

The calculation formula to determine the effective energy was also obtained from the ratio of the response with the plastic filter to that with the aluminum filter.

$$E= -0.3165x(Pl/Al)^4 - 4.1843x(Pl/Al)^3 + 20.975x(Pl/Al)^2 - 48.575x(Pl/Al) + 60.447$$

where E is the effective energy in keV, No is the response without the filter, Pl is the response with the plastic filter, and Al is the response with the aluminum filter. The calculated result using the response of each filter obtained in the simulation using single energy photons in each formula is shown in a Table1-1. Moreover, inserting the response ratio of No/Al on simulation using single energy photons into the effective energy calculation formula gave an error of SD ±0.04keV. Insertion of the response ratio of Pl/Al on simulation of single energy photons into the effective energy calculation formula gave an error of SD ±0.06 keV. As the error was small, the accuracy of the formula was considered good.

After substituting the ratio of the response on simulation using continuous-spectrum energy, the formula yielded the results shown in Table 1-2. Insertion of the response ratio of No/Al on simulation using continuous-spectrum energy into the formula yielded a low average of 0.79keV. Insertion of the response ratio of Pl/Al on simulation using continuous-spectrum energy yielded a low average of 0.77keV.

When continuous-spectrum X-rays were evaluated using a single photon, the calculated energy value was actually lower. Substituting the response ratio of the measurement of single energy photons in the formula yielded the results shown in Table 1-3. The insertion of the response ratio of No/Al on simulation using single energy photons into the effective energy calculation formula yielded an error of SD ±065keV. Insertion of the response ratio of Pl/Al using single energy photons into the effective energy calculation formula yielded an error of SD ±0.79keV. This indicates that simulation accuracy is good.

The effective energy calculation formula was investigated by simulation of continuous-spectrum X-rays. Each approximated curve from the effective energy calculation formula is shown in Fig. 2. The formula to determine the effective energy was obtained from the response ratio without the filter to that with an aluminum filter.

$$E =0.511x(No/Al)^4-7.0075x\ (No/Al)^3+26.634x(No/Al)^2-81.154x(No/Al)+87.608$$

The calculation formula to determine the effective energy was also obtained from the response ratio with the plastic filter to that with the aluminum filter.

$$E=0.70918x(Pl/Al)^4 -9.2971x\ (Pl/Al)^3-45.1648x(Pl/Al)^2+97.931x\ (Pl/Al)+97.89$$

where E is the effective energy in keV, No is the response without the filter, Pl is the response with the plastic filter, and Al is the response with the aluminum filter.

After the response obtained with each filter during the simulation using continuous-spectrum X-rays was placed into each formula, the calculated results are shown in Table.2-1. Insertion of the response ratio of No/Al on simulation using continuous-spectrum energy into the effective energy calculation formula yielded an error of SD ±0.13keV. Insertion of the response ratio of Pl/Al on simulation using continuous-spectrum energy into the effective energy calculation formula yielded an error of SD ±0.17keV. As the error was small, the accuracy of the formula was considered good.

Substituting the response ratio using continuous-spectrum X-rays in the formula yielded the results shown in Table 2-2. Insertion of the response ratio of No/Al on simulation of c measurement using continuous-spectrum X-rays into the effective energy calculation formula yielded an error of SD ±0.29keV. Insertion of the response ratio of Pl/Al using continuous-spectrum X-rays into the effective energy calculation formula yielded an error of SD ±0.33keV. This indicates that the simulation accuracy is good.

The effective energy calculation formula was investigated by measurement of single energy photons. Each approximated curve from the effective energy calculation formula is shown in Fig. 3. The calculation formula to determine the effective energy was obtained from the response ratio without the filter to that with an aluminum filter.

$$E = -2.795x\,(No/Al)^3 + 23.534x(No/Al)^2 - 65.754x(No/Al) + 77.827$$

The calculation formula to determine the effective energy was also obtained from the response ratio with the plastic filter to that with the aluminum filter.

$$E = -3.865x\,(Pl/Al)^3 + 29.828x(Pl/Al)^2 - 77.332x\,(Pl/Al) + 84.094$$

where E is the effective energy in keV, No is the response without the filter, Pl is the response with the plastic filter, and Al is the response with the aluminum filter.

Inserting the response of each filter obtained by measurement of single energy photons into each formula yielded the results shown in Table.3-1. Insertion of the response ratio of No/Al on simulation using continuous-spectrum energy into the effective energy calculation formula yielded an error of SD ±1.47keV. Insertion of the response ratio of Pl/Al of the measurement of continuous-spectrum energy into the effective energy calculation formula yielded an error of SD ±1.02keV.

Substituting the response ratio of the measurement of continuous-spectrum energy in the formula yielded the results shown in Table 3-2. Insertion of the response ratio of No/Al on measurement of continuous-spectrum energy into the formula yielded a low average of 3.00keV. Insertion of the response ratio of Pl/Al on measurement of continuous-spectrum energy into the formula yielded a low average of 3.17keV. In a survey as well as by simulation, a low computed value for continuous-spectrum X-rays was shown.

Substituting the response ratio obtained by simulation using single energy photons in the formula yielded the results shown in Table 3-3. Insertion of the response ratio of No/Al on simulation of c measurement of single energy photons into the effective energy calculation formula yielded an error of SD ±0.28keV. Insertion of the response ratio of Pl/Al on measurement of single energy photons into the effective energy calculation formula yielded an error of SD ±0.29keV. This indicates that the simulation accuracy is good.

The effective energy calculation formula was investigated by measurement of continuous-spectrum X-rays. Each approximated curve from the effective energy calculation formula is shown in Fig. 4. The calculation formula to determine the effective energy was obtained from the response ratio without the filter to that with the aluminum filter.

$$E = 0.3515x(No/Al)^2 - 4.2505x(No/Al) + 28.798$$

The calculation formula to determine the effective energy was also obtained from the response ratio with the plastic filter to that with the aluminum filter.

$$E = 0.1238x(Pl/Al)^2 - 3.2369x(Pl/Al) + 27.322$$

where E is the effective energy in keV, No is the response without the filter, P1 is the response with the plastic filter, and Al is the response with the aluminum filter.

Substituting the response of each filter shown by measurement of continuous-spectrum X-rays into each formula yielded the results shown in Table.4-1. Insertion of the response ratio of No/Al into the formula yielded an error of SD ±0.22keV. Insertion of the response ratio of Pl/Al into the formula yielded an error of SD ±0.24keV. As the error was small, the accuracy of the formula was considered good.

Substituting the response ratio obtained by simulation using continuous-spectrum X-rays in the formula yielded the results shown in Table 4-2.

Insertion of the response ratio of No/Al obtained by simulation of c measurement of single energy photons into the effective energy calculation formula yielded an error of SD ±0.27keV. Insertion of the response ratio of Pl/Al obtained by measurement of single energy photons into the effective energy calculation formula yielded an error of SD ±0.39keV. This indicated that simulation accuracy is good.

Discussion

Findings on simulations using both single energy photons and continuous-spectrum X-rays were in agreement with the survey. As the value will be reduced if the response ratio using the formula for single energy photons irradiation is used for continuous-spectrum energy, compensation must be included in the formula.

Since measurements of a single photon were rough, it is necessary to measure energy gradually. In future studies, it will be necessary to survey the single photon of 8 - 15keV and 27 - 40keV again, and to consider whether accuracy may be increased by changing the thickness and type of filter used.

Conclusion

Optically stimulated luminescence (OSL) individual exposure dosimeters (InLight Badge) are used for management of low-energy X-ray exposure, but these dosimeters use an estimation of the effective energy based on the ratio of response between filters irradiated with discrete photons. However, X-ray irradiation is really a continuous-spectrum energy source. Therefore, it is thought that errors will occur in estimating the effective energy by calculations based on single energy photons. We calculated the effective energy formula from an actual survey of mammography X-ray apparatus and single energy photons, and compared the precision of effective energy estimation using the OSL dosimeter respectively irradiated with single energy photons and with continuous-spectrum energy. Insertion of the response ratio of No/Al obtained by simulation using continuous-spectrum energy into the effective energy calculation formula yielded an error of SD ±1.47keV. Insertion of the response ratio of Pl/Al obtained by measurement of continuous-spectrum energy into the effective energy calculation formula yielded an error of SD ±1.02keV. Insertion of the response ratio of No/Al obtained by measurement of continuous-spectrum energy into the formula demonstrated a low average of 3.00keV. Insertion of the response ratio of Pl/Al obtained by measurement of continuous-spectrum energy into the formula computed a low average of 3.17keV. In the survey as well as on simulation, a low computed value for continuous-spectrum X-rays was demonstrated.

As the value will be reduced if the response ratio using the formula for single energy photons irradiation is used with continuous-spectrum energy, compensation for this error must be incorporated in the formula.

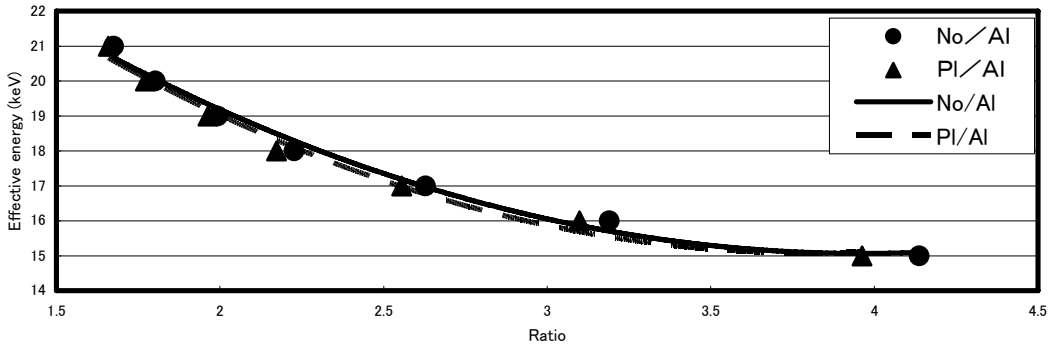

Fig.1 Estimation of the effective energy from the ratio between the filters by simulation with single energy photons

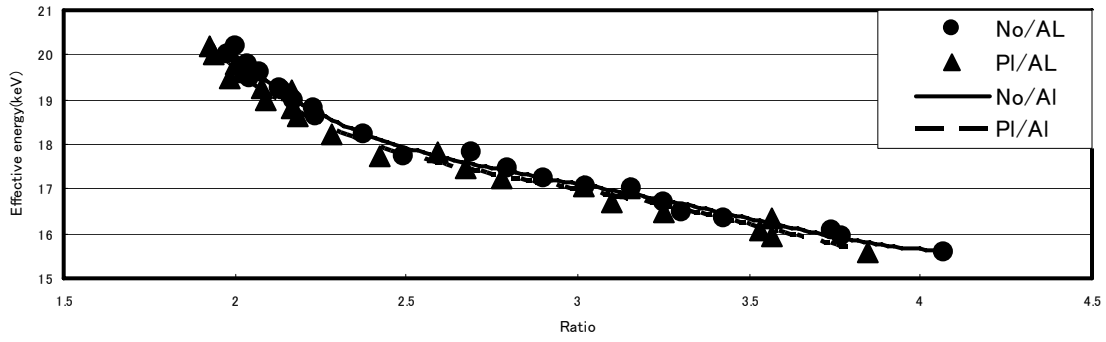

Fig. 2 Estimation of the effective energy from the ratio between the filters by simulation of continuous-spectrum radiation

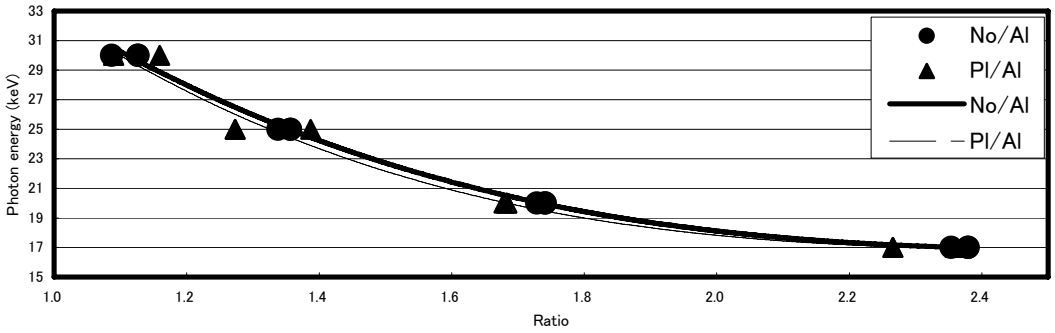

Fig. 3 Estimation of the effective energy from the ratio between the filters by measurement of single energy photons

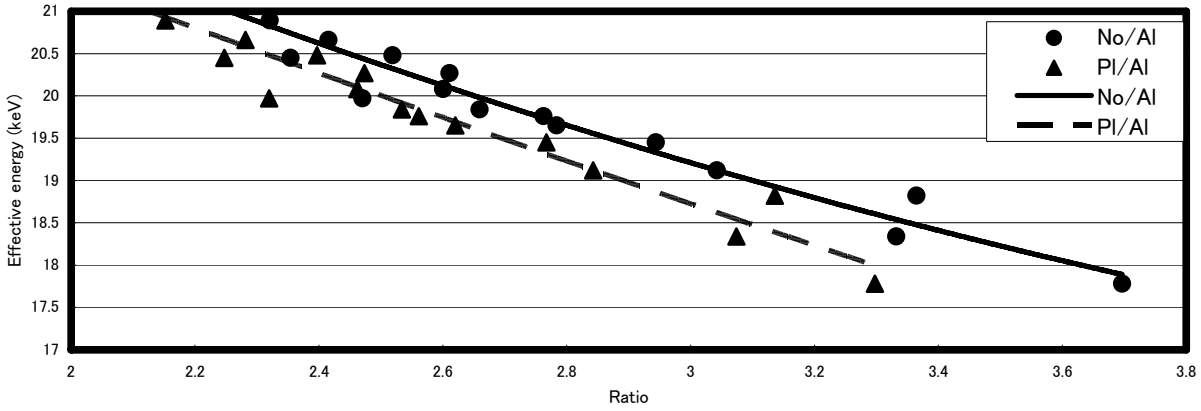

Fig. 4 Estimation of the effective energy from the ratio between the filters by measurement of continuous-spectrum X-rays radiation

Table 1-1 The calculated results after inserting the response of each filter obtained by simulation of single energy photons into each formula

keV	No/Al keV)	Pl/Al (KeV)
15	14.99	15.00
16	16.01	16.01
17	16.97	16.96
18	18.04	18.06
19	18.99	18.97
20	20.04	20.07
21	20.92	20.89

Table 1-2 The calculated results obtained by inserting the response of each filter on simulation of continuous-spectrum X-rays into each formula rather than simulation of single energy photons

KeV	No/Al(keV)	Pl/Al(keV)
15.57	15.01	15.09
15.93	15.24	15.39
16.09	15.28	15.43
16.36	15.67	15.39
16.48	15.85	15.79
16.71	15.92	16.01
17.03	16.05	15.93
17.04	16.26	16.13
17.23	16.46	16.52
17.47	16.64	16.71
17.73	17.28	17.27
17.82	16.84	16.89

KeV	No/Al(keV)	Pl/Al(keV)
18.22	17.58	17.68
18.62	18.01	18.03
18.81	18.03	18.09
19.00	18.25	18.39
19.21	18.37	18.09
19.25	18.39	18.43
19.49	18.77	18.85
19.62	18.63	18.69
19.77	18.77	18.78
20.02	19.05	19.08
20.18	18.95	19.15

Table1-3 The calculated results obtained by inserting the response of each filter on measurement of single photons into each formula rather than simulated values for single photons.

keV	No/Al	Pl/Al
17	17.68	16.96
20	20.64	20.68
23	23.16	23.59
25	24.52	24.02

Table.2-1 The calculated results obtained by inserting the response of each filter obtained by simulation of continuous-spectrum X-rays into each formula

keV	No/Al(keV)	Pl/Al(keV)
15.57	15.41	15.57
15.93	15.89	16.08
16.09	15.94	16.15
16.36	16.45	16.08
16.48	16.63	16.63
16.71	16.70	16.86
17.03	16.83	16.79
17.04	17.00	16.98
17.23	17.17	17.30
17.47	17.33	17.46
17.73	17.91	17.95
17.82	17.50	17.60

keV	No/Al(keV)	Pl/Al(keV)
18.22	18.24	18.35
18.62	18.73	18.74
18.81	18.76	18.81
19.00	19.02	19.16
19.21	19.18	18.81
19.25	19.20	19.21
19.49	19.69	19.74
19.62	19.51	19.53
19.77	19.70	19.65
20.02	20.06	20.05
20.18	19.93	20.14

Table2-2 The calculated results obtained by inserting the response of each filter obtained in the simulation of the continuous-spectrum X-rays into each formula rather than single photon values.

keV	No/Al(keV)	Pl/Al(keV)
17.78	16.01	16.56
18.34	16.58	16.90
18.82	16.54	16.81
19.12	16.98	17.22
19.45	17.11	17.32
19.65	17.35	17.55
19.76	17.38	17.66
19.84	17.56	17.71

keV	No/Al(keV)	Pl/Al(keV)
19.97	17.97	18.24
20.08	17.67	17.86
20.27	17.65	17.83
20.45	18.30	18.48
20.48	17.85	18.02
20.66	18.12	18.36
20.89	18.42	18.86
21.34	18.66	18.95

Table.3-1 The calculated results obtained by inserting the response of each filter on measurement of single energy photons into each formula

keV	No/Al(keV)	Pl/Al(keV)
17	17.06	16.95
20	20.23	19.98
23	25.09	24.14
25	25.87	24.81
30	30.10	29.37

Table 3-2 The calculated results obtained by inserting the response of each filter on measurement of the continuous-spectrum X-rays into each formula rather than measured values for single energy photons

keV	No/Al (keV)	Pl/Al (keV)
17.78	15.29	14.85
18.34	16.71	15.96
18.82	16.64	15.72
19.12	16.97	16.52
19.45	16.97	16.61
19.65	16.92	16.72
19.76	16.91	16.76
19.84	16.88	16.78

keV	No/Al (keV)	Pl/Al (keV)
19.97	16.91	16.97
20.08	16.88	16.82
20.27	16.88	16.82
20.45	17.03	17.08
20.48	16.89	16.88
20.66	16.95	17.02
20.89	17.08	17.29
21.34	17.20	17.35

Table3-3 The calculated results obtained by inserting the response of each filter on simulation of single energy photons into each formula rather than that from measured values for single energy photons.

keV	No/Al (keV)	Pl/Al (keV)
17	16.88	16.76
18	17.27	17.24
19	18.15	17.99
20	19.42	19.22
21	20.60	20.26

Table.4-1 The calculated results obtained by inserting the response of each filter on measurement of

continuous-spectrum X-ray into each formula.

keV	No/Al (keV)	Pl/Al (keV)
17.78	17.89	17.99
18.34	18.54	18.54
18.82	18.48	18.39
19.12	19.12	19.12
19.45	19.33	19.31
19.65	19.69	19.69
19.76	19.74	19.84
19.84	19.98	19.92

keV	No/Al (keV)	Pl/Al (keV)
19.97	20.44	20.48
20.08	20.12	20.10
20.27	20.10	20.07
20.45	20.74	20.67
20.48	20.32	20.27
20.66	20.58	20.58
20.89	20.83	20.93
21.34	21.00	20.98

Table4-2 The calculated results obtained by inserting the response of each filter on simulation of continuous-spectrum X-ray into each formula rather than measured values for continuous-spectrum X-rays.

keV	No/Al (keV)	Pl/Al (keV)
15.57	17.32	16.70
15.93	17.77	17.35
16.09	17.82	17.43
16.36	18.37	17.35
16.48	18.60	18.10
16.71	18.69	18.47
17.03	18.88	18.35
17.04	19.16	18.68
17.23	19.43	19.28
17.47	19.66	19.55
17.73	20.39	20.20
17.82	19.90	19.77

keV	No/Al (keV)	Pl/Al (keV)
18.22	20.69	20.58
18.62	21.05	20.85
18.81	21.07	20.90
19	21.23	21.10
19.21	21.33	20.90
19.25	21.33	21.13
19.49	21.59	21.38
19.62	21.50	21.29
19.77	21.59	21.34
20.02	21.76	21.51
20.18	21.70	21.54

INVESTIGATION OF SIMULATION OF CHERENKOV LIGHT WITH EGS

N. Kadoya, K. Tabushi

Department of Radiological Technology, Graduate School of Medicine, Nagoya University
e-mail: Noriyuki_Kadoya@yahoo.co.jp

Abstract

When a charged particle moves at velocity faster than the speed of light in water, a faint radiation is produced from water. It is called Cherenkov light. This phenomenon is mostly used in study of engineering and physics. However, it is not very useful in study of medicine. Therefore, we thought whether Cherenkov light can be used in medical treatment and we carried out many experiments where we measured Cherenkov light. In this study, in order to check the accuracy of the experimental result we tried to simulate Cherenkov light with EGS. In comparison with Cherenkov photon calculated with EGS, the measured value was almost the same as it in the irradiation field, however, outside the irradiation field, a difference was found. The discrepancy between calculated and measured values was considered to be caused by the measurement deviation. Moreover, not taking account of the decrease of the light by water in simulation may also influence the difference. The Cherenkov photon calculated with EGS5 were closer to an actual measurement than those calculated with EGS4. It is thought that, by introducing Energy hinge and MS hinge, transportation of the electron in the simulation became close to transportation of an original electron, and the calculated value might approach the measured value.

1. Introduction

When a charged particle moves at velocity faster than the speed of light in water, a faint radiation is produced from water. It is called Cherenkov light [1]. The light propagates away in a cone forward of the place where the interaction took place. This phenomenon is mostly used in study of engineering and physics. However, it is not very useful in study of medicine. Therefore, we thought whether Cherenkov light can be used in medical treatment and in the experiment carried out before, the distribution of Cherenkov light which was generated by Co-60 gamma-rays in water was similar to that of absorbed dose in water of Co-60 gamma-rays[2]. Therefore, we noted the relation of the absorbed dose and Cherenkov light and currently conducted the experiment where we investigated whether absorbed dose distribution of water of a section could be indirectly measured by acquiring the emission CT image of Cherenkov light generated from water of the section.

In this study, in order to check the accuracy of the experimental result we tried to investigate whether the simulation of Cherenkov light can be carried out using EGS.

2. Materials and Methods

2.1 Acquisition method of emission CT of Cherenkov light

We tried to get the image of emission CT based on Cherenkov light generated from water using the Linear

accelerator (Mitubishi, EXL-15SP). The irradiation beam was set at X-rays (10MV).When the light passed through the collimator which was set outside the water phantom, it was measured with the film (Fig.1). The distance from the radiation source to the center of the collimator was 100cm. The water phantom, which was the aquarium made of glass, was 25×20×25cm^3.The collimator was located at 3 cm below the surface of water. It was consisted of the thirty prisms; the outer size of the prism was 5×5mm^2 and the aperture size was 4×4 mm^2. The length of the prisms was 4.4 cm and then aluminum and lead boards were attached on and under the collimator (Fig.2). Moreover, as the turn table was rotated at step of 15 degrees, 24 films were used for the experiment. A radiation dose was 125cGy and the films were got from 0 to 345 degrees. Then 24 films were read and the film densities were changed to the light exposure. The image was reconstructed using back projection with Sheep & Logan Filter created by Fortran and we obtained Cherenkov CT image (CCT image).

2.2 Simulation Method for Cherenkov photon

The Monte Carlo code was EGS4 and EGS5. The geometry of simulation was the same as that of the experiment. The irradiation beam was set at 10MV X-ray (mitubishi.EXL-15SP). The cut-off energies for transport calculation of electron (ECUT) and photon (PCUT) in all calculations of this study were set to 775 keV and 264keV, respectively. The statistical error in all calculation was set below 1 %. It was necessary to modify subroutine AUSGAB to calculate Cherenkov photon [3]. Fig.3 gives the flow chart of additional program. This subroutine is called whenever an event (photoelectric effect, compton effect, electron pair production and change of the region of interest..et.al) takes place.

In this subroutine, we checked first two conditions:

1. The particle has the charge.
2. The kinetic energy of the particle is over the threshold (264keV).

Only if these conditions were satisfied, subroutine cherenkov was called. In subroutine cherenkov, emission angle θ was calculated according to Eq.(1).

$$\cos\theta = \frac{c/n}{V} = \frac{c}{nV} \qquad (1)$$

Where n is the refractive index of medium and V is the velocity of the particle.
Moreover, we calculated Nc using Eq. (2).

$$\frac{dN_c}{ds} = 2\pi\alpha\int\frac{\sin^2\theta}{\lambda^2}d\lambda \qquad (2)$$

Where Nc is the Cherenkov photon emitted per path length ***S***.
In this wavelength band 350-500nm, this gives:

$$N_C = 390\sin^2\theta$$

In this simulation, we used this formula.
The total number of created photons was given by Nc multiplied per the transportation step of the charged particle in the medium. That is, Cherenkov photons were created along pathway of the charged particle. Then we counted the Cherenkov photons when IARG was equal to zero to avoid measuring the Cherenkov photon redundantly. In EGS4, the transportation step was TVSTEP and in EGS5, the step was USTEP. We counted the Cherenkov photon which was entering the place where the film was set (Fig.4).

The distance from originating point of Cherenkov photon to measuring plane was calculated and the inverse square law was taken into consideration using the distance.

3. Results

Figure 6 shows a comparison of the calculated with EGS4 and measured profile curves normalized to the max value at the arrangement like Fig.5. Although each has almost the same tendency, a difference is found outside the irradiation field. Next, In Fig.7 we show a comparison of the calculated with EGS5 and measured profile curves normalized to the max value. As for the profile curves calculated with EGS5, we show the two profile curves where the Characteristic distance are different. The Cherenkov photon calculated with EGS5 fits measured Cherenkov light more than those calculated with EGS4. In Fig.8 we compare the Cherenkov photon calculated with EGS4 to that calculated with EGS5. From this graph, the Cherenkov photon calculated with EGS5 is closer to the actual measurement than those calculated with EGS4. The calculated Cherenkov photon is not consistent with measured Cherenkov light outside the irradiation field.

4. Discussions

As for the calculated Cherenkov photon and measured Cherenkov light, although they were considerably similar to each other in the irradiation field, the difference was found out of the irradiation field. The discrepancy between the two values was considered to be caused by the measurement deviation. Moreover, not taking account of the decrease of the light by water in simulation may also influence the difference.

Next, the Cherenkov photon calculated with EGS5 was closer to the actual measurement than those calculated with EGS4. It is thought that, by introducing Energy hinge and MS hinge, transportation of the electron in the simulation became close to transportation of an original electron, and the calculated value might approach the measured value.

5. Conclusion

The simulation of Cherenkov photon was possible by using EGS. However, since the calculated values were correctly inconsistent with the measured values in this result, it is necessary to measure the values again and to examine them again. Moreover, from this result, in the simulation of Cherenkov light, EGS5 can calculate more correctly than EGS4.

References

1) P.A.Cerenkov (1937) Visible Radiation Produced by Electrons Moving in a Medium with Velocities Exceeding that of Light. Phys. Rev 52:pp378-379
2) N Kadoya, K Tabushi et al (2005) Trial of CT based on Cherenkov Radiation using Co-60 γ-rays, Jpn.J.Med.Phys.Proc.vol.25, 3, the 4th Japan-Korea Joint Meeting on Medical Physics:pp 404－407,
3) A. Mishev, E. Duverger, L. Makovicka.et al (2001) Modelling and study of the Cherenkov effect, Radiation Physics and Chemistry 61:371-373

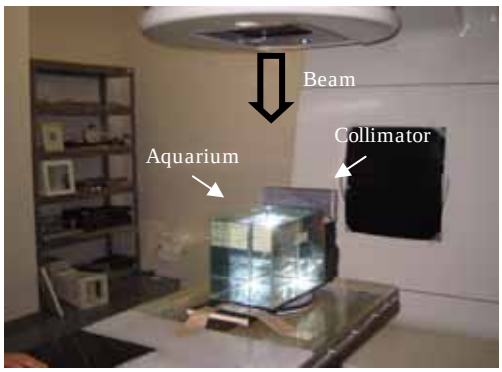

Fig.1 Arrangement of the experiment

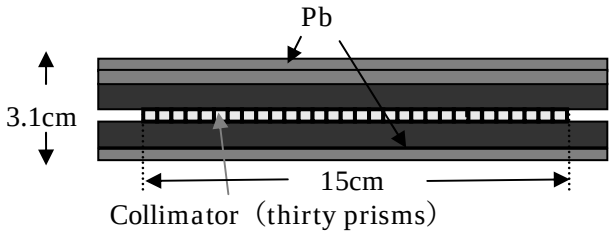

Fig.2 Structure of collimator.

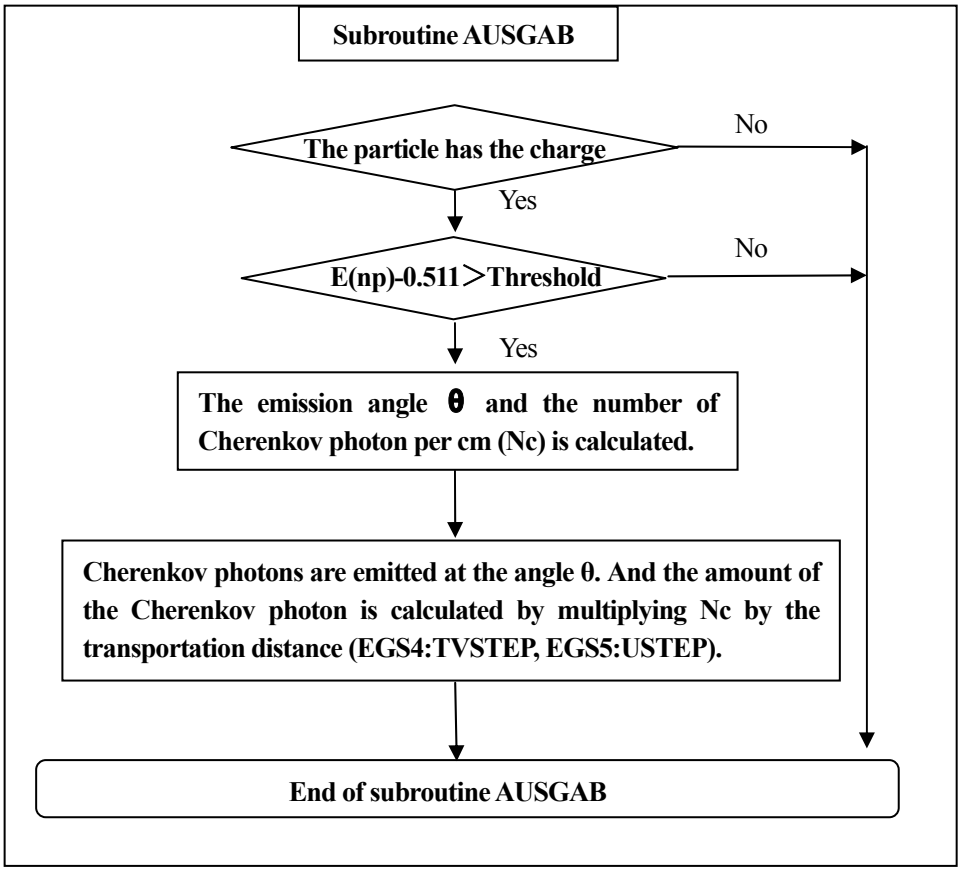

Fig.3 Flow diagram of simulation of Cherenkov photon

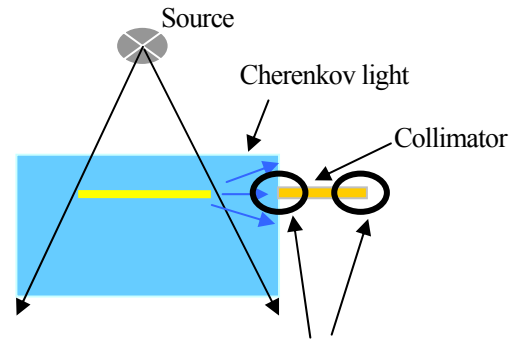

Fig.4 The count method of Cherenkov photon

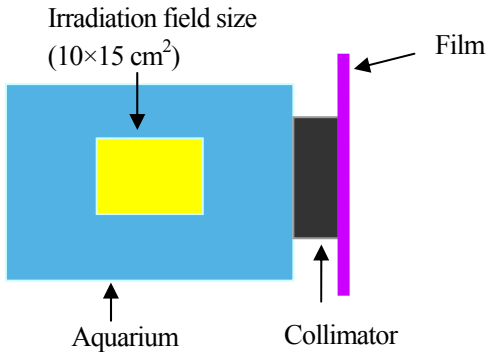

Fig.5 Experiment arrangement for acquirement of the profile curve.

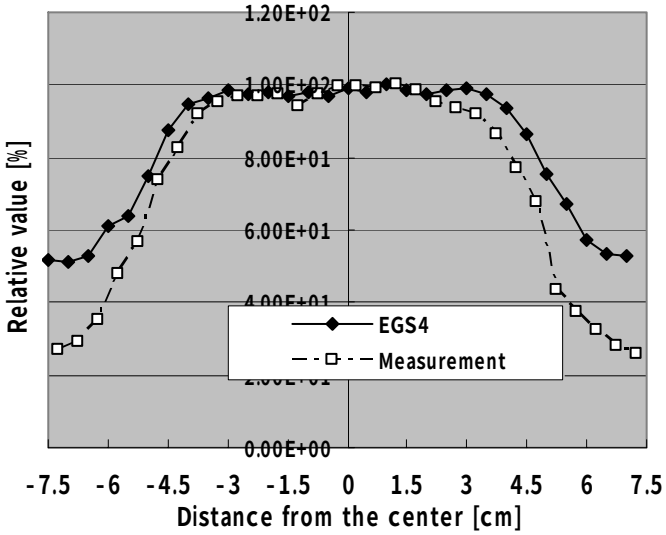

Fig.6 Comparison of Cherenkov light obtained from the simulation with EGS4 and that of the measurement.

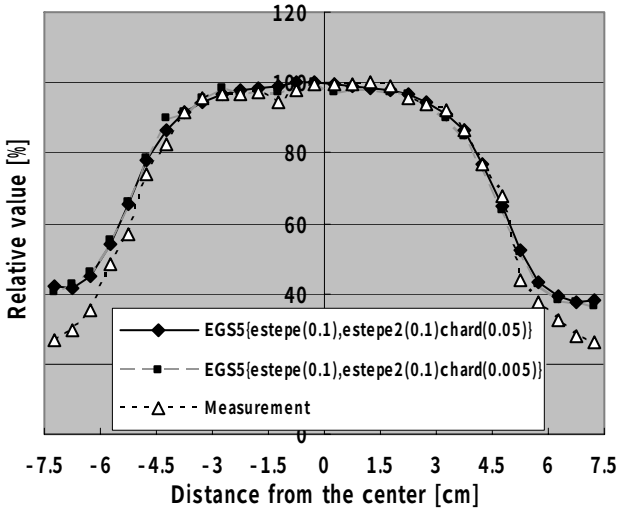

Fig.7 Comparison of Cherenkov light obtained from the simulation with EGS5 and that of the measurement.

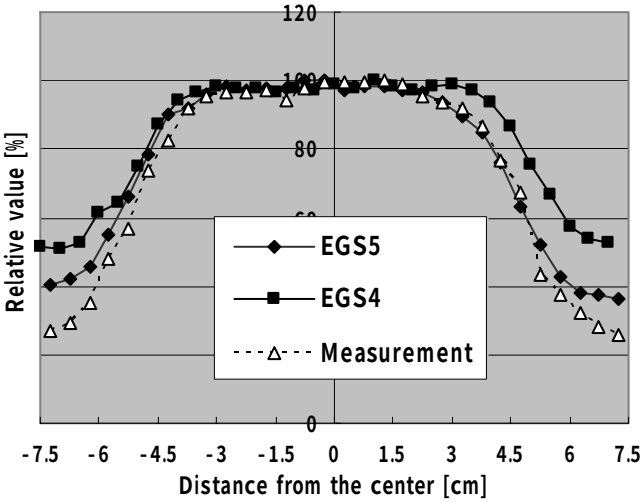

Fig.8 Comparison of Cherenkov light obtained from the simulation with EGS4 , that with EGS5 and that of the measurement.

NEW DEVELOPMENT OF HIGH-ENERGY X-RAY PRIMARY AND SCATTER DOSE KERNELS BY MONTE CARLO SIMULATION

Makoto Sasamori [1,2], Akira Iwasaki [1,3], Hidetosi Saitoh [4], Shigenobu Kimura [1,5], Morio Seino [1,6], Fumio Komai [1,7]

[1)] *Hirosaki University Graduate School of Health Sciences, Aomori 036-8564, Japan*
[2)] *Department of Radiology, Misawa City Hospital, Aomori, 033-0001, Japan*
[3)] *Hirosaki University, School of Health Sciences, Aomori, 036-8564, Japan*
[4)] *Tokyo Metropolitan University Graduate School of Health Sciences, Tokyo, 116-8551, Japan*
[5)] *Department of Radiology, Aomori City Hospital, Aomori, 030-0821, Japan*
[6)] *Department of Radiology, Hirosaki University Hospital, Aomori, 036-8563, Japan*
[7)] *Department of Radiology, Aomori Prefectural Hospital, Aomori, 030-8553, Japan*
e-mail: beamon@r20.7-dj.com (M. Sasamori)

Abstract

The convolution method is one of the methods that can calculate 3D high-energy x-ray doses in media. This method is to convolve the primary x-ray strength (terma or collision kerma) with a dose kernel. The x-ray spectrum as a function of the off-axis distance varies depending on the linear accelerator. Moreover, the x-ray spectrum varies along each rayline in media. The present study was to develop a new method for obtaining dose kernels based on the x-ray spectrum using a Monte Carlo (MC) simulation. The dose kernel was separated into primary and scatter dose components, and the primary water collision kerma was used as the primary x-ray intensity. For a linear accelerator, the x-ray spectrum was reconstructed as a function of the off-axis distance. The dose kernels used in the commercial radiation treatment planning (RTP) systems have been simulated using an infinite water phantom; however, it has been found that this idea is not reasonable. Simulating dose kernels using a semi-infinite water phantom is rather reasonable. The present study describes (1) how the dose kernel based on a semi-infinite water phantom is different from that based on an infinite water phantom and (2) how to simulate dose kernels using information of measured x-ray spectra.

1. Introduction

In high-energy x-ray therapy, radiation treatment planning (RTP) systems are used for 3D dose calculations in media. The convolution (or superposition) method [1-6] is able to calculate primary and scatter dose components separately and is convenient for 3-D dose calculations, especially when using irregular fields with a non-uniform incident beam intensity. Some types of convolution algorithms are adopted in the commercial RTP systems. However, it is found that these convolution algorithms cannot, in general, perform accurate dose calculations in the tumor boundary regions under lung irradiation when the radiation field is small. Although the dose calculation principle of the convolution method is simple, the degree of the dose calculation accuracy largely depends on such inputted data as the incident primary x-ray intensity distribution, the incident x-ray spectrum variation as a function of the off-axis distance, the x-ray spectrum variation along each rayline in media, and the dose kernel. When using the convolution algorithms in the commercial RTP systems, we should point out the following terms:

(1) Use of dose kernels constructed in an infinite water phantom

Iwasaki [7] has reported that dose kernels should be constructed using semi-infinite water phantoms (Fig. 1), not using an infinite water phantom. According to this report, the forward dose kernel should be constructed using a semi-infinite water phantom as shown in Fig. 1(a), setting the photon interaction point *O* at the photon incidence surface. The backward dose kernel should be constructed using semi-infinite phantoms as shown in Fig. 1(b), changing the depth of the photon interaction point *O*. Therefore, it can be seen that since the dose kernels simulated using an infinite water phantom have full quantitative backscatter, the dose calculation based on such dose kernels makes higher doses near the beam incident surface and near the tumor boundary in lung.

(2) Use of dose kernels not based on directly measured x-ray spectra

In general, the x-ray spectrum varies depending on a linear accelerator. Moreover, the spectrum for each linear accelerator varies with the off-axis distance. Therefore, for high-accurate dose calculations, dose kernels should be constructed by taking into account the x-ray spectrum information for each linear accelerator.

(3) Use of terma

The primary x-ray beam suffers the radiation quality change along raylines in media. When using the primary terma (total energy released per unit mass) as the primary x-ray intensity, the ratio of the calculated primary and scatter doses in media turns out to keep constant along each rayline for a given x-ray beam. On the other hand, when using the collision kerma (kinetic energy released per unit mass) as the primary x-ray intensity, more accurate primary dose calculations can be performed because the primary collision kerma itself can be evaluated accurately by taking into account the radiation quality change along each rayline when the information of the x-ray spectra is known. Therefore, the use of dose kernels acting under the primary collision kerma is more reasonable. This fact has also been pointed out by Ahnesjö and Aspradakis [8].

This paper describes a method for constructing new types of dose kernels to act under the collision kerma using a Monte Carlo simulation, separating each of them into primary and scatter dose components.

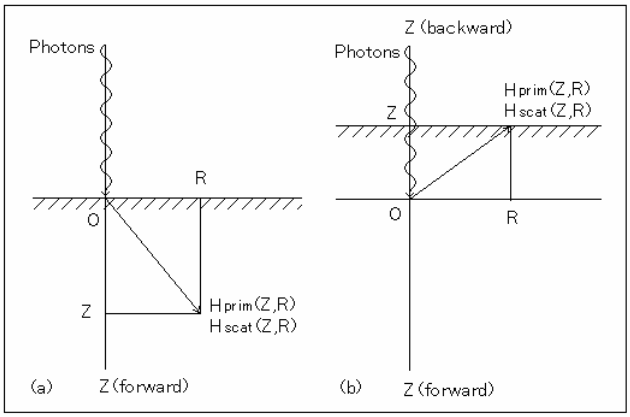

Fig. 1. Diagrams showing how (a) the forward dose kernels and (b) the backward dose kernels should be constructed using semi-infinite water phantoms, where the photon interaction point is situated at point *O*.

2. Materials and Methods

2.1 Theory

2.1.1. Collision kerma

For an x-ray beam having a spectrum with energy bins of i=1, 2, 3,…, n, let $E(i)$ and $\Phi(i)$ denote the representative photon energy (MeV) and photon fluence (photons/cm^2), respectively, of the i-th energy bin. Then the water collision kerma (Gy) for the beam can be expressed as

$$K_{col} = 1.602 \times 10^{-10} \times \sum_{i=1}^{n} E(i) \cdot \mathbf{\Phi}(i) \cdot (\mu_{en}(i)/\rho)_{water} \quad \text{(Gy)}, \tag{1}$$

where $(\mu_{en}(i)/\rho)_{water}$ is the mass energy absorption coefficient (cm^2/g) of water for a photon energy (MeV) of $E(i)$.

2.1.2. Dose calculations using a convolution method

The convolution method developed by Iwasaki [5,6] can also perform 3D dose calculations in heterogeneity media using a photon beam emanating from the source. However, we simply restrict it to the case of calculations in water using a parallel photon beam. We set a dose calculation point (*P*) at the origin of *Z* and *R* coordinates in a water phantom (Fig. 2). When a volume element (ΔV in cm^3) at (*Z*, *R*) is irradiated by x-ray photons with a primary water collision kerma (Gy) of $K_{col}(Z, R)$, the primary and scatter doses (Gy) at point *P* can be expressed as

$$\Delta D_{prim}(Z,R) = H_{prim}(Z,R) \cdot K_{col}(Z,R) \cdot \Delta V \text{ (Gy)}, \tag{2}$$

$$\Delta D_{scat}(Z,R) = H_{scat}(Z,R) \cdot K_{col}(Z,R) \cdot \Delta V \quad \text{(Gy)}, \tag{3}$$

where $H_{prim}(Z,R)$ and $H_{scat}(Z,R)$ express the primary and scatter doses (Gy) at point *P*, respectively, arising from point (*Z*,*R*) per unit volume (cm^3) per unit primary water collision kerma (Gy) at point (*Z*,*R*); therefore, their units are cm^{-3}. Using the total dose kernel

$$H_{total}(Z,R) = H_{prim}(Z,R) + H_{scat}(Z,R) \quad (cm^{-3}), \tag{4}$$

the total dose that is the sum of the primary and scatter doses can be calculated as

$$\Delta D_{total}(Z,R) = H_{total}(Z,R) \cdot K_{col}(Z,R) \cdot \Delta V \quad \text{(Gy)}. \tag{5}$$

Figure 3 illustrates how the $H_{prim}(Z,R)$ and $H_{scat}(Z,R)$ kernels (cm^{-3}) are derived using another set of *Z* and *R* coordinates. They express the primary and scatter doses (Gy) at point *P*, respectively, arising from the photon interaction point *O* per unit volume (cm^3) per unit primary water collision kerma (Gy) at point *O*.

2.1.3. Dose calculations using dose kernels based on MC simulation

Using a Monte Carlo (MC) simulation method on referring to Fig. 3, let $H_{prim}^{MC}(Z,R;E(i))$ and $H_{scat}^{MC}(Z,R;E(i))$ (Gy/photon-interaction) denote the average primary and scatter doses (Gy) at point (*Z*,*R*), respectively, when a photon with a representative energy (MeV) of $E(i)$ interacts with water at point *O*. On the other hand, let $\Phi(i)$ be the photon fluence (photons/cm^2) at point *O* regarding the *i*-th energy bin. Then the number of photons performing interactions (Rayleigh scattering, photoelectric effect, Compton scattering, electron pair production) with a water volume element (cm^3) of ΔV at point *O* can be calculated as

$$\Delta N(i)_{photon} = \mathbf{\Phi}(i) \cdot \mu(i)_{water} \cdot \Delta V \quad \text{(photon interactions)}, \tag{6}$$

where $\mu(i)_{water}$ is the linear attenuation coefficient (cm^{-1}) of water for photon energy $E(i)$. Therefore, the primary and scatter doses (Gy) at point (*Z*,*R*) from the water volume element (ΔV) can be expressed as

$$\Delta D_{prim}(Z,R) = \sum_{i=1}^{n} H_{prim}^{MC}(Z,R;E(i)) \cdot [\mathbf{\Phi}(i) \cdot \mu(i)_{water} \cdot \Delta V] \quad \text{(Gy)}, \tag{7}$$

$$\Delta D_{scat}(Z,R) = \sum_{i=1}^{n} H_{scat}^{MC}(Z,R;E(i)) \cdot [\mathbf{\Phi}(i) \cdot \mu(i)_{water} \cdot \Delta V] \quad \text{(Gy)}. \tag{8}$$

Using the total dose kernel

$$H_{total}^{MC}(Z,R;E(i)) = H_{prim}^{MC}(Z,R;E(i)) + H_{scat}^{MC}(Z,R;E(i)) \quad \text{(Gy/photon-interaction)}, \tag{9}$$

the total dose (Gy) can be calculated as

$$\Delta D_{total}(Z,R) = \sum_{i=1}^{n} H_{total}^{MC}(Z,R;E(i)) \cdot [\mathbf{\Phi}(i) \cdot \mu(i)_{water} \cdot \Delta V] \quad \text{(Gy)}. \tag{10}$$

2.1.4. Conversion of the MC-based dose kernels to the dose kernels in the convolution method

We describe how the dose kernels used in the convolution method are reproduced using the MC-based dose kernels. For a given x-ray beam, we use a normalized set of water collision kermas ($K_{col}(i)$, i=1-n) that has no unit (or Gy/Gy); namely,

$$\sum_{i=1}^{n} K_{\mathrm{col}}(i) = 1 \quad \text{(no unit)}. \tag{11}$$

Similarly, we use a normalized set of photon fluences ($\Phi_0(i)$, i=1-n) as

$$\sum_{i=1}^{n} \Phi_0(i) = 1 \quad \text{(no unit)}. \tag{12}$$

Let the photon fluences ($\Phi(i)$, i=1-n) generating the normalized set of water collision kermas be expressed as

$$\Phi(i) = f \cdot \Phi_0(i) \quad \text{(photons/cm}^2\text{/Gy)}. \tag{13}$$

Therefore, we obtain

$$K_{col}(i) = f \cdot E(i) \cdot \Phi_0(i) \cdot (\mu_{en}(i)/\rho)_{water} \times 1.602 \times 10^{-10} \quad \text{(no unit)}, \tag{14}$$

$$f = \frac{1}{1.602 \times 10^{-10} \times \sum_{i=1}^{n} E(i) \cdot \Phi_0(i) \cdot (\mu_{en}(i)/\rho)_{water}} \quad \text{(photons/cm}^2\text{/Gy)}. \tag{15}$$

Furthermore, we introduce a special factor for each energy bin (i) as

$$K_0(i) = E(i) \cdot (\mu_{en}(i)/\rho)_{water} / \mu(i)_{water} \times 1.602 \times 10^{-10} \quad \text{(Gy·cm}^3\text{)}. \tag{16}$$

Therefore, we finally have the following expression:

$$H_{\mathrm{total}}(Z,R) = \sum_{i=1}^{n} H_{\mathrm{total}}^{\mathrm{MC}}(Z,R;E(i)) \frac{K_{\mathrm{col}}(i)}{K_0(i)} \quad \text{(cm}^{-3}\text{)}. \tag{17}$$

For $H_{\mathrm{prim}}(Z,R)$ and $H_{\mathrm{scat}}(Z,R)$, we similarly have

$$H_{\mathrm{prim}}(Z,R) = \sum_{i=1}^{n} H_{\mathrm{prim}}^{\mathrm{MC}}(Z,R;E(i)) \frac{K_{\mathrm{col}}(i)}{K_0(i)} \quad \text{(cm}^{-3}\text{)}, \tag{18}$$

$$H_{\mathrm{scat}}(Z,R) = \sum_{i=1}^{n} H_{\mathrm{scat}}^{\mathrm{MC}}(Z,R;E(i)) \frac{K_{\mathrm{col}}(i)}{K_0(i)} \quad \text{(cm}^{-3}\text{)}. \tag{19}$$

2.1.5. Verification of the MC-based dose kernels

We use MC-based primary and scatter dose kernels (Gy/photon-interaction) produced using photons with energy E (MeV), where in Fig. 4, we simulate that the photon interactions occur at the origin O of the Z and R coordinates using an infinite water phantom.

First we give an account of the primary dose kernel. The average primary dose energy (J) deposited in the infinite water phantom caused by one photon interaction can be calculated as

$$W_{prim} = E \cdot (\mu_{en}(E)/\rho)_{water} / \mu(E)_{water} \times 1.602 \times 10^{-13} \quad \text{(J)}, \tag{20}$$

where $(\mu_{en}(E)/\rho)_{water}$ and $\mu(E)_{water}$ are, respectively, the mass energy absorption coefficient (cm^2/g) and linear attenuation coefficient (cm^{-1}) of water for photon energy E (MeV). On the other hand, the integral dose (J) due to the MC-based primary dose kernel can be calculated as

$$W_{prim}^{MC} = \left[\sum_{i,j} H_{prim}^{MC}(Z_i,R_j) \cdot \Delta Z \cdot \Delta S_j \times 10^{-3}\right]_{\mathrm{forward}} + \left[\sum_{i,j} H_{prim}^{MC}(Z_i,R_j) \cdot \Delta Z \cdot \Delta S_j \times 10^{-3}\right]_{\mathrm{backward}} \quad \text{(J)} \tag{21}$$

with

$$\Delta S_j = \pi[(R_j + \Delta R/2)^2 - (R_j - \Delta R/2)^2] \quad \text{(cm}^2\text{)},$$

where (Z_i, R_j) shows the coordinates (cm) of the mid point of matrix (i,j) with intervals (cm) of ΔZ and ΔR. Both values for W_{prim} and W_{prim}^{MC} should agree with each other.

Secondly, we give an account of the scatter dose kernel. The average scatter dose energy (J) deposited in the infinite water phantom caused by one photon interaction can be calculated as

$$W_{scat} = E \cdot ((\mu(E)/\rho)_{water} - (\mu_{en}(E)/\rho)_{water}) / \mu(E)_{water} \times 1.602 \times 10^{-13} \quad \text{(J)}, \tag{22}$$

where $(\mu(E)/\rho)_{water}$ is the mass attenuation coefficient (cm^2/g) of water for photon energy E (MeV). On the other hand, the integral dose (J) due to the MC-based scatter dose kernel can be calculated as

$$W_{scat}^{MC} = \left[\sum_{i,j} H_{scat}^{MC}(Z_i, R_j)\cdot\Delta Z\cdot\Delta S_j\times 10^{-3}\right]_{\text{forward}} + \left[\sum_{i,j} H_{scat}^{MC}(Z_i, R_j)\cdot\Delta Z\cdot\Delta S_j\times 10^{-3}\right]_{\text{backward}} \quad \text{(J)}. \qquad (23)$$

Both values for W_{scat} and W_{scat}^{MC} should agree with each other.

Lastly, we give an account of the total dose kernel. The average total dose energy (J) deposited in the infinite water phantom caused by one photon interaction can be calculated as

$$W_{total} = E\cdot(\mu(E)/\rho)_{water} / \mu(E)_{water} \times 1.602\times 10^{-13} = W_{prim} + W_{scat} \quad \text{(J)}. \qquad (24)$$

On the other hand, the integral dose (J) due to the MC-based total dose kernel can be calculated as

$$W_{total}^{MC} = \left[\sum_{i,j} H_{total}^{MC}(Z_i, R_j)\cdot\Delta Z\cdot\Delta S_j\times 10^{-3}\right]_{\text{forward}} + \left[\sum_{i,j} H_{total}^{MC}(Z_i, R_j)\cdot\Delta Z\cdot\Delta S_j\times 10^{-3}\right]_{\text{backward}} \quad \text{(J)}, \qquad (25)$$

Both values of W_{total} and W_{total}^{MC} should agree with each other.

2.2 Monte Carlo simulation

The primary dose component in the dose kernels is the dose imparted to water due to the ionization and excitation generated along the tracks of the secondary electrons (Auger electrons, photon electrons, Compton electrons, and pair production electrons) generated by the photon interaction at the kernel origin (*O*) (see Fig. 3 or 4) and along the tracks of their δ rays. The scatter dose component in the dose kernels is the dose imparted to water due to Rayleigh scattering photons, annihilation gamma-rays, Compton scattering photons, characteristic x-rays, and bremsstrahlung that are caused after the photon interaction.

The EGS4 MC code was used for constructing 4 and 10 MV x-ray dose kernels. Input data were obtained using 4 and 10 MV x-ray beams from a linear accelerator (Varian Clinac 21EX). For each beam, sets of photon fluences as a function of the off-axis distance, composed of about 10 energy bins, were estimated [9-11] using acrylic and lead transmission data. We developed a new user code to obtain the primary and the scatter dose kernel separately, simulating that monochromatic photons of each energy bin of the x-ray spectrum impinge upon a certain point in an infinite or a semi-infinite water phantom.

The separation of the primary and the scatter dose was performed using Subroutine AUSGAB. When a photon enters into water and interact with water at a point, we placed a flag on each of the scatter photons generated directly by the photon interaction at the point. Letting the dose caused by the flagged scatter photons be the scatter dose, the primary dose was calculated by substituting the scatter dose from the total dose. Table 1 lists input parameters used for the MC simulation.

2.3 X-ray spectra and others

Figure 5 shows (a) 4 MV and (b) 10 MV x-ray spectra in relative photon fluences (Φ_0) as a function of the off-axis distance. These spectra were reconstructed for the present linear accelerator using an iterative method developed by Iwasaki et al [9-11]. Verification of the MC-based dose kernels was performed using Eqs. (20), (22), and (24) with data on $\mu(E)_{water}$, $(\mu(E)/\rho)_{water}$, and $(\mu_{en}(E)/\rho)_{water}$ published by Hubbell [12].

Table 1. Input parameters of the MC simulation.

AE and ECUT	0.521 MeV
AP and PCUT	0.01 MeV
Number of incident particle	1×10^7

AE: Array containing PEGS lower charged particle cutoff energy for each medium. ECUT: Array of regions' charged cutoff energies. AP: Array containing PEGS lower photon cutoff energy for each medium. PCUT: Array of regions' photon cut off energies.

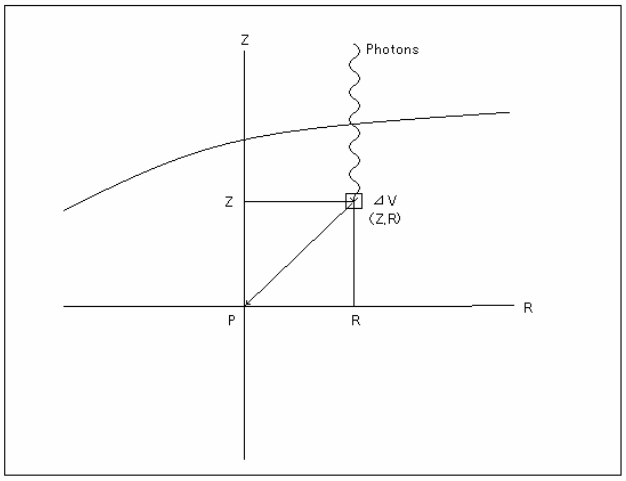

Fig. 2. Diagram showing how to calculate the dose at point P in a water phantom, arising from a volume element ΔV at point (Z,R) using a parallel photon beam.

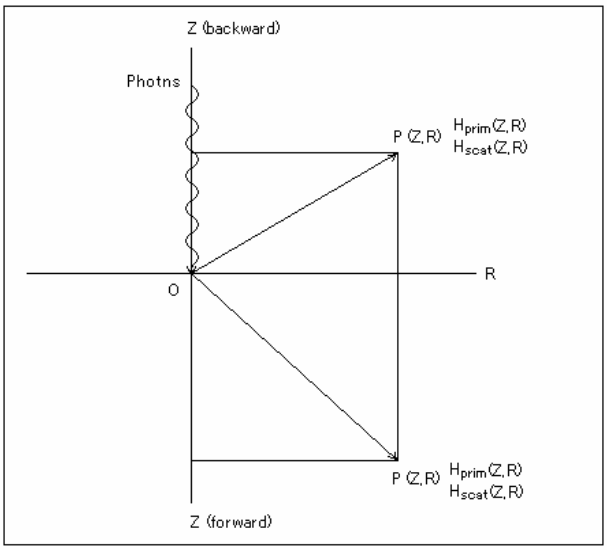

Fig. 3. Diagram illustrating how the $H_{prim}(Z,R)$ and $H_{scat}(Z,R)$ kernels are derived, expressing the primary and scatter doses at point $P(Z,R)$, respectively, arising from the photon interaction point O.

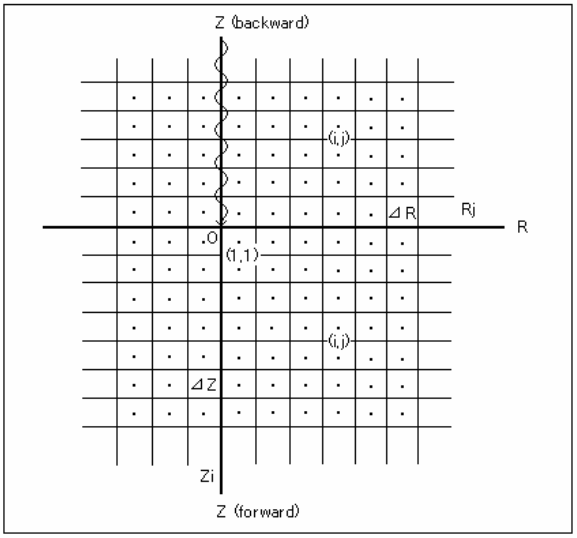

Fig. 4. Diagram showing how the primary or scatter dose is contributed to matrix element (i,j), arising from the photon interaction point O, where the primary or scatter dose is averaged within the ring made by rotating each matrix element (i,j) around the Z axis.

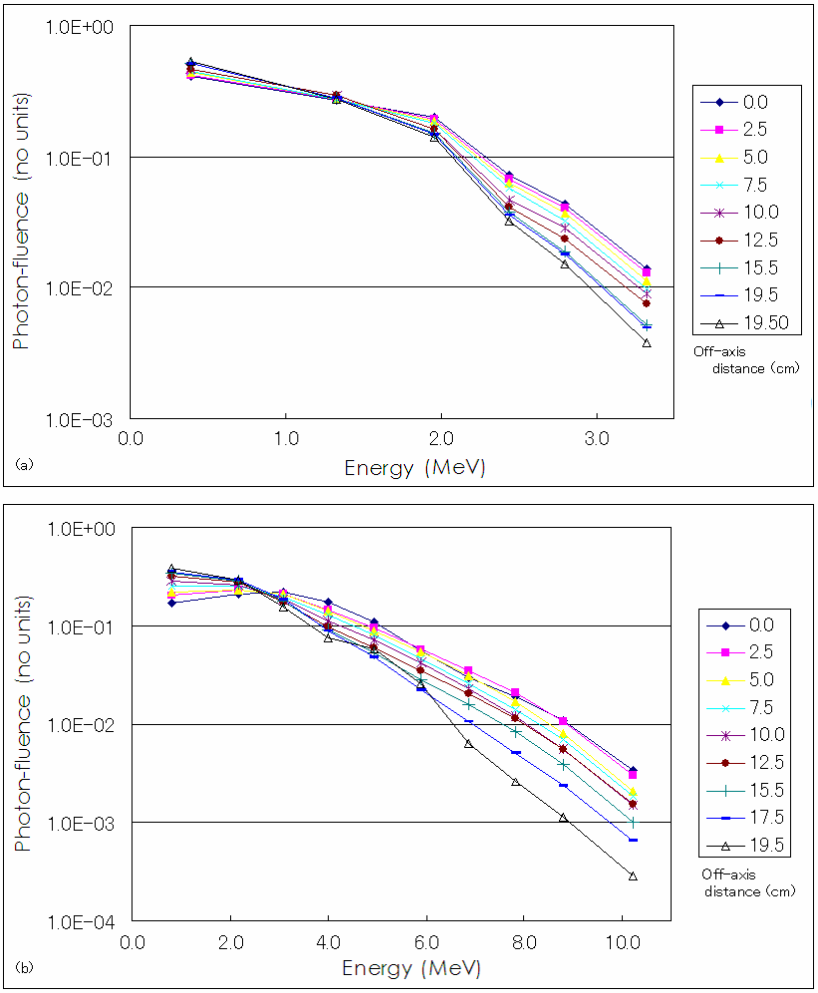

Fig. 5. (a) 4 MV and (b) 10 MV x-ray spectra in relative photon fluences (Φ_0) as a function of the off-axis distance.

3. Results and discussion

Figure 6 shows how the integral primary, scatter, and total doses (J) due to one photon interaction vary with the photon energy (0.1-10 MeV). The lines were obtained by the analytical method using Eqs. (20), (22), and (24). The sets of dots were obtained using Eqs. (21), (23), and (25), by integrating each of the MC-based primary, scatter, and total dose kernels that were produced using a large cylindrical water phantom with a radius of 500 cm (ΔR=5 cm) and a height of 500 cm (ΔZ=5 cm), letting the photon interaction point be placed at the center of the phantom. It can be seen that each set of dots coincides well with the corresponding line. Therefore, it can be understood that both MC and analytical methods are reasonable.

Using photon energies of 0.391, 1.330, 1.955, 2.443, 2.794, and 3.320 MeV that are the representative photon energies of the 4 MV x-ray spectra (Fig. 5(a)), we simulated MC-based primary and scatter dose kernels (Gy/photon-interaction) in an infinite water phantom. Figure 7 shows results for the primary dose components, showing that there is a limited dose region for each of the photon energies, that the dose pattern becomes large as the photon energy becomes large, and that although the dose pattern is long and narrow near the photon interaction point, it becomes round as the distance from the photon interaction becomes large. Figure 8 shows results for the scatter dose components, showing that there is no limited dose region, that the dose pattern does not change much largely with the photon energy, and that there is a forward scattering effect around the Z axis. It should be noted that the dose pattern in Fig. 8(a) shows an effect due to Rayleigh (coherent) scattering around the Z-axis (Rayleigh scattering has more practical importance at low energies and the scattering angle is usually redirected through only a small angle). Similarly, Figs. 9 and 10 show

results using the 10 MV x-ray spectrum (Fig. 5(b)), having photon energies of 0.812, 2.179, 3.091, 4.002, 4.939, 5.901, 6.863, 7.825, 8.787, and 10.230 MeV. The same dose patterns as in the 4 MV x-ray beam were obtained.

Using Eqs. (17)-(19) with the above-described dose kernels in Figs. 7-10, we reconstructed primary, scatter, and total dose kernels (cm^{-3}) for the whole photon energies in an infinite water phantom. Figure 11 shows results using the 4 MV x-ray spectrum at the central axis. Figure 12 shows results using the 10 MV x-ray spectrum at the central axis. By comparing isodose values in Figs. 11 and 12, it can be understood that for each of the 4 and 10 MV x-ray beams, the primary dose kernel performs a much greater dose contribution.

Figure 13 shows how the MC-based primary dose kernel (cm^{-3}) for 4 MV x-rays at the central axis changes with the matrix size (ΔZ and ΔR) using values of (a) 0.05 cm, (b) 0.02 cm, and (c) 0.005 cm for ΔZ and ΔR. It is observed that the isodose shape near the photon interaction point varies largely according to the matrix size and that the isodose shape with large dose values becomes long and narrow as the matrix size becomes small. Therefore, it can be understood that for accurate dose calculations, the primary dose kernel should be simulated using as small ΔZ and ΔR values as possible; however, it has been found that spiral patterns are yielded in regions when using ΔZ and ΔR values less than 0.02 cm (for the single precision). Regarding the scatter dose kernel, the isodose shape keeps almost the same for these matrix sizes, as shown in Fig. 14. The MC-based primary and scatter dose kernels and others shown in Figs. 6-12 were all constructed using $\Delta Z=\Delta R=0.02$ cm.

Changing the photon interaction depth in a semi-infinite water phantom, we simulated the primary and scatter doses (Gy/photon-interaction) at the matrix element of (1,1) in Fig. 4 using $\Delta R=\Delta Z=0.02$ cm for (a) 4 MV x-rays and (b) 10 MV x-rays at the central axis. Figure 15 shows results in relative dose values, letting each of the primary and scatter doses be unity at large depths. It can be seen that both primary and scatter dose components become almost constant beyond at depths greater than 0.3 cm for 4 MV x-rays and at depths greater than 0.5 cm for 10 MV x-rays. It can be understood that the dose kernel produced based on semi-infinite water phantoms is much different from that produced based on an infinite water phantom, especially around the photon interaction point. Accordingly, it should be noted that the convolution method happens to calculate large different dose values depending on whether the dose kernel is based on semi-infinite water phantoms or based on infinite water phantoms.

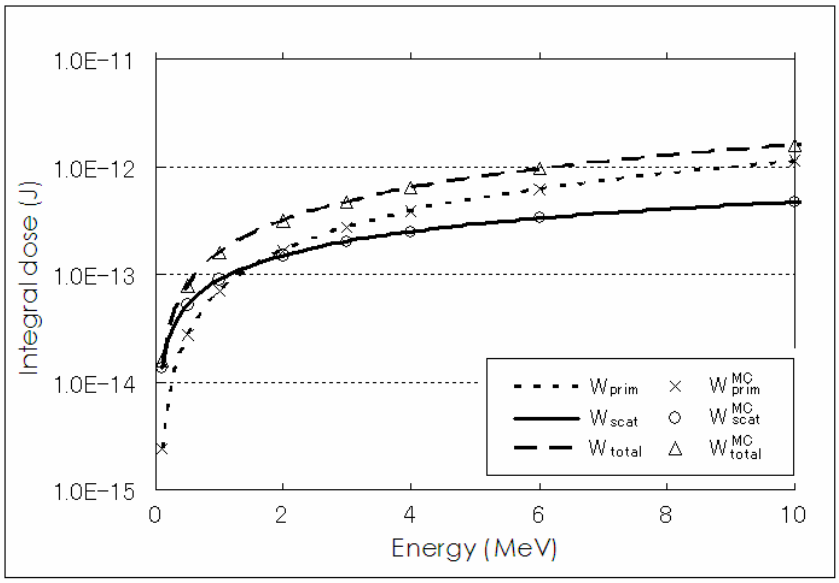

Fig. 6. Integral primary, scatter, and total doses (J) for one photon interaction at the center point of a large water phantom. The lines were obtained by the analytical method using Eqs. (20), (22), and (24). The sets of dots were obtained by integrating each of the MC-based primary, scatter, and total dose kernels for monochromatic photon energies.

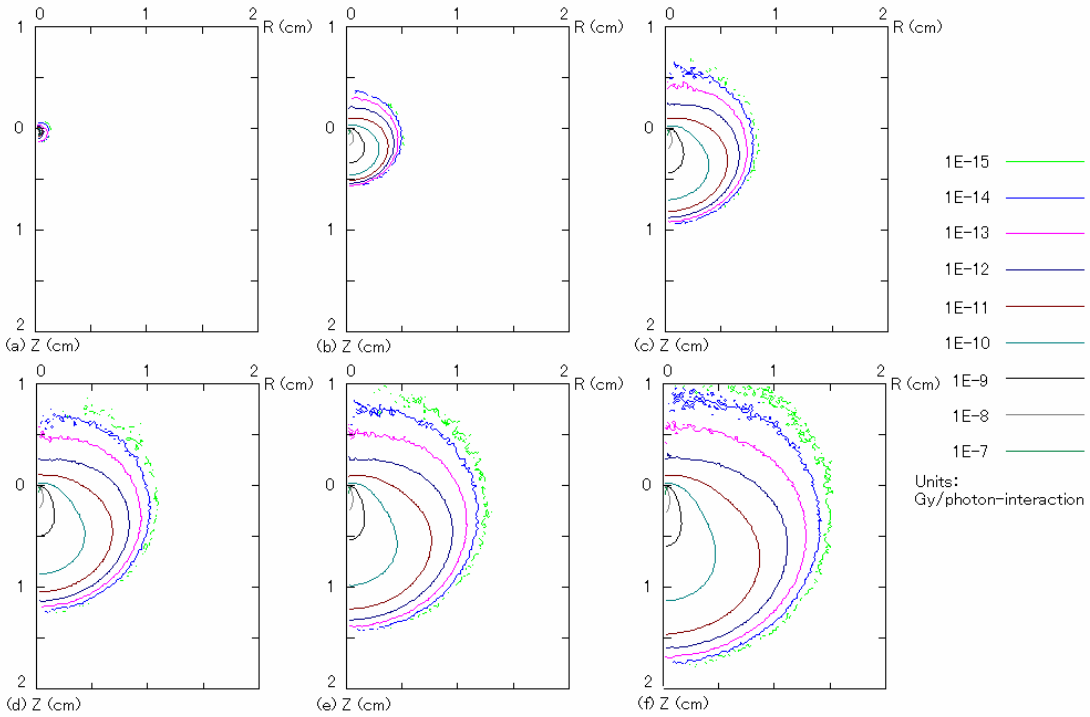

Fig. 7. Primary dose kernels (Gy/photon-interaction) simulated in an infinite water phantom using photon energies of (a) 0.391, (b) 1.330, (c) 1.955, (d) 2.443, (e) 2.794, and (f) 3.320 MeV that are the representative photon energies of a 4 MV x-ray spectrum.

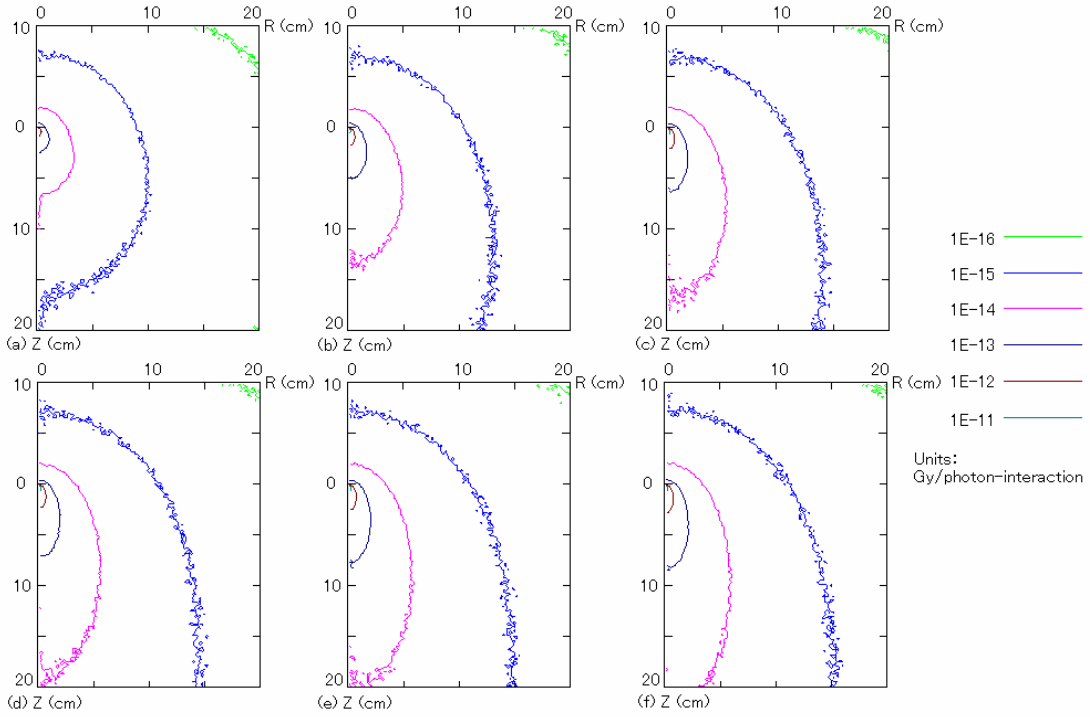

Fig. 8. Scatter dose kernels (Gy/photon-interaction) simulated in an infinite water phantom using photon energies of (a) 0.391, (b) 1.330, (c) 1.955, (d) 2.443, (e) 2.794, and (f) 3.320 MeV that are the representative photon energies of a 4 MV x-ray spectrum.

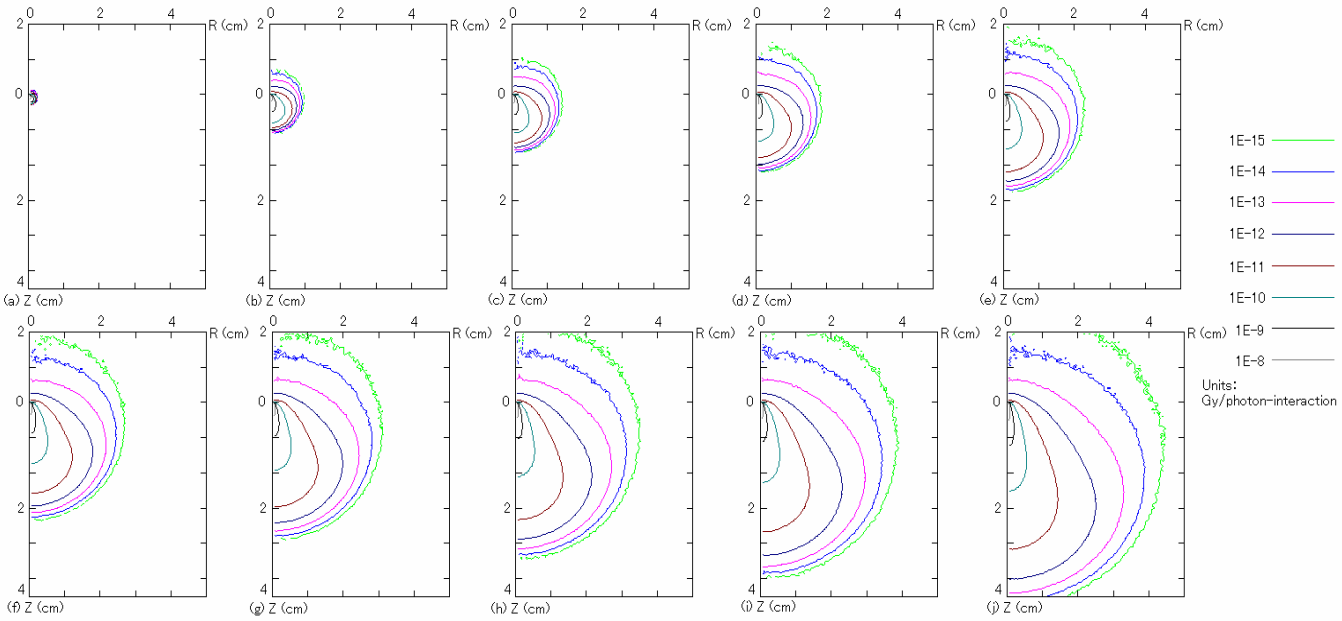

Fig. 9. Primary dose kernels (Gy/photon-interaction) simulated in an infinite water phantom using photon energies of (a) 0.812, (b) 2.179, (c) 3.091, (d) 4.002, (e) 4.939, (f) 5.901, (g) 6.863, (h) 7.825, (i) 8.787, and (j) 10.230 MeV that are the representative photon energies of a 10 MV x-ray spectrum.

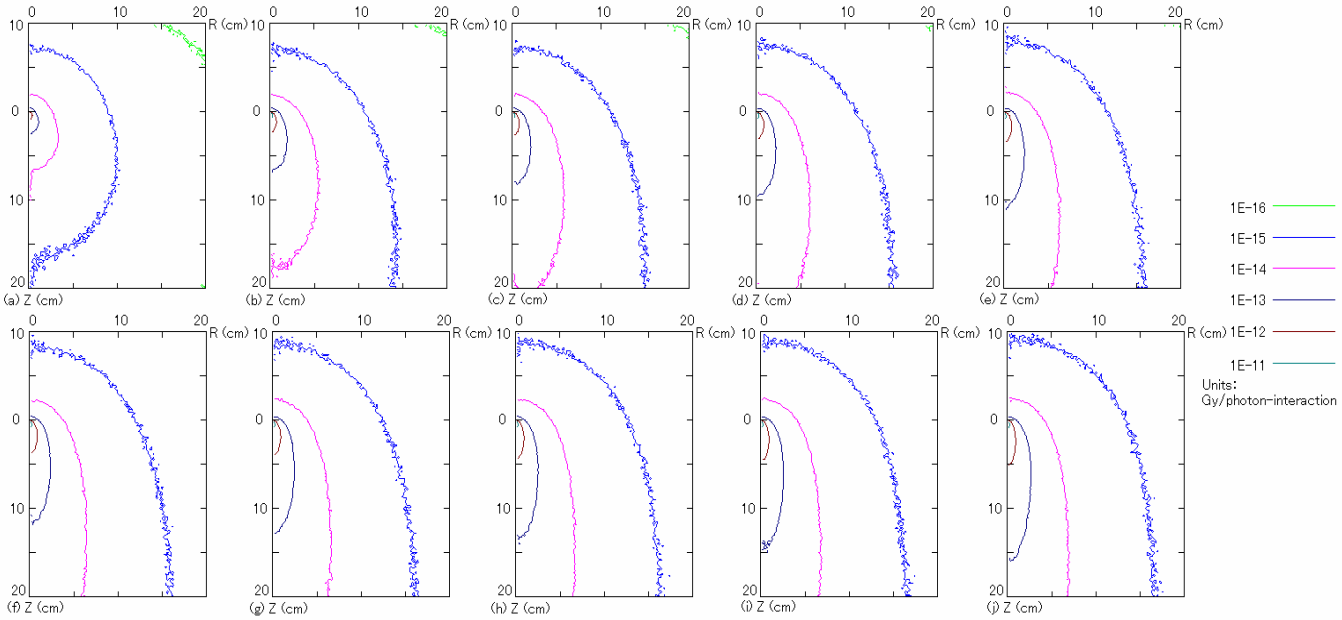

Fig. 10. Scatter dose kernels (Gy/photon-interaction) simulated in an infinite water phantom using photon energies of (a) 0.812, (b) 2.179, (c) 3.091, (d) 4.002, (e) 4.939, (f) 5.901, (g) 6.863, (h) 7.825, (i) 8.787, and (j) 10.230 MeV that are the representative photon energies of a 10 MV x-ray spectrum.

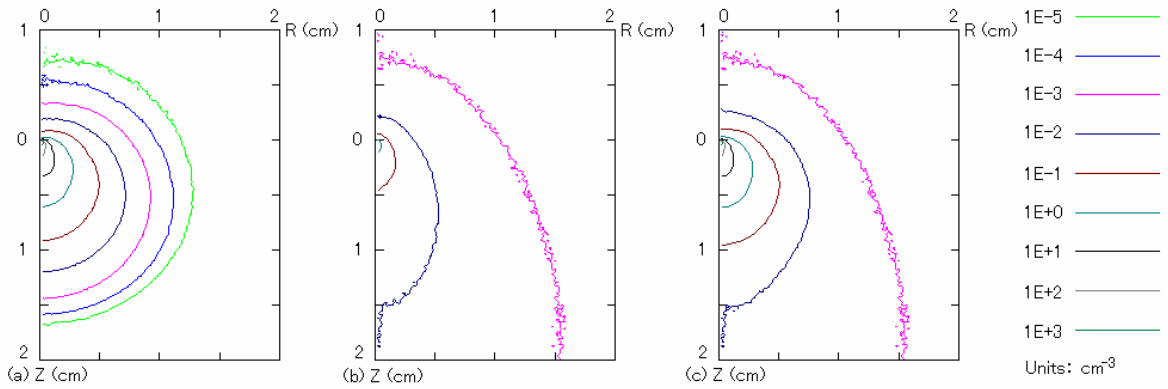

Fig. 11. (a) Primary, (b) scatter, and (c) total dose kernels (cm^{-3}) for 4 MV x-rays, simulated in an infinite water phantom using a measured set of spectrum at the central axis.

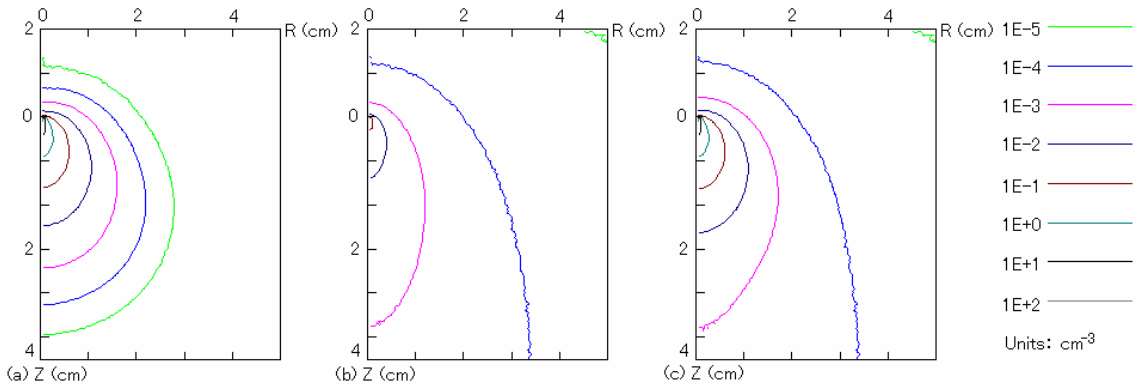

Fig. 12. (a) Primary, (b) scatter, and (c) total dose kernels (cm^{-3}) for 10 MV x-rays, simulated in an infinite water phantom using a measured set of spectrum at the central axis.

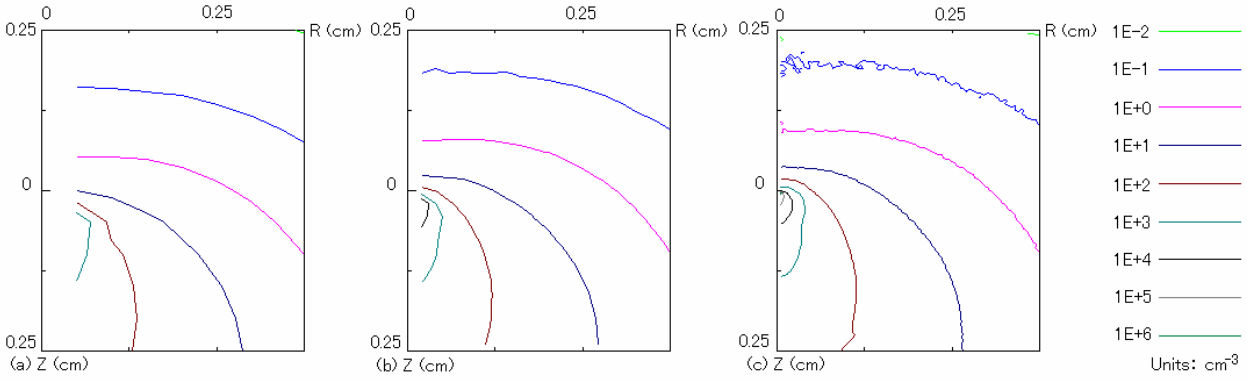

Fig. 13. Diagrams showing how the primary dose kernel (cm^{-3}) for 4 MV x-rays at the central axis changes with the size of the matrix using values of (a) 0.05 cm, (b) 0.02 cm, and (c) 0.005 cm for ΔZ and ΔR.

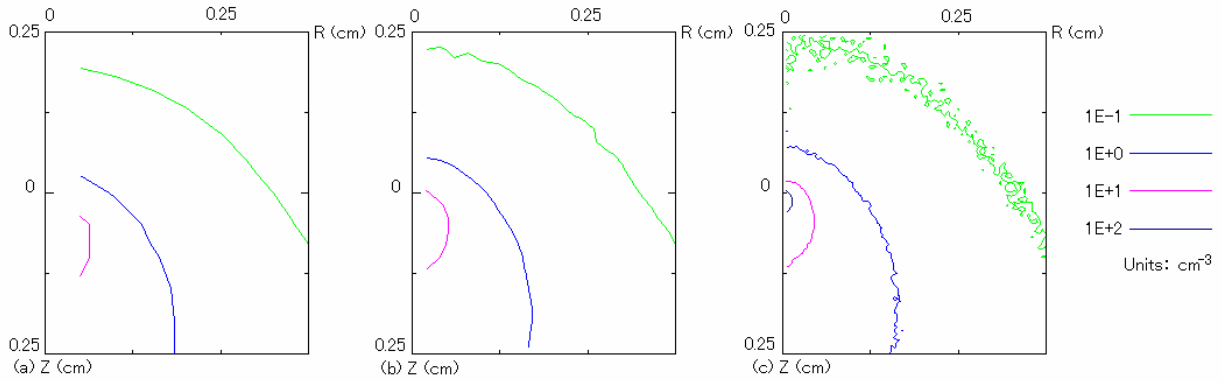

Fig. 14. Diagrams showing how the scatter dose kernel (cm^{-3}) for 4 MV x-rays at the central axis changes with the size of the matrix using values of (a) 0.05 cm, (b) 0.02 cm, and (c) 0.005 cm for ΔZ and ΔR.

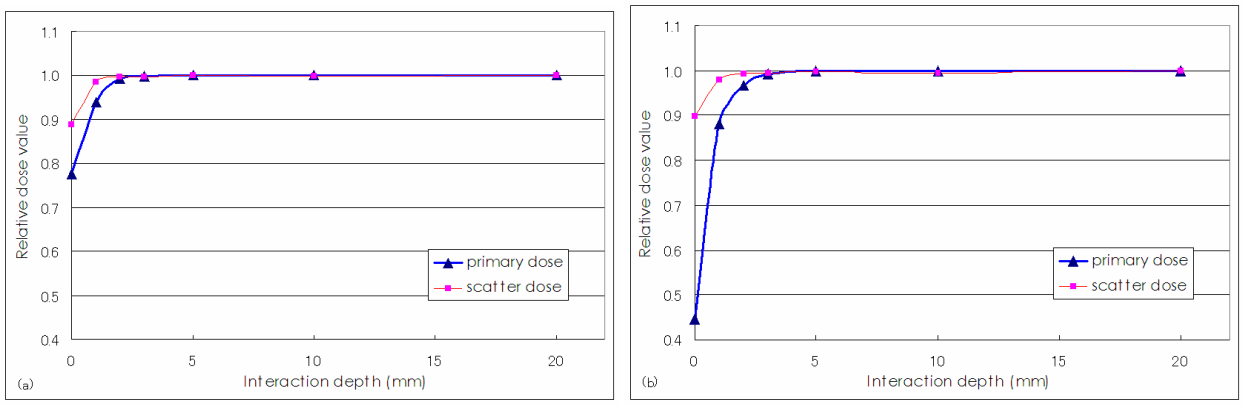

Fig. 15. Diagrams showing how (a) the 4 MV x-ray and (b) the 10 MV x-ray primary and scatter doses in the (1,1) matrix element (Fig. 4) change with the interaction depth in a semi-infinite water phantom.

4. Conclusions

We have developed a Monte Carlo simulation method to obtain primary, scatter, and total dose kernels using information of x-ray spectrum. The experiments were performed using 4 and 10 MV x-ray beams from a linear accelerator. We simulated dose kernels in infinite and semi-infinite water phantoms based on measured x-ray spectra as a function of the off-axis distance. It has been found that the dose kernel produced based on semi-infinite water phantoms is much different from that produced based on an infinite water phantom, especially around the photon interaction point.

References

1) A. L. Boyer and E. C. Mok: A photon dose distribution model employing convolution calculations. Med. Phys. 12: 169-177 (1985).
2) T. R. Mackie, J. W. Scrimger, and J. J. Battista: A convolution method of calculating dose for 15-MV x rays. Med. Phys. 12: 188-196 (1985).
3) R. Mohan, C. Chui, and L. Lidofsky: Differential pencil beam dose computation model for photons. Med. Phys. 13: 64-73 (1986).
4) A. Ahnesjö: Collapsed cone convolution of radiant energy for photon dose calculation in heterogeneous media.

Med. Phys. 16: 577-592 (1989).
5) A. Iwasaki: A convolution method for calculating 10-MV x-ray primary and scatter dose including electron contamination dose. Med. Phys. 19: 907-915 (1992).
6) A. Iwasaki: 10 MV X-ray central-axis dose calculation in thorax-like phantoms (water/cork) using the differential primary and scatter method. Radiat. Phys. Chem. 65: 11-26 (2002).
7) A. Iwasaki: Comments on the primary and scatter dose-spread kernels used for convolution methods. Radiat. Phys. Chem. 65: 595-597 (2002).
8) A. Ahnesjö and M. M. Aspradakis: Dose calculations for external photon beams in radiotherapy. Phys. Med. Biol. 44: 99-155 (1999).
9) A. Iwasaki, H. Matsutani, M. Kubota, A. Fujimori, K. Suzaki and Y. Abe: A practical method for estimating high-energy X-ray spectra using the iterative perturbation principle proposed by Waggener. Radiat. Phys. Chem. 67: 81-89 (2003).
10) A. Iwasaki, M. Kubota, J. Hirota, M. Itoh, A. Fujimori, K. Suzaki, M. Aoki and Y. Abe: Characteristic features of a high-energy x-ray spectra estimation method base on the Waggener iterative perturbation principle (in Japanese). J. Jpn. Soc. Ther. Radiol. Oncol. 17: 79-95 (2005).
11) A. Iwasaki, M. Kubota, J. Hirota, A. Fujimori, K. Suzaki, M. Aoki, and Y. Abe: Characteristic features of a high-energy x-ray spectra estimation method base on the Waggener iterative perturbation principle. Med. Phys. Accepted for publication (2006)
12) J. H. Hubbell: Photon mass attenuation and energy-absorption coefficients from 1 keV to 20 MeV. Int. J. Appl. Radiat. Isot. 33: 1269-1290 (1982).

Analysis of variation in the position of maximum dose in the percentage depth dose with field size using EGS4

M.Yoshikawa, Y.Obata[1], K.Tabushi[1], and Y.Shiota

Department of Radiological Technology, Graduate School of Medicine, Nagoya University
1 – 1 – 20 Daikou – Minami, Higashi area, Nagoya, Japan
[1] Nagoya University School of Health Science
e-mail: j050230m@mbox.nagoya-u.ac.jp

Abstract

The percentage depth dose increases with field size in the buildup region, resulting in a shift of the observed position of maximum dose. The purpose of this work is to examine the component of the radiation generated in the head of a clinical linear accelerator and to investigate the effect of the components on the position of maximum dose using the EGS4 code. The head structure of the clinical linear accelerator was reproduced in the simulation. A phase space file was obtained and the percentage depth dose was calculated from it. It was confirmed that the position of maximum dose in the percentage depth dose was observed at shallower depth as the field size was increased. When the field size was larger, the incident scatter radiation into the field increased. The smaller it was, the lower energy of the scatter radiation was.

1. Introduction

For high energy x-ray beams from the clinical linear accelerator (linac), it is well known that the position of maximum dose in the percentage depth dose (PDD) depends on a field size. The position of maximum dose is observed at gradually shallower depth as the field size is increased [1]. Figure 1 shows measured PDDs of 10 MV x-ray, and the relationship between the field size and the position of maximum dose. If the field size increases, the position of maximum dose becomes shallower. Since PDD is fundamental data for the treatment planning, it is important to know the characteristics of PDD. The main purpose of this study is to examine the cause of changing the position of maximum dose with the field size by Monte Carlo code EGS4 [2].

2. EGS4 simulation

2.1 Phase space file

To obtain the phase space file, we reproduced the head structure of the linac of the 10 MV photon mode in EGS4. Figure 2 shows the constructed head structure and figure 3 shows the geometry to obtain the phase space file. The linac head consists of five main component modules, i.e., a target, a primary collimator, a flattening filter, a monitor chamber and a secondary collimator. The secondary collimator is composed of an upper jaw and a lower jaw.

Scored plane was set at the position of the source surface distance (SSD = 100 cm) to collect the particles after transportation from the linac and to form the so-called phase space file. The information in it included the charge, the energy, the position (X, Y, Z), the direction (U, V, W) and the origin (LATCH) of particles [3]. The irradiation field

sizes were 5 × 5 and 30 × 30 cm^2 at the position of SSD. We used the obtained phase space file for the source of the following simulation and analysed the position of maximum dose in each field size.

The energy of incident electron was 10 MeV. The cut-off energies of photon and electron were 10 keV and 521 keV, respectively.

2.2 Calculation of PDDs

Figure 4 shows the geometry to calculate the PDDs calculated by the obtained phase space file. The water phantom size was 40 × 40 × 40 cm^3 and the phase space file was on the phantom surface. PDDs were calculated up to 25.0 cm depth with 2.0 × 2.0 × 0.1 cm^3 voxel size.

2.3 Analysis of the position of maximum dose in each field size

Ratio of the primary to the scattered radiation in the vicinity of the position of maximum dose and the energy spectra of the scattered radiation on the phantom surface were calculated using LATCH in the phase space file.

3. Results and Discussions

Depth dose curves of (a) 5 × 5 cm^2 field and (b) 30 × 30 cm^2 field are shown in figure 5. Approximative peaks were obtained from each graph. The values of the position of maximum dose were about 2.80 cm in 5 × 5 cm^2 field and about 1.98 cm in 30 × 30 cm^2 field, respectively.

PDDs of each field size are shown in figure 6. The position of maximum dose in 30 × 30 cm^2 field was shallower than that in 5 × 5 cm^2 field.

Figure 7 shows ratio of the primary to the scatter radiation at from 0.0 cm to 3.0 cm depths, which are in the vicinity of the position of maximum dose. The percentage of the scatter radiation in 5 × 5 cm^2 field was larger than that in 30 × 30 cm^2 field. This result shows that the contribution of the scatter radiation is larger as the field size increased.

Figure 8 shows the energy spectra of the scatter radiation on the phantom surface from each head component and the field size. The scatter radiation from the secondary collimator has higher energy than those of others. In 5 × 5 cm^2 field, it was more than that in 30 × 30 cm^2 field. This result shows that if the field size increases, the energy of the scatter radiation becomes lower.

4. Conclusions

It can be made certain that the position of maximum dose becomes shallower as the field size increase by using Monte Carlo simulation code, EGS4.

If the field size is larger, the scatter radiation incident into the field increases. If the field size decreases, the scatter radiation from lower head component with the higher energy increases. Therefore the energy of the scatter radiation in larger field size is lower than that in smaller.

These result shows that the position of maximum dose becomes shallower as the field size increases.

References

1) Peter J., Biggs, and C. Clifton Ling, " Scattered photons as the cause for the observed d_{max} shift with field size in high-energy photon beams " , Med. Phys. 4, 310-314 (1977).
2) R. Nelson, H. Hirayama, and D. W. O. Rogers, " The EGS4 Code System ", SLAC-265 (Stanford Linear Accelerator Center, Stanford, CA, 1985).
3) Sung-Yen Lin, Tieh-Chi Chu, and Jao-Perng Lin, " Monte Carlo simulation of a clinical linear accelerator ", Applied Radiation and Isotopes 55, 759-765 (2001).

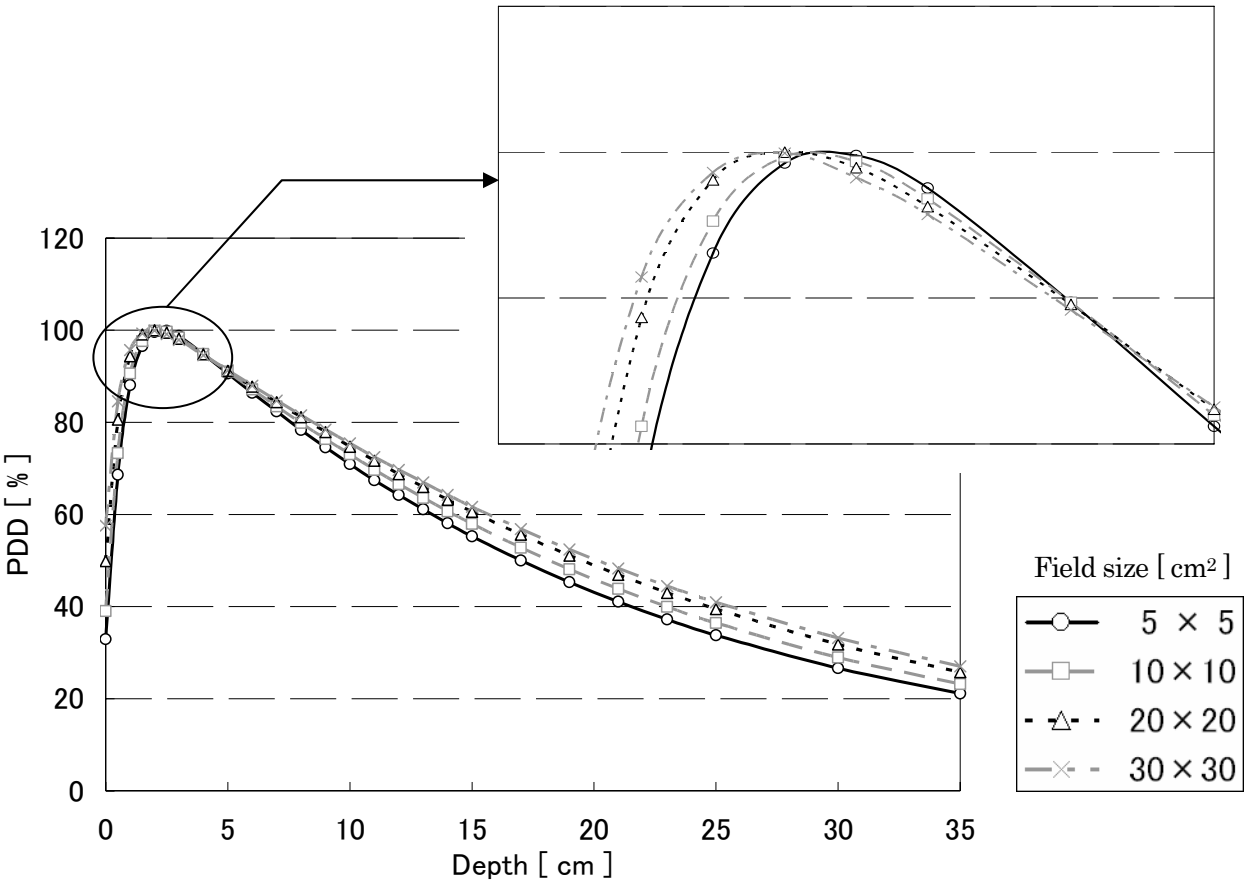

Figure 1. Measured PDDs of 10 MV x-ray.

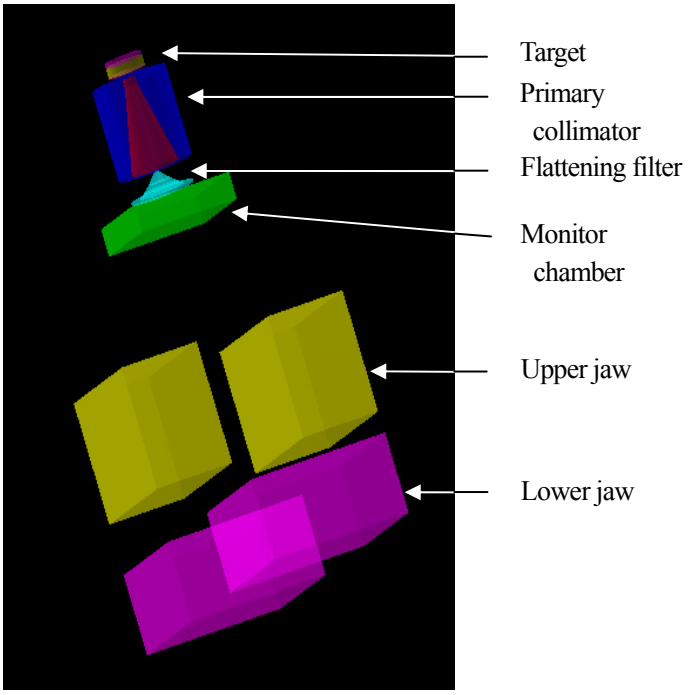

Figure 2. Constructed linac head structure.

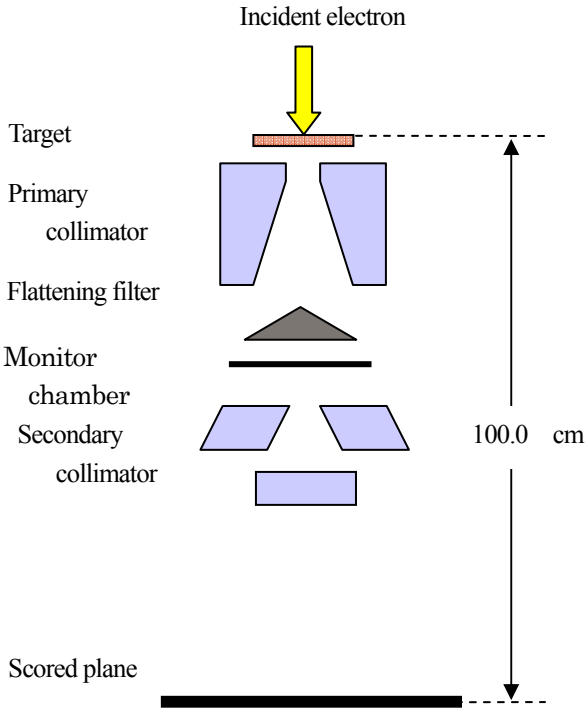

Figure 3. Geometry of a linac head.

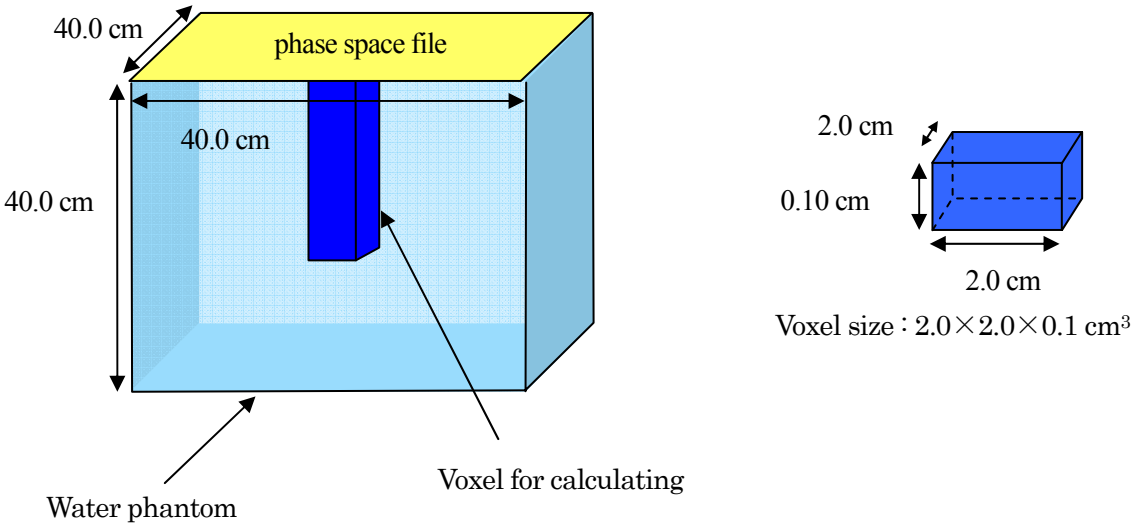

Figure 4. Geometry to calculate PDD and voxel size

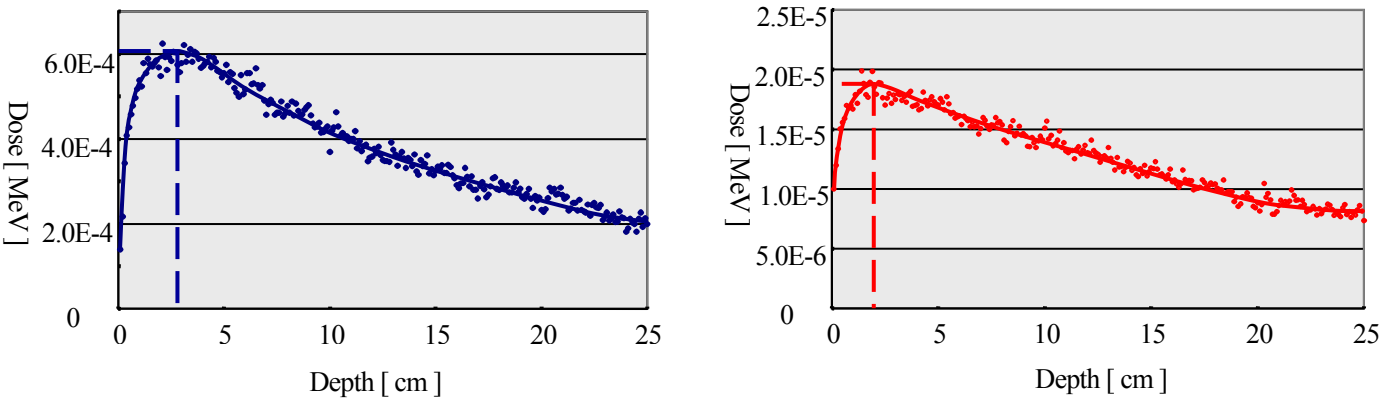

(a) Field size is 5 × 5 cm²

(b) Field size is 30 × 30 cm²

Figure 5. Depth dose curves of (a) 5 × 5 cm² field and (b) 30 × 30 cm² field. The values of the position of maximum dose were about 2.80 cm in 5 × 5 cm² field and about 1.98 cm in 30 × 30 cm² field, respectively.

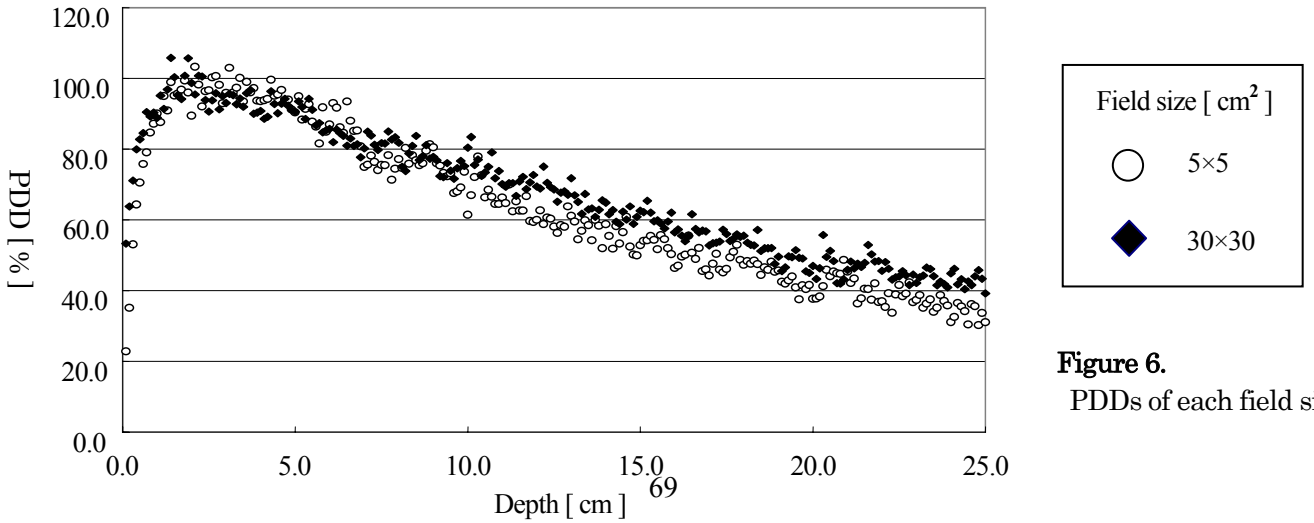

Figure 6.
PDDs of each field size

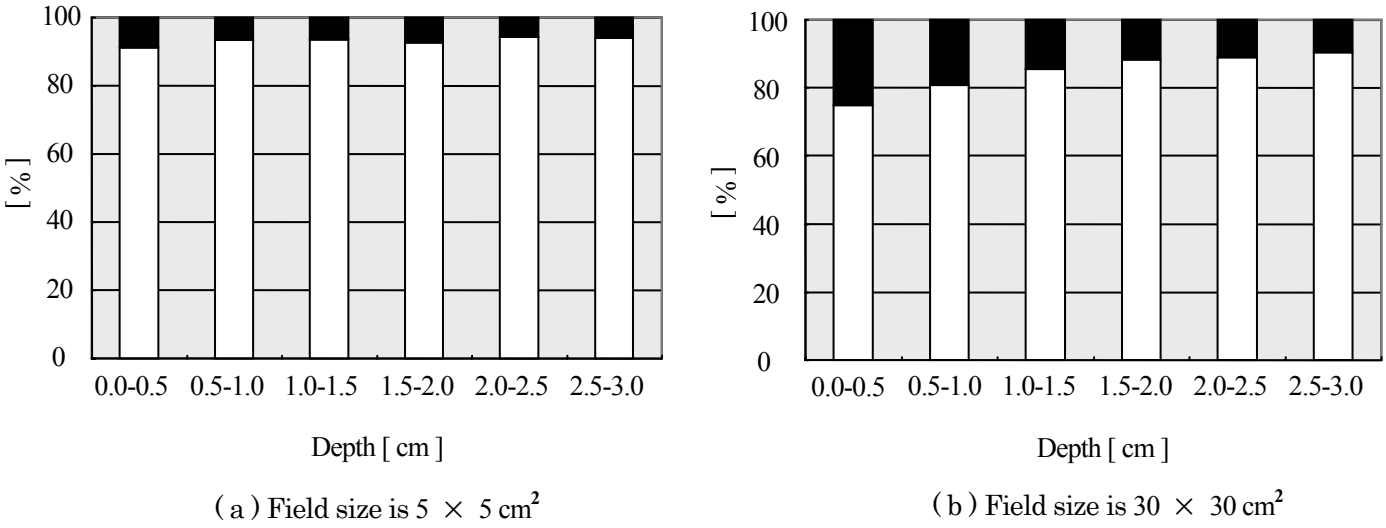

Figure 7. Ratio of the primary to the scatter radiation at each depth that is from 0.0 cm to 3.0 cm depths, which are in the vicinity of the position of maximum dose. □ is the primary radiation, and ■ is the scatter radiation.

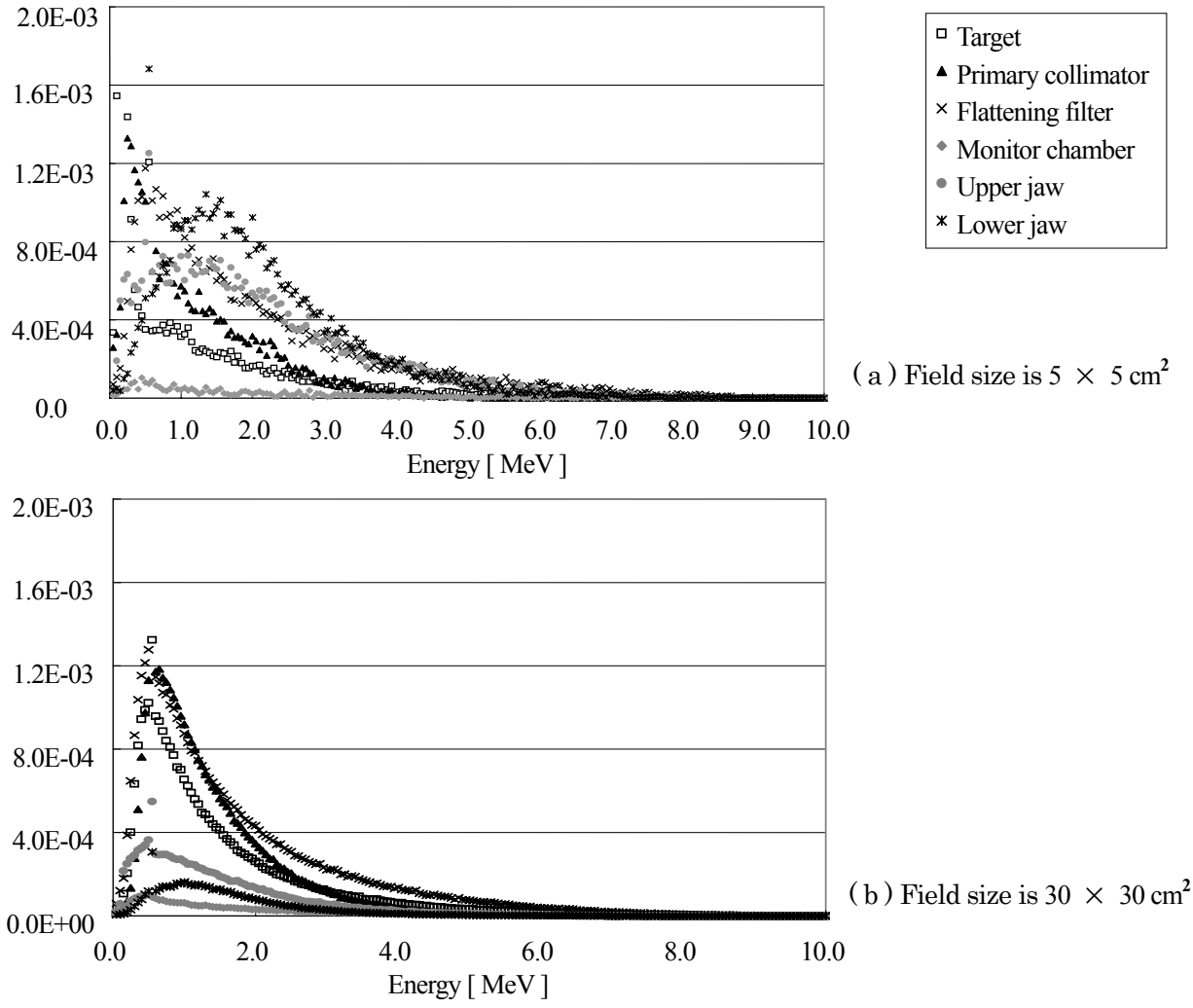

Figure 8. The energy spectra of the scatter radiations on the phantom surface from each head component and the field size.

FUNDAMENTAL EXAMINATION OF FILM DOSIMETRY IN RADIOTHERAPY

C. Nejigaki[1], K. Tabushi[2], T. Shimosato[1,3], Y. Aoyama[1,4], Y. Shiota[1], and N. Kadoya[1]

[1]Department of Radiological Technology, Graduate School of Medicine, Nagoya University
1-1-20 Daikou – Minami, Higashi area, Nagoya, Japan
[2]Nagoya University School of Health Science
[3]Department of Radiology, Hamamatsu University School of Medicine
[4]Department of Radiology, Nagoya University School of Medicine
e-mail:

Abstract

In radiotherapy the dose delivery techniques are evolved rapidly. Intensity-modulated radiotherapy (IMRT) has non-uniform complex distribution and varying two-dimensional (2D) dose distribution. Therefore it is necessary to obtain 2D data. The radiographic film is more commonly used in this situation. The radiographic film features high resolution, and obtaining 2D data easily. In radiographic film dosimetry, the film is a few deflected from the beam axis at each facility. However, the adequate length of shift and the affect of shift do not clarify. Moreover, this study verifies the affect that the radiographic film deflected from the beam axis and that difference of measuring method by experimental measurement and Monte Carlo code EGS4. Experimental measurement and simulation performed two different arrangements. First method was a film protruded the upper edge of the phantom. Second method was the upper edge of a film matched that of the phantom. In each method, films were exposed in two patterns; one was the film was set under the beam axis and the other was the film was set 2 cm off from the beam axis. Density distributions obtained by the films were converted to percentage depth dose (PDD) curves. PDD curves obtained in the first method were not in good agreement with that of the ion chamber but PDD curves in the second was in good agreement in experimental measurement. However, PDD curves measured by the films accorded with PDD curve measured by ion chamber. Moreover, first method was more available than second method.

1. Introduction

In radiotherapy, as intensity-modulated radiotherapy (IMRT) and dynamic delivery techniques, the dose delivery techniques are evolved rapidly. IMRT has non-uniform complex distribution and varying two-dimensional (2D) dose distribution. Therefore it is necessary to obtain 2D data. The radiographic film is more commonly used in this situation. The radiographic film features high resolution, and obtaining 2D data easily. These features indicate that the radiographic film is available, but the radiographic film dosimetry has some problems such as film handling, quality control and energy dependence.

In radiographic film dosimetry, the film is a few deflected from the beam axis at each facility. If the film under the beam axis, the primary photon was incident into the film first and scattered by the film. Therefore the dose distributions obtained from the film did not differ from the dose distribution in water equivalent phantom. Thus, the

film was set a few off from the beam axis. However the adequate length of the shift and the affect of the shift do not clarify and the standard of measuring method by radiographic film dosimetry is not firm. This study verifies the affect of the radiographic film deflected from the beam axis and that of difference in two measuring methods by experimental measurement and Monte Carlo code EGS4.

2. Materials and Methods

2.1 Film measurements

The radiographic film used in this study was Kodak X-Omat V film in Ready Pack. The film was exposed 1.17 MeV and 1.33 MeV (Co-60 gamma rays) by 10 x 10 cm^2 field and the irradiation time is 500 seconds. The phantom was tough water phantom (30 x 30 x 30 cm^3). Film calibration was carried out known dose at eight depths (0 to 20 cm). This measurement was executed in two cases. As shown in Fig.1, the first method was the film protruded the upper edge of phantom, and as shown in Fig.2, the second was the upper edge of film matched with that of phantom. Furthermore, the film was exposed in two patterns, under the beam axis, and deflected 2 cm from beam axis. The exposed films were processed under the same conditions using automatic film processor. Each film was digitalized and read by software of our own composition.

2.2 Monte Carlo simulation using EGS4

The simulation geometry reflected the film measurement arrangement with accuracy, but in the case shown in Fig.2, the geometry was reenacted simply. The elemental composition of film, fraction by weight, was H: 0.023948, C: 0.222374, N: 0.099407, O: 0.473944, Br: 0.076736 and Ag: 0.103592; and the density was 1.731 g / cm^3 [1]. The composition of the paper used in Ready Pack for prevention of light-transmittance was assumed cellulose (C_6HO_8) and the density was 0.8050 g / cm^3. This paper wrapped the film and its thickness was 0.3 mm. Incident particles were 1.17 MeV and 1.33 MeV (Co-60 gamma rays) and the irradiation field size was 10 x 10 cm^2.

3. Results and Discussions

3.1 Film protruded from upper edge of phantom

Fig.3 (a) shows that percentage depth dose (PDD) curves measured by the protruded film. PDD curve measured by the ion chamber plotted in, too. PDD curves are obtained from two measurement patterns that the film under the beam axis and shifted approximately coincided, but PDD curves obtained from the films do not accord with the curve measured by the ion chamber. Fig.3 (b) shows the PDD curves calculated by EGS4. PDD curves calculated in two patterns almost agreed, but any curves do not accord with the curve measured by the ion chamber.

PDD curves obtained from any situation did not accord with the PDD curve measured by the ion chamber. Consequentially, primary photon could be influenced by the film protruded from upper edge of phantom. However, both PDD curves obtained from the film measurement and those calculated by EGS4 showed much the same tendency. This indicated that if the geometry in EGS4 reflected the arrangement of the film measurement, almost the same results could be acquired with EGS4 calculation.

3.2 Upper edge of film matched with that of phantom

Fig.4 (a) shows that PDD curves measured by the film that upper edge of the film matched with that of phantom. The data in build up region is not obtained properly. This is subjected to the software to read. However, PDD curve obtained from the deflected film accords with the curve measured by the ion chamber. Fig.4 (b) shows that PDD curves calculated by EGS4. PDD curves are removed from the curve measured by the ion chamber.

The PDD curves obtained from measurement and calculated were not in good agreement. However, PDD

curves measured by the film and the ion chamber were in good agreement. Therefore, the second measuring method was better than the first. However, in the first measuring method, PDD curves measured by the films and calculated are in good agreement. Therefore, reflecting the film measurement arrangement with accuracy made the PDD curves measured by the film measurement approach possible.

4. Conclusions

In this study, we cannot refer to the affect of deflecting the beam axis. However, as shown in Fig.3 and Fig.4, the PDD curves measured by the film protruded from upper edge of phantom are better than another. Therefore, as a result, we can suggest that the measuring method that the film protruded from upper edge of phantom is not appropriate.

References

1) Å. Palm, A. S. Kirov, and T. LoSasso, "Predicting energy response of radiographic film in a 6 MV x-ray beam using Monte Carlo calculated fluence spectra and absorbed dose," Int. Med. Phys. **31**(12), 3168-3178 (2004).

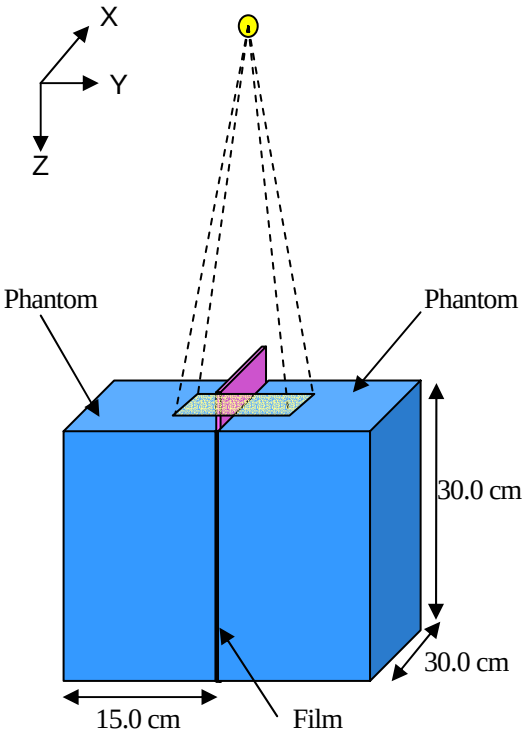

Fig.1 The geometry that the film was protruded the upper edge of the phantom (the first method).

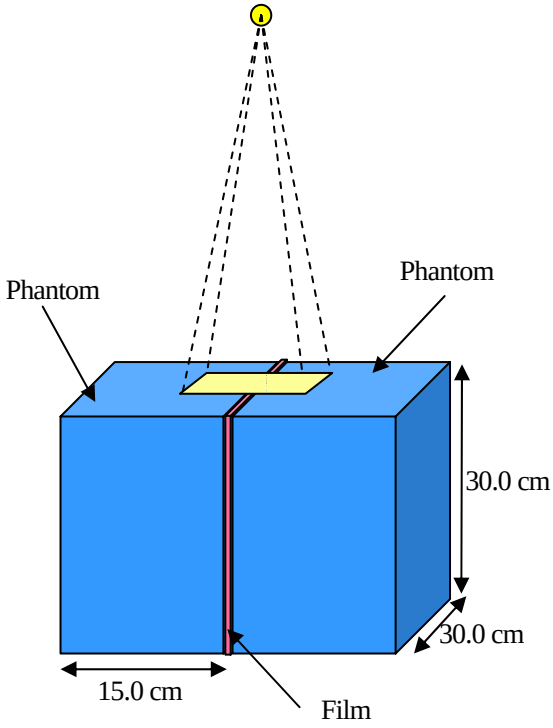

Fig.2 The geometry that the upper edge of the film matched with that of the phantom (the second method).

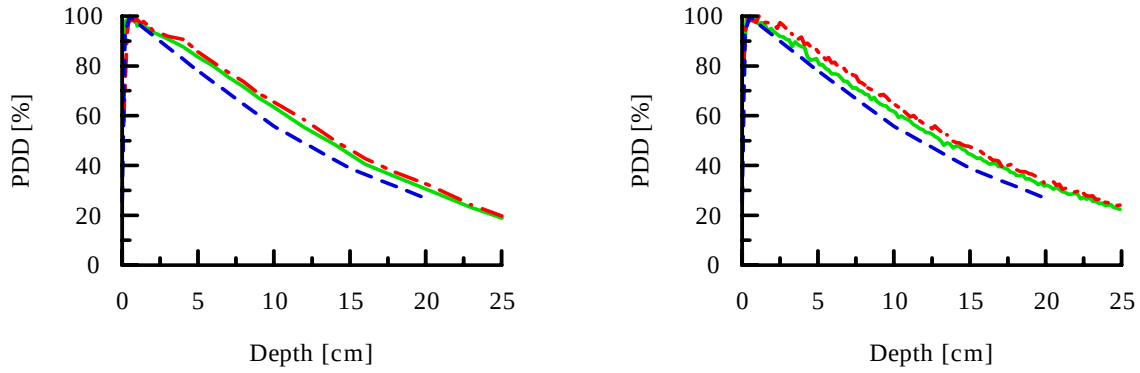

(a) (b)

Fig.3 The solid line (green) is the PDD curve measured by the film that set under the beam axis. The dash-dot line (red) is the PDD curve measured by the film that deflected from the beam axis. The dash line (blue) is the PDD curve measured by the ion chamber. The PDD curves in (a) were measured by the films in the first method and the ion chamber. (b) The PDD curves in (b) were calculated by EGS4.

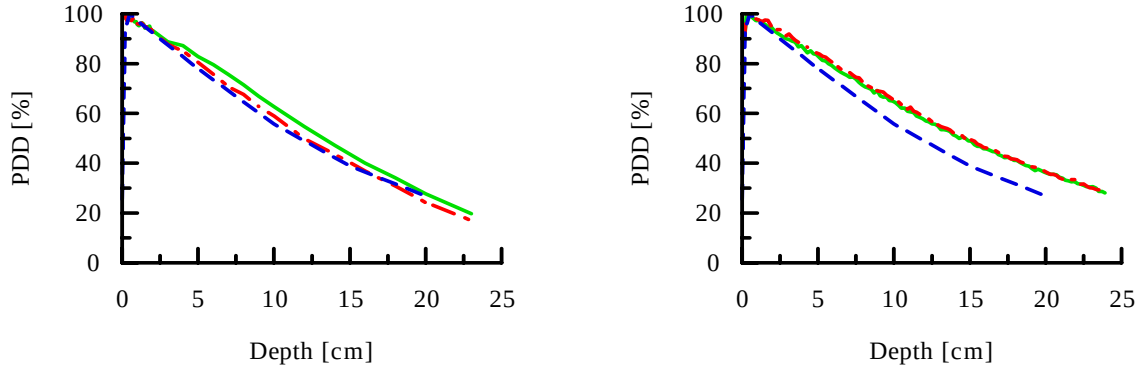

(a) (b)

Fig.4 The solid line (green) is the PDD curve measured by the film that set under the beam axis. The dash-dot line (red) is the PDD curve measured by the film that deflected from the beam axis. The dash line (blue) is the PDD curve measured by the ion chamber. The PDD curves in (a) were measured by the films in the second method and the ion chamber. (b) The PDD curves in (b) were calculated by EGS4.

STUDY ON THE ESTABLISHMENT OF THE RADIATION SAFETY STANDARD FOR Y-90 IN NUCLEAR MEDICINE

I. Yamaguchi[1], H. Narita[2], K. Morozumi[3], and T. Aburano[4]

[1]Department of Environmental Health, National Institute of Public Health, Saitama 351-0197, Japan,
[2]Department of Radiology, Jikei Medical University Hospital, Tokyo 105-8461, Japan
Department of Radiology, Saitama Cardiovascular and Respiratory Center, Saitama 360-0105, Japan
[4] Department of Radiology, Asahikawa Medical College, Hokkaido 078-8510, Japan
e-mail: drhyama@niph.go.jp

Abstract

To establish the radiation safety standard for radioactive immune therapy using Y-90, scenarios of radiation exposure to workers and the public were introduced and the radiation doses were estimated. The radiation doses were estimated supposing the following scenarios. 1) Disclosure of Y-90 by the accident at the time of conveyance. 2) At the time of intravenous administration. (1) External exposure of medical workers during administration of Y-90 to patients. (2) The subcutaneous tissue absorbed dose of the patient by accidental disclosure from the vein. 3) External exposure of the person who contacted the patient after administration of Y-90.(1) Radiation dose to other patients. (2) Radiation dose to hematologist during the examination of lymph gland palpation. 4) Internal exposure by polluted Y-90. 5) The dose rate around a drainage storage tank in a hospital and a sludge tub in sewage disposal plant. 6) Internal exposure by oral ingestion of river water contained Y-90. 7) Other environmental releases of Y-90 from patients. The fundamental data for a medical radiation safety standard of nuclear medicine using Y-90 were obtained by simulation calculation. It is not necessary to isolate patients prescribed Y-90 from the viewpoint of radiation safety.

1. Introduction

In order to develop useful and safe medical products and pharmaceuticals, it is essential to investigate the efficacy, efficiency, effectiveness, and safety of pharmaceuticals. Among the clinical studies performed in order to obtain approval as a medical supply is the clinical trial. These are important elements of medical supply development. Since a clinical trial targets humans, it is performed in a medical institution. Moreover, in order to secure safety, it is necessary to conduct the trial according to the requirements of "the ministerial ordinance regarding the standard of implementation of clinical trials of medical supplies" of the Ministry of Health, Labor and Welfare in Japan. The basic idea of this ministerial ordinance is the spontaneous "consent" of participants based on the "explanation" from a physician. Clinical trials can therefore be said to be realized by the goodwill of the volunteers. It is necessary to prepare rules so that a clinical trial can be conducted appropriately from the viewpoints of science and ethics. Furthermore, in order to smoothly promote clinical trials using radiation, securing radiation safety is important.

Radioimmunotherapy (RIT) is a novel modality for treating indolent Non-Hodgkin's lymphoma (NHL), using monoclonal antibodies to target tumor cells with systemic, low-dose radiation. The chimeric antibody (brand name Rituxan) to CD20 that is the surface antigen of B cells is widely used as a pharmaceutical for malignant lymphoma.

Ibritumomab tiuxetan (Zevalinw; Schering AG, Berlin, Germany), which has the same variable domain as Rituxan and carries out Y-90 to the mouse antibody, was approved by U.S. FDA in February 2002 as the first RIT approved for use in relapsed/refractory indolent NHL [1] [2] [3]. To establish the radiation safety standard for radioactive immune therapy using Y-90, scenarios of radiation exposure to workers and the public were introduced and the radiation doses were estimated.

2. Materials and Methods

The radiation doses were estimated assuming the following scenarios. The amount of Y-90 was assumed to be 0.4 mCi/kg. A patient's weight was assumed to be 60 kg. Therefore, the amount of Y-90 was set to 888 MBq / patient. The kinetic energy distribution of the electrons emitted from Y-90 was quoted from Table D.1 of ICRU report 56 and is shown in Fig. 1.

2.1 Radiation dose from discharged Y-90 in an accident during conveyance to hospital

The dose was calculated assuming the discharge of Y-90 from a container in an accident during conveyance to a medical institution. The amount of leakage from the container was assumed to be 1 MBq/m^2.

2.2 At the time of intravenous administration

2-2-1. External exposure of medical workers during administration of Y-90 to patients

The skin dose of a medical worker over 3 months was calculated assuming that one patient was administered a dose every week. For ibritumomab tiuxetan, the administration time is recommended to be 10 minutes or more. Two administration methods were assumed. In both scenarios, the number of patients was assumed to be one each week.

A. Syringe injector: It was assumed that a medical worker held an acrylic syringe for 30 seconds for preparation. The thicknesses of the acrylic syringe were assumed to be 1 mm and 2 mm. The finger of the medical worker was represented by a water cylinder around the acrylic syringe. The absorbed dose to a 7-mm depth was calculated as the skin-absorbed dose.

B. Drip infusion: It was assumed that intravenous drip infusion was performed with a 1-mm-thick bottle with as 2.5-cm radius for 1 hour. The medical worker was assumed to stay 30 cm and 100 cm from the patient.

2-2-2. Radiation doses to patient skin due to inadvertent intravenous injection of Y-90

The rate of subcutaneous extravasation was 10%. The depth of the leakage layer was 100 μm and the thickness of this layer was 20 μm. Leaked Y-90 and the dose estimation region was cylindrical and the radius at the bottom was set to 30 mm. The depth of the dose-estimated layer and effective half-life of extravasated Y-90 in subcutaneous tissue were made into variables.

2.3 External exposure of the person who made contact with the patient after administration of Y-90

2-3-1. Radiation dose to other patients

The target was assumed to be spherical water and spherical acrylic, and Y-90 was assumed to be at the center of the sphere. The radiation dose around the target was calculated. Moreover, the dose rate around the patient was calculated assuming that the patient was a pillar of 30 cm in diameter. The element composition of the patient was assumed to be C: 60%, H: 8%, O: 32% (composition rate by the number of atoms), with a density of 1.9 g/cm^3. The depth of Y-90 was assumed to be 0.3 to 1 cm, and 0.9 to 1 cm from the surface, and it was assumed that it was distributed equally to a 10-cm-high domain 30 degrees toward the evaluation direction side. The occupational factor was set to 0.5 at the time of staying 1 m from the patient[4]. The maximum number of injected patients who stayed near other patients was assumed to be 4 each year.

2-3-2. Radiation dose to hematologists during lymph gland palpation

The dose absorbed through the skin of the fingers of hematologists who palpate the lymph gland with uptake of Y-90 was estimated. It was assumed that Y-90 was equally distributed in the lymph gland at a depth of 0.3 to 1 cm from the skin surface. A doctor's finger was considered to be 1 cm in thickness, and skin-absorbed dose was calculated at a 1-mm depth from the surface.

2.4 Internal exposure to contaminated Y-90

The equivalent dose of each organ from accidental oral ingestion due to contamination was calculated based on the compartment model of ICRP (International Commission on Radiation Protection). The calculation was conducted as follows. The intake was 1 MBq, which is equal to 1/1,000 of the administrative dose of 1 GBq. The INDES code of the Japan Atomic Energy Agency was used.

2.5 The dose rate around a drainage storage tank in a hospital and a sludge tub in a sewage disposal plant

The dose rate around a waste water tank and sludge-processing tub was calculated. It is assumed that the whole quantity of Y-90 shifted to the drainage system of the medical institution, and it is assumed that these radioactive nuclides were entirely collected into a sludge-processing tub in a public sewage disposal plant.

2.6 Internal exposure by oral ingestion of river water containing Y-90

The number of patients with B cell malignant lymphoma in Osaka was assumed to be 200 each year. The amount of activity for administration to a patient was assumed to be 1480 MBq. The annual average flux of the Yodo River was assumed to be 4.1 Tl each year.

2.7 Other environmental releases of Y-90 from patients

Air pollution with particulates containing 1 kBq Y-90 per cubic meter of was assumed.

3. Results

3.1 Radiation dose from discharged Y-90 in an accident during conveyance to hospital

Even if the contamination of Y-90 was 1 MBq per square meter, the public dose did not exceed 1 mSv. For this reason, even if a radiation source container of Y-90 is damaged, with adequate zoning for the contaminated area and appropriate handling of the contamination, the radiation dose to the public is at a fully controllable level.

3.2 At the time of intravenous administration

3-2-1. External exposure of medical workers during administration of Y-90 to patients

A. Syringe injector: The skin-absorbed dose of a worker's finger was 240 mGy for 3 months when the thickness of the acrylic syringe was 1 mm. On the other hand, the skin-absorbed dose of a worker's finger was 28 mGy for 3 months when the thickness of acrylic syringe was 2 mm. Figure 2 shows the trajectory of radiation for 100 decaies of Y-90 in the syringe.

B. Drip infusion: At 30 cm from the bottle, the medical worker's skin-absorbed dose was 140 mGy for 3 months. On the other hand, at 100 cm from the bottle, it was 11 mGy for 3 months.

3-2-2. Radiation doses to patient skin due to inadvertent intravenous injection of Y-90

The subcutaneous tissue-absorbed dose of the patient at accidental leakage from a vein administered 10% Y-90 was estimated to be about 5Gy when the effective half-life of Y-90 in the subcutaneous tissue was 1 hour(Figure 3).

3.3 External exposure of the person who made contact with the patient after administration of Y-90

3-3-1. Radiation dose to other patients

Figure 4 to Fig. 6 show the dose rate around the sphere. The closed circles show the calculated dose rate for the water sphere. The closed squares show the calculated dose rate for the acrylic sphere. Figure 4 shows the dose rate of the surface. Figure 5 shows the dose rate at a depth of 1cm. Figure 6 shows the dose rate of the mean absorbed dose. The horizontal solid line indicates the value of the target of atomic number 20 in the manual of the Nuclear Safety Technology Center in Japan. The horizontal broken line indicates the value of the target of water in the same manual.

Figure 7 shows the dose rate around the patient. The maximum radioactivity that was below 5 mSv for four patients' care was 1.7 GBq when the accumulated depth of Y-90 was 0.3 to 1 cm from the surface. On the other hand, when the accumulated depth of Y-90 was 0.9 to 1 cm from the surface, the maximum activity was 74 GBq.

3-3-2. Radiation dose to hematologists during lymph gland palpation

When 5 MBq of Y-90 was assumed to accumulate in the lymph glands, the skin-absorbed dose rate of the finger of the hematologist who palpates lymph glands at the time of accumulation was 780±30 μGy/h. The figure for the decay of 5 MBq of Y-90 for 5 minutes is 1.5×10^9. Therefore, if a medical worker touches the contaminated area directly for 5 minutes, the skin dose reaches about 20 mGy.

3.4 Internal exposure to contaminated Y-90

Oral ingestion of Y-90 can result in comparatively high doses via the alimentary canal. When a 5-year-old child intakes 1 MBq of Y-90 accidentally, the equivalent dose of the lower part of the large intestine was calculated to be 120 mSv.

3.5 The dose rate around a drainage storage tank in a hospital and a sludge tub in sewage disposal plant

Even if a tank collects whole quantity of administrated dose, the accumulated dose from one patient 1 m from the tank is 14 μSv.

3.6 Internal exposure by oral ingestion of river water containing Y-90

The concentration of Y-90 in the river was estimated to be 0.08 Bq / l. Since oral intake of water is 2 l per day, the amount of Y-90 was calculated to be 60 Bq per year. Therefore, internal exposure to Y-90 was estimated to be 0.16 μSv per year when the effective dose coefficient for internal Y-90 was 2.7E-06 mSv / Bq.

3.7 Other environmental releases of Y-90 from patients

Even if the concentration of polluted Y-90 in the air is 1 kBq per cubic meter, the external effective dose over one year is estimated to be 50 μSv. On the other hand, the internal effective dose over 8 hours was 20 μSv.

4. Discussion

The dose rate around a patient was comparatively low. In the assumed scenario, neither the care worker nor other patients exceeded the dose limit. The radiation dose to workers in municipal sewage treatment facilities was also below the dose limit. For this reason, it seems unnecessary to isolate patients prescribed Y-90 from the viewpoint of radiation safety.

On the evaluation of the braking radiation from a body containing Y-90, the self-absorption of the body depends relatively largely on physique. At the time of accumulation to a shallow layer, a dose becomes large. Assuming that the hematologist takes 20 minutes to examine one patient, the skin dose was 12±0.5 mGy. Therefore, the dose limit is not exceeded even if the hematologist examines 40 patients every year. However, the dose rate from surface contamination of Y-90 was large. In ICRU Report 56, the skin-absorbed dose rate per skin surface pollution density of 1 Bq / cm^2 is indicated to be 1760 nGy/h. For this reason, it is recommended that direct touching of polluted Y-90 should be avoided. When a medical worker touches Y-90, it is

necessary to consider internal exposure.

Since the kinetic energy of electrons emitted from Y-90 is relatively high, caution is required at the time of administration. A correspondence manual for injection failure may be necessary.

5. Conclusion

The fundamental data for a medical radiation safety standard of nuclear medicine using Y-90 were obtained by simulation calculation. It is not necessary to isolate patients prescribed Y-90 from the viewpoint of radiation safety.

Acknowledgment

This study was supported by the Health and Labour Sciences Research Grants on from Ministry of Health, Labour and Welfare (Research on Health Technology Assessment), Ministry of Health, Welfare and Labour, Japan.

References

1) Kaminski MS, Zasadny KR, Francis IR, Milik AW, Ross CW, Moon SD, Crawford SM, Burgess JM, Petry NA, Butchko GM, et al, "Radioimmunotherapy of B-cell lymphoma with 131I anti-B1 (anti-CD20) antibody," N Engl J Med, **329**, 459-465, (1993).
2) Kaminski MS, Tuck M, Estes J, Kolstad A, Ross CW, Zasadny K, Regan D, Kison P, Fisher S, Kroll S, Wahl RL, "^{131}I-Tositumomab Therapy as Initial Treatment for Follicular Lymphoma," N Engl J Med, **352**, 441-449, (2005).
3) A. Hagenbeek1, V. Lewington," Report of a European consensus workshop to develop recommendations for the optimal use of 90Y-ibritumomab tiuxetan (Zevalin®) in lymphoma," Annals of Oncology, **16**,786-792, (2005).
4) International Commission on Radiological Protection, Release of patients after therapy with unsealed radionuclides, ICRP Publication 94, Ann ICRP, **34**(2),(2005).

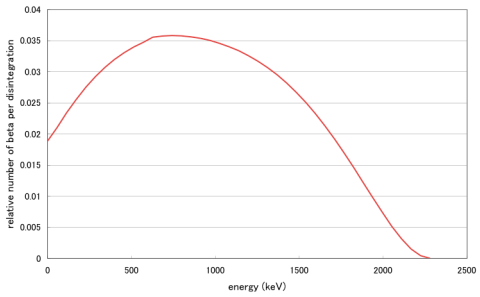

Figure 1. The energy distribution of electrons of Y-90

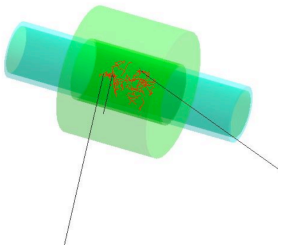

Figure 2. The trajectory of radiation for 100 decaies of Y-90 in the syringe. The thickness of syringe is 2mm

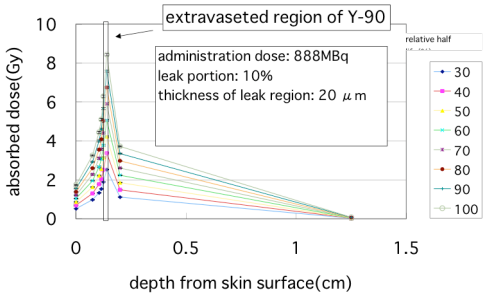

Figure 3. Radiation doses to patient skin due to inadvertent intravenous injection of Y-90

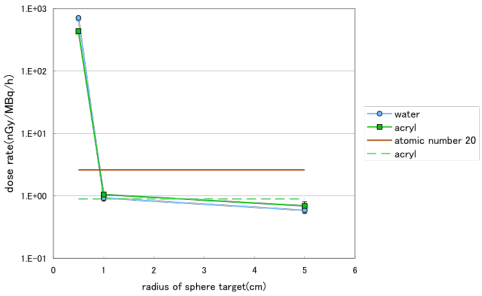

Figure 4 Dose rate (H(0.07) around sphere target

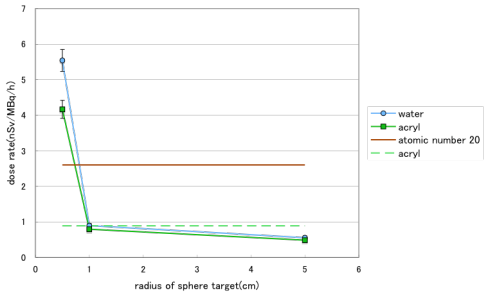

Figure 5. Dose rate (H(10) around sphere target

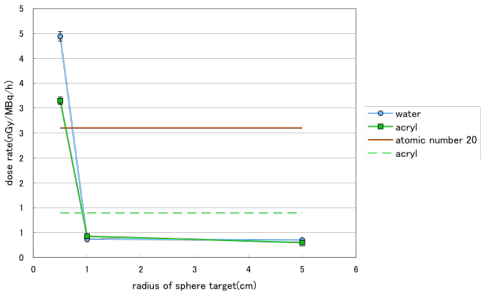

Figure 6. Dose rate (mean body dose) around sphere target

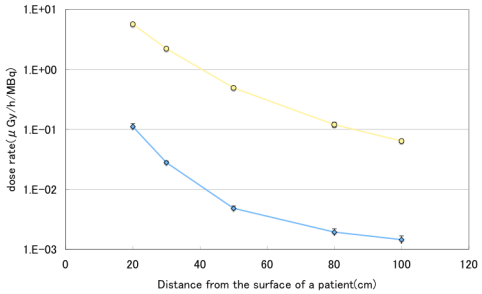

Figure 7. Dose rate (H(10)) around a patient

Absorbed Doses to the Urinary Bladder Wall Considering Radiosensitive Cells

Y. Watanabe, S. Kinase and K. Saito

Japan Atomic Energy Agency, Tokai-mura, Naka-gun, Ibaraki 319-1195, Japan
e-mail: watanabe.yoko@jaea.go.jp

Abstract

Dose evaluation of the urinary bladder considering radiosensitive cells is needed for more realistic dose assessment. The present study has developed a simple bladder model in order to evaluate the energy deposition on the radiosensitive basal cells in the bladder wall. The photon and electron SAFs to the basal cells as well as the whole bladder wall were evaluated using EGS4 code. In addition, S values for the nine radionuclides were obtained. As a result, the photon SAFs are larger for the basal cells than for the whole bladder wall at the energies from 10 to 30 keV. The electron SAFs obtained in the present study increase with the electron energy, indicating that electron SAFs are not constant as used in the radiological protection. S values of the present study are smaller than those of previous study, particularly for the beta emitters.

1. Introduction

The radionuclides entered the body by ingestion, inhalation or injection are partially excreted by urine. Hence, dose evaluation of urinary bladder is important from the standpoint of radiological protection and diagnostic procedures [1]. In particular, it is necessary in diagnostic procedures since absorbed dose from some radiopharmaceuticals is higher for the urinary bladder than for the other organs [2]. In evaluating internal dose, the specific absorbed fraction (SAF) – the fraction of energy emitted as a specified radiation type in a source tissue which is absorbed in 1 kg of a target tissue- and S value –the mean absorbed dose to the target organ per unit cumulated activity in the source organ- are generally used. Both the Medical International Radiation Dose (MIRD) committee [1,3] and the Internal Commission on Radiological Protection (ICRP) [4-7] have provided the estimates of SAFs for the photon and electron sources which are uniformly distributed in the bladder contents of a MIRD 5 type phantom. The photon SAFs for the whole bladder wall was provided using Monte Carlo simulation [3], while electron SAFs for the bladder mucous membrane were taken to be constant with an assumption that half of the emitted electrons from the source is absorbed in the target tissue [5]. In the evaluation of absorbed dose, SAFs were converted into S values considering the radiation of radionuclides.

To our knowledge, previous works [1,8-10] did not determine the depth of the radiosensitive cells in the bladder wall since little was known about them. However, recent study has reported the existence of germinal basal cells in the epithelium [11]. Since the absorbed dose to the radiosensitive cells is considered to relate to the radiation risks, dose evaluation considering basal cells is necessary.

The present study has developed a multi-layered simple bladder model and evaluated both photon and electron SAFs for the basal cells as well as the whole bladder wall using EGS4 code. Besides, S values were calculated for the nine radionuclides: ^{11}C, ^{13}N, ^{15}O, ^{18}F, ^{89}Sr, ^{90}Sr, ^{90}Y, ^{99m}Tc and ^{123}I.

2. Material and Methods

2.1 Bladder model

Figure 1 shows the bladder model that was developed for the simulation. The model is similar to the ellipsoid model of MIRD 5 type phantom [3]. The bladder wall (2,520 μm) was divided into multi-layers of 10 μm thick from the inner surface to 600 μm in depth since basal cells are 5 – 10 μm thick [11]. The basal cell layers at the depth of 70 - 80 μm and 140 - 150 μm from the inner surface were chosen for the evaluation as they exist at the depth of 70 -140 μm depending on the degree of the bladder stretch [11]. The component of ICRP urinary bladder was used for the bladder model [12]. The mass of the bladder wall and the bladder contents were 0.05 kg [12] and 0.211 kg [13], respectively.

2.2 SAF and S value evaluation

The energy deposition on the urinary bladder from monoenergetic photons and electrons in the bladder contents were calculated in the energy range 10 keV – 4 keV using EGS4 code [14]. The SAFs were evaluated as the fraction of energy absorbed in the target tissue that was released in the bladder contents divided by the mass of the target tissue. It is assumed that the sources of photons and electrons in the bladder contents were uniformly distributed. The number of histories for the simulations of photons and electrons was basically determined to reduce the statistical uncertainties below 5%. The exceptions were electrons with low energies (<100 keV). The worst case was approximately 50% at 10 keV for 140 - 150 μm basal cell layer. No variance reduction was used. The cross-section photons were taken from PHOTX [15] and the electron ranges were taken from ICRU report 37 [16]. The photon SAFs were evaluated considering the transport of the secondary electrons.

S values to the whole bladder wall and the basal cell layers from uniformly distributed radionuclides in the bladder contents were calculated, using the results of the SAFs. The SAFs and the decay mode of radionuclides were considered for the evaluation. S values were obtained for a) fission products (^{89}Sr, ^{90}Sr, ^{90}Y), b) radionuclides for radiopharmaceuticals (^{99m}Tc, ^{123}I), and c) radionuclides for PET (^{11}C, ^{13}N, ^{15}O, ^{18}F). Table 1 shows the energy and intensity (>0.01) of photons. The maximum and mean energy of beta rays are shown in Table 2. The photon energy and the beta spectra of radionuclides were taken from DECDC2 [17] as well as ICRU Report 56 [18]. As for the S value evaluation of ^{99m}Tc and ^{123}I, internal conversion and Auger electrons were included.

3. Results and Discussion

3.1 SAF evaluation

The photon SAFs to 70 - 80 μm and 140 - 150 μm basal cell layers and the whole bladder wall are shown in Figure 2 (a). The photon SAFs of ICRP are also shown for comparison. The evaluated results of SAFs to the whole bladder wall agreed well with those listed in ICRP except in the energy range 10 - 50 keV. The discrepancy in this energy region is considered to be the use of different bladder wall mass, nuclear data as well as calculation codes. The photon SAFs to the basal cell layers are larger than those of ICRP –the SAFs to the whole bladder wall - in the energy range 10 - 30 keV. This result indicates that the evaluation of photon SAFs considering radiosensitive cells is necessary, particularly in the low energy region.

Figure 2 (b) shows electron SAFs to 70 - 80 μm and 140 - 150 μm basal cell layers and the whole bladder wall. In the figure, electron SAF of ICRP is also shown. Although the electron SAF used in the radiological protection was constant, the SAFs obtained in the present study increase with the electron energy in the range 10 keV - 4 MeV. The electron SAFs to the basal cell layers show sharp rise at 50 keV for 70 - 80 μm layer and 100 keV for 140 - 150 μm layer, since SAFs are directly contributed from the primary electrons in the energy greater than those values. Bremsstrahlung contributes the SAF in the energy range where primary electrons do not reach target

tissues. Hence, electron SAFs do not reach zero even though its energy is below 50 keV for 70-80 μm layer and 100 keV for 140-150 μm layer.

3.2 S value evaluation

Figure 3 (a) shows the S values of 'pure' beta emitters (^{89}Sr, ^{90}Sr, ^{90}Y). The S values obtained in the present study were less than half of conventional values, indicating that S values used for the radiation protection were overestimated. The S values decrease with the mean energy of radionuclides and with increasing target tissue mass. This suggests that the mean energy of beta rays and the mass of target tissues are the factors that directly influence the S value evaluation.

The S values of radionuclides used for radiopharmaceuticals (^{99m}Tc, ^{123}I) are shown in Figure 3 (b). The S values of ^{99m}Tc and ^{123}I to basal cell layers are 1.2 and 1.3 times larger than those of ICRP, indicating that the conventional S values for photon emitters are slightly underestimated.

Figure 3 (c) shows the S values of radionuclides (^{11}C, ^{13}N, ^{15}O, ^{18}F) used for positron emission tomography (PET). The contribution from positrons and two annihilation photons are presented separately. Since the contributions from photons in all cases are almost the same, the difference is attributed to the contribution from positrons. As described before, the S values from beta rays decrease with their mean energy and with increasing target tissues mass. These results demonstrate that S values for radionuclides for PET were also overestimated and dose evaluation considering radiosensitive cells is required for the accurate dose assessment.

4. Conclusions

The multi-layered simple bladder model was developed for the dose evaluation of radiosensitive basal cells in the bladder wall. The SAFs for both photons and electrons to the basal cell layers and the whole bladder wall were evaluated using EGS4 and obtained SAFs were converted into S values for the nine radionuclides. Both photon and electron SAFs are different from those currently used in radiological protection. Furthermore, S values of beta emitters were found to be overestimated, especially for the radionuclides that emit low energy of beta rays. The present study concludes that the dose evaluation considering radiosensitive basal cells is necessary for more realistic dose assessment.

References

1) S. R Thomas, M. G. Stabin, C-T. Chen, and R. C. Samaratunga, "A Dynamic Urinary Bladder Model for Radiation Dose Calculations," MIRD Pamphlet No.14, *J. Nucl. Med.*, **40(4)**, 102-123 (1999).
2) ICRP, "Radiation Dose to Patients from Radiopharmaceuticals," ICRP Publ. 53, Pergamon Press, Oxford (1987).
3) W. S. Synder, M. R. Ford, G. G. Warner, and H. L. Jr. Fisher, "Estimates of Absorbed Fractions for Monoenergetic Photon Sources Uniformly Distributed in Carious Organs of a Heterogeneous Phantom," MIRD Pamphlet No.5, *J. Nucl. Med.*, Suppl. 3, **10**, 5-52 (1969).
4) ICRP, "Report of the Task Group on Reference Man," ICRP Publ. 23, Pergamon Press, Oxford (1975).
5) ICRP, "Limits for Intakes of Radionuclides by Workers," ICRP Publ. 30, Pergamon Press, Oxford (1979).
6) ICRP, "Dose Coefficients for Intakes of Radionuclides by Workers," ICRP Publ. 68, Pergamon Press, Oxford (1995).
7) M. Christy. and K. F. Eckerman, "Specific Absorbed Fractions of Energy at Various Ages from Internal Photon Sources. VII. Adult Male," ORNL, TM-8381/V7 (1987).

8) S. Kinase, M. Zankl, J. Funabiki, H. Noguchi, and K. Saito, "Evaluation of S Values for Beta-ray Emitters within the Urinary Bladder," *J. Nucl. Sci. Technol.*, Suppl.4, 136-139 (2004).
9) J. B. Stubbs, J. F. Evans and M. G. Stabin, "Radiation Absorbed Doses to the Walls of Hollow Organs," *J. Nucl. Med.*, **39**(11), 1989-1995 (1998).
10) A. A. Bolster and T. E. Hilditch, "The Radiation Dose to the Urinary Bladder in Radio-Iodine Therapy," *Phys. Med. Biol.*, **41**, 1993-2008 (1996).
11) S. A. Lewis, "Everything You Wanted to Know About the Bladder Epithelium but were Afraid to Ask," Am. *J. Physiol. Renal. Physiol.*, **278**, F867-F874 (2000).
12) ICRP, "Basic Anatomical and Physical Data for Use in Radiological Protection:Reference Values," ICRP Publ.89, Pergamon Press, Oxford (2002).
13) M. Christy and K. F. Eckerman, "Specific Absorbed Fractions of Energy at Various Ages from Internal Photon Sources. I. Methods," ORNL, TM-8381/V1 (1987).
14) W. R. Nelson, H. Hirayama, and D. W. O. Rogers, "The EGS4 Code System," SLAC 265 (1985).
15) RSIC, DLC-136/PHOTX Photon Interaction Cross Section Library (contributed by National Institute of Standards and Technology) (1989).
16) ICRU, "Stopping Powers for Electrons and Positrons," ICRU Report 37, Bethesda, Md. (1984).
17) A. Endo, Y. Yamaguchi, and K. Eckerman, "Nuclear Decay Data for Dosimetry Calculation Revised Data of ICRP Publ. 38," JAERI 1347 (2005).
18) ICRU, "Dosimetry of External Beta Rays for Radiation Protection," ICRU Report 56, Bethesda, Md. (1997).

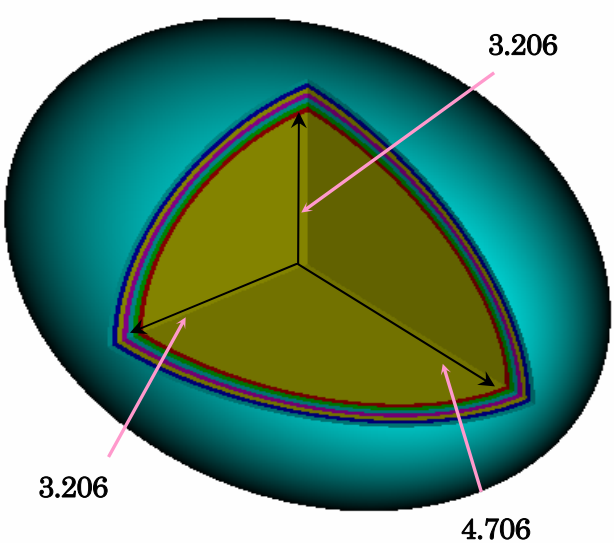

Figure 1. Multi-layered simple bladder model. unit: cm

Table 1. Photon energy and intensity of radionuclides[17)]

Nuclides	Energy (MeV)	Intensity (>0.01)
^{11}C	0.5110	2.00
^{13}N	0.5110	2.00
^{15}O	0.5110	2.00
^{18}F	0.5110	1.93
^{99m}Tc	0.0183	0.02
	0.0184	0.04
	0.1405	0.89
^{123}I	0.0038	0.03
	0.0040	0.02
	0.0272	0.25
	0.0275	0.46
	0.0309	0.04
	0.0310	0.09
	0.0317	0.03
	0.1589	0.83
	0.5290	0.01

Table 2. Mean and maximum energy of positron and electron emitters[17)]

Nuclides	Mean energy (MeV)	Maximum energy (MeV)	Intensity
^{11}C	0.386	0.960	9.98×10^{-1}
^{13}N	0.492	1.199	9.98×10^{-1}
^{15}O	0.735	1.732	9.99×10^{-1}
^{18}F	0.250	0.634	9.67×10^{-1}
^{89}Sr	0.210		9.62×10^{-5}
	0.583	1.492	1.00×10^{0}
^{90}Sr	0.196	0.546	1.00×10^{0}
^{90}Y	0.025		1.40×10^{-8}
	0.186	2.282	1.15×10^{-4}
	0.934		1.00×10^{0}
^{99m}Tc	0.030		1.08×10^{-6}
	0.102	0.436	2.59×10^{-5}
	0.152		9.98×10^{-6}

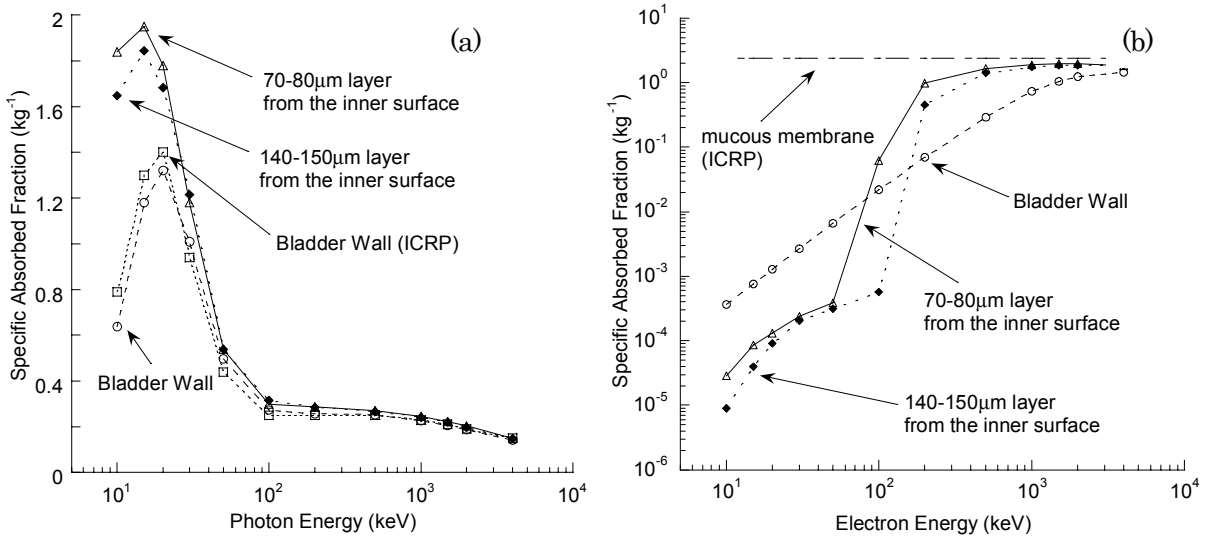

Figure 2. Specific absorbed fraction of energy for monoenergetic (a) photon and (b) electron sources with bladder contents as the source and bladder as the target organ.

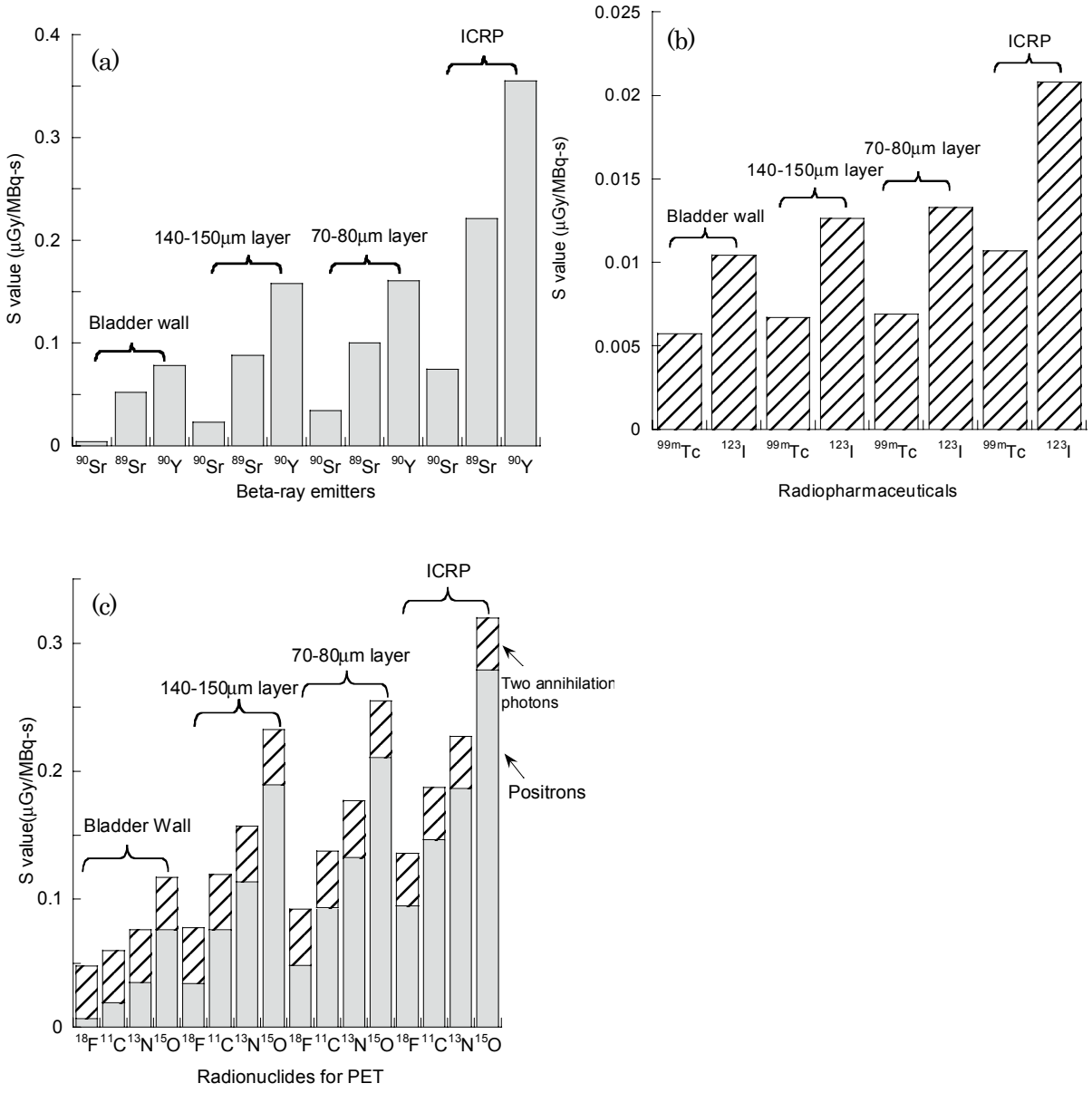

Figure 3. S values for (a) beta ray emitters (b) radiopharmaceuticals and (c) radionuclides for PET distributed in the bladder contents.

EVALUATION OF THE PATIENT INTERNAL ORGAN DOSES IN POSITRON EMISSION TOMOGRAPHY USING EGS4

K. Tsuda[1,2], S. Kinase[2], M. Fukushi[1], K. Saito[2]

[1]Tokyo Metropolitan University Graduate School of Health Sciences,
Higashiogu, Arakawa City, Tokyo, 116-8551, Japan
[2]Research Group for Radiation Effect Analysis,
Nuclear Energy Basic Engineering Research Sector,
Japan Atomic Energy Agency, Tokai-mura, Naka-gun, Ibaraki 319-1195, Japan
e-mail: tsuda.keisuke@jaea.go.jp

Abstract

In recent years, positron emission tomography (PET) has attracted considerable attention in the diagnosis of cancer. The aim of the present work is the development of evaluation method for the brain absorbed dose in ^{18}F-FDG PET. The evaluation method combining the experimental and the simulation evaluation has been studied. Dose measurements on the surface of body were carried out using photo luminescence dosimeters (PLDs) for volunteers, and the absorbed doses of PLD and brain were obtained by simulation using voxel phantoms. Consequently, the evaluation method was validated by several comparisons with experimental data, assuming that pharmacokinetics of FDG follows a biokinetic model suggested by the International Commission on Radiological Protection (ICRP). Furthermore, the regression equations that can estimate the brain absorbed dose from those at the brain surface were obtained. A simple but accurate method for evaluating organ doses from PLD measurements was established.

1. Introduction

Positron emission tomography (PET) is very effective in the diagnosis and management of patients with various types of cancers. PET using 2-[F-18] Fluoro-2deoxy-D-glucose (FDG) is an advanced imaging tool, based on the increased glucose consumption of cancer cells. FDG is widely used in conjunction with PET scans to examine glucose metabolism [1]. The examinations have recently become available in more than one hundred hospitals and have been approved under Japan's national health insurance program from April, 2002. It is anticipated that patients undergoing diagnosis or treatment would increase leading to significant enhancement of radiation exposure. However, the dose assessment is now being performed in a simple manner, and the assessed dose is considered to have large uncertainties. Hence, radiation dose assessments for individuals based on measurements are of great practical significance.

It is well accepted that absorbed dose per unit administered activity presented in the International Commission on Radiological Protection (ICRP) is used for organ dose assessment [2-4]. The ICRP, in its publications 53 [3] and 80 [4], presented tables of FDG doses derived from a model assuming specific uptake of FDG by organs such as the brain with the further assumption that all other activity is distributed uniformly in the body. In the data for the ICRP reference individual, however, data on Japanese are not reflected but those on Western Europeans and North Americans are used. Difference in metabolism and body structure might affect organ doses; moreover the organ doses are desired to be estimated by measurements for each specific case. It is therefore necessary to develop the reliable method for the

absorbed dose assessment of FDG PET on each individual based on measurements.

The present study was carried out to develop an evaluation method for the FDG brain absorbed dose on Japanese population. The dose evaluation method that combined the experimental and the Monte Carlo simulation evaluation has been studied. Furthermore, the regression equations that can estimate the brain absorbed dose from the absorbed dose at the brain surface are examined.

2. Materials and Methods

2.1 Experimental evaluation

The relationship between the absorbed dose at a glabella position and the cumulated activity of the brain was evaluated. The absorbed doses at the brain surface in FDG PET were measured using photo luminescence dosimeters (PLDs) (Chiyoda Technol Co. Ltd, Tokyo, Japan) in International Medical Center of Japan. The size of the PLD element was 8.5 mm in length and 1.5 mm in diameter. Twelve PLDs were placed at a glabella position. The mean administered activity was 400 MBq (from 359 to 402 MBq). The cumulated activity of the brain was evaluated using a biokinetic model of ICRP Publ.53 [1, 3]. As for five normal volunteers (three men, two women, age 21-24 years old, **Table 1**), the cumulated absorbed doses in PLDs for 30, 60, 90, 120, 180, 240 minutes were measured after an intravenous administration of FDG. None of them had a prior history of any major illness. All volunteers were prohibited from eating and drinking for 5 to 6 hours before the experiment.

2.2 Simulation evaluation

The relationship between cumulated absorbed dose and activity of the brain were evaluated using voxel phantoms and the Monte Carlo code, EGS4 [5, 6]. Japanese voxel phantoms (OTOKO, ONAGO, **Fig. 1**) [7] developed in Japan Atomic Energy Research Institute (JAERI) were used for the realistic calculation. The OTOKO and ONAGO phantoms were constructed from CT data of real human bodies. In the simulation model, PLDs were set on the surfaces of the phantoms at the same position to the actual measurements. FDG source of radiation was assumed to be uniformly distributed in the brain. Positrons were emitted from the FDG source. Photons (two annihilations) were emitted at the spot where the positron was stopped. The maximum and mean energies of ^{18}F were 634 keV and 250 keV, respectively [8]. The energy spectrum of positron was sampled in accordance with formula of KONOPINSKI [9]. The spectrum for the ^{18}F was taken from DECDC2 [8]. The numbers of histories of the simulations were basically determined to reduce statistical uncertainties below 5 %. The cross-section for photons were taken from PHOTX [10] and the data for electrons were taken from ICRU report 37 [11]. The uptake of FDG to the brain was assumed to be 8.5% based on the previous report [1]. Furthermore, the calculation results were compared with measurement results of PLD values to validate of the simulation.

3. Results and Discussion

3.1 Experimental evaluation

Figure 2 shows time-PLD cumulated absorbed dose curve after an intravenous administration of FDG in the experiment. PLD values of male and female average are shown in the figure as cumulated absorbed dose (Gy) per unit administered activity (MBq). Each PLD cumulated absorbed doses increases with an increase of time after an intravenous administration of FDG. The average dose of female tends to be larger than that of male. This difference is due not only to smaller overall body and organ sizes, but also to a larger biological uptake of FDG in the brain [12].

3.2 Cumulated activity of the brain

The cumulated activity of the brain with a biokinetic model is shown in **Fig. 3**. The curves were plotted in accordance with ICRP Publ.53 [3], in which 6 % of the administered tracer (FDG 1 MBq) was taken up by the brain with

an uptake half-time of 8 minutes and retained for a time which is long in relation to the radioactive half-life of ^{18}F. The cumulated activity reached the peak after an intravenous administration of FDG in about 30 minutes. The integration value of the brain cumulated activity increases in the similar way as experimental PLD value.

3.3 Simulation evaluation

In **Figs. 4** and **5**, temporal change of absorbed dose for FDG in the brain calculated using the OTOKO and the ONAGO phantoms are shown. The cumulated absorbed dose increases with increasing time after an intravenous administration of FDG. The brain cumulated absorbed dose is larger than that of the PLD values of the glabella position so that target positron contributes directly to the dose. The calculation of the present study was validated since the calculated doses of the PLD values are consistent with those of measurement. There is difference in the dose between measurement and calculation of PLD, as shown in the figures. This is mainly attributed to the different source term in the brain between that of real human and that of phantom.

The relationship between the calculated PLD and the brain absorbed dose are shown in **Fig. 6**. The brain absorbed dose can be obtained by multiplying 40 and 53 to the PLD value for the OTOKO and ONAGO phantoms, respectively. Since the calculated PLD doses agree well the measured values, these conversion factors are considered to apply to Japanese generally. These results demonstrate that the brain absorbed dose for FDG PET can be simply evaluated from the PLD value of glabella position.

4. Conclusions

We have developed the reliable evaluation method for the brain absorbed dose in ^{18}F-FDG PET using a Monte Carlo simulation and actual measurement. Regression equations that can estimate the brain absorbed dose from the PLD value of glabella position were obtained. In the near future, we are going to perform dose assessment for other organ in FDG PET. We are also going to apply this method to other positron emitters: ^{11}C, ^{13}N and ^{15}O.

Acknowledgments

The authors would like to thanks Ms. Y. Watanabe of Japan Atomic Energy Agency for her useful comments.

References

1) Deloar HM, Fujiwara T, Shidahara M, et al: Estimation of absorbed dose for 2-[F-18] fluoro-2deoxy-D-glucose using whole-body positron emission tomography and magnetic resonance imaging, Eur J Nucl Med, 25, 565-574 (1998).
2) ICRP: Protection of the Patient in Nuclear Medicine, ICRP Publication 52, Pergamon Press, Oxford, UK (1990).
3) ICRP: Radiation Dose to Patients from Radiopharmaceuticals, ICRP Publication 53, Pergamon Press, Oxford, UK (1988).
4) ICRP: Radiation Dose to Patients from Radiopharmaceuticals, Addendum 2 to ICRP Publication 53, ICRP Publication 80, Pergamon Press, Oxford, UK (1998).
5) W. R. Nelson, H. Hirayama and D. W. O. Rogers: The EGS4 Code System, SLAC-265 (1985).
6) S. Kinase, M. Zankl, J. Kuwabara, K. Sato, H. Noguchi, J. Funabiki and K. Saito: Evaluation of Specific Absorbed Fractions in Voxel Phantoms using Monte Carlo Simulation, Radiat. Prot. Dosim. 105 (1-4), 557-563 (2003).
7) K. Saito, A. Wittmann, S. Koga, Y. Ida, T. Kamei, J. Funabiki and M. Zankl: Construction of a Computed Tomographic Phantom for a Japanese Male Adult and Dose Calculation System, Radiat. Environ. Biophys. 40, 69-76 (2001).
8) A. Endo, Y. Yamaguchi and K. Eckerman: Nuclear Decay Data for Dosimetry Calculation Revised data of ICRP Publication 38, JAERI 1347 (2005).

9) Konopinski, E. J: The Theory of Beta Radioactivity, Oxford Univ. Press, Oxford (1966).
10) RSIC: DLC-136/PHOTX Photon interaction cross section library (contributed by National Institute of Standards and Technology) (1989).
11) ICRU: Stopping powers for electrons and positrons, ICRU Report 37, Bethesda, Md. (1984).
12) E. Niven, M. Thompson, and C. Nahmias: Absorbed dose to adult male and female brain from ^{18}F-fluorodeoxyglucose, Health Phys, 80, 62-66 (2001).

Table1 Characteristics of volunteers and Japanese voxel phantoms

Volunteers and phantoms	Age	Height [cm]	Weight [kg]	Administered activity [MBq]
Male 1	21	182	62	359
Male 2	22	179	75	388
Male 3	23	176	73	371
Female 1	22	153	47	402
Female 2	24	154	54	402
OTOKO	-	170	65	-
ONAGO	-	163	57	-

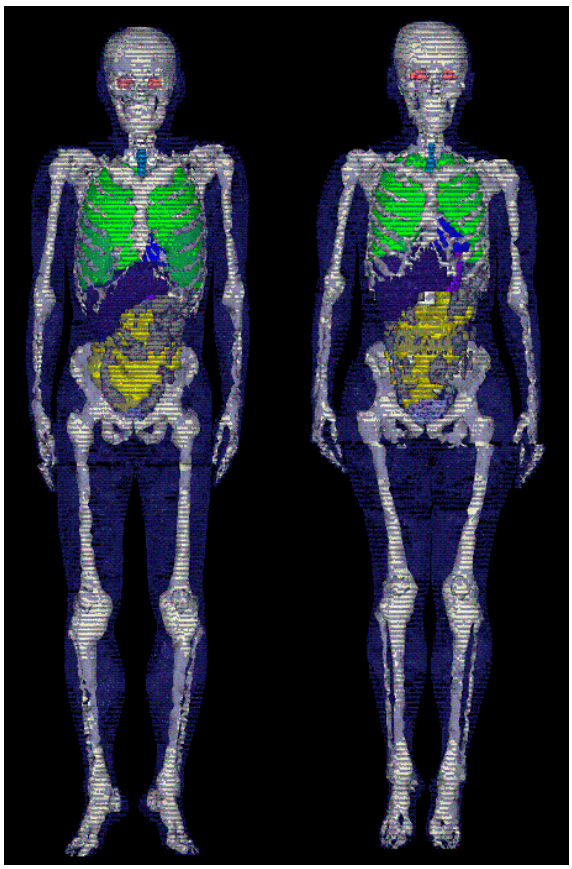

OTOKO ONAGO

Figure 1. Japanese voxel phantoms.

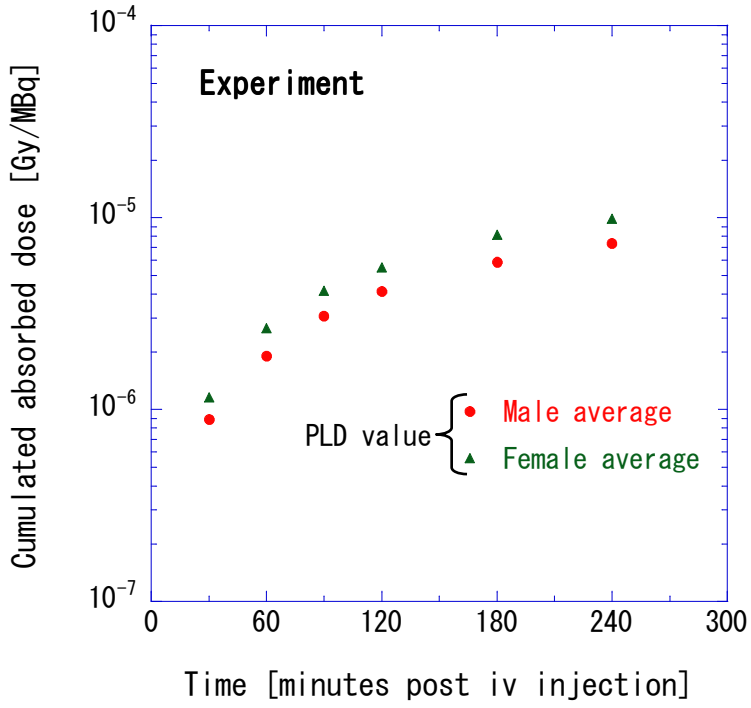

Figure 2. Time-PLD cumulated absorbed dose curve after an intravenous administration of FDG in the experiment.

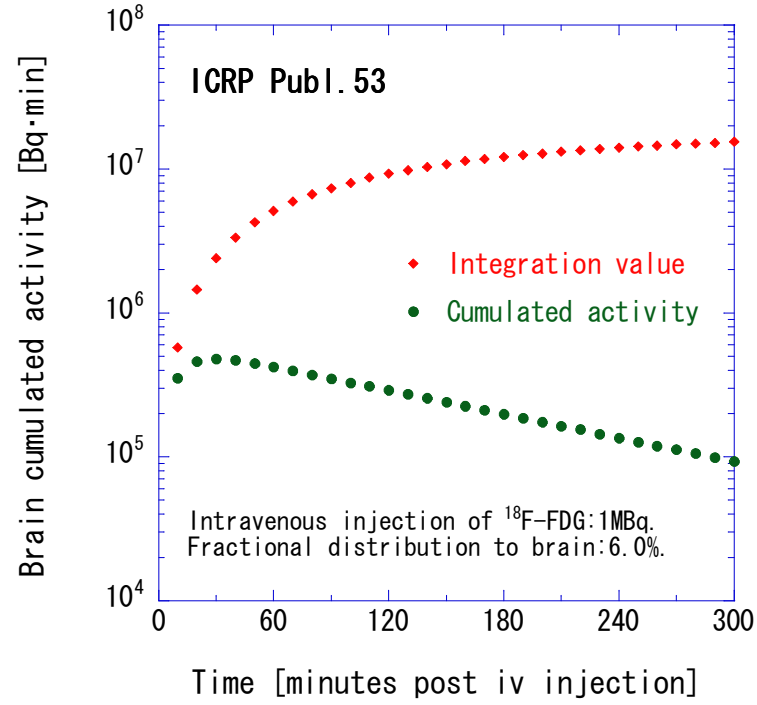

Figure 3. Time-Brain cumulated activity curve after an intravenous administration of FDG.

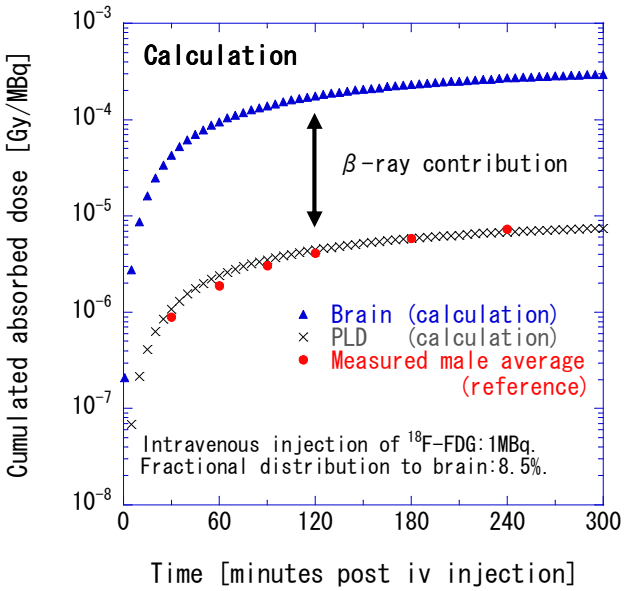

Figure 4. Time-calculated absorbed dose curve for FDG in brain using OTOKO phantom.

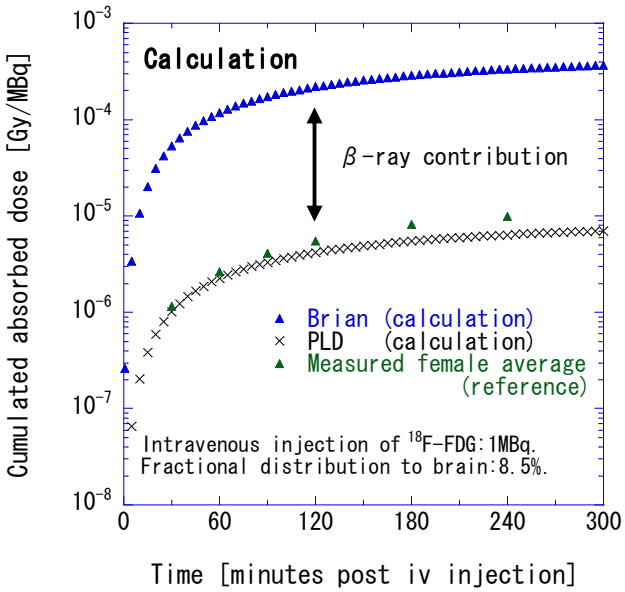

Figure 5. Time-calculated absorbed dose curve for FDG in brain using ONAGO phantom.

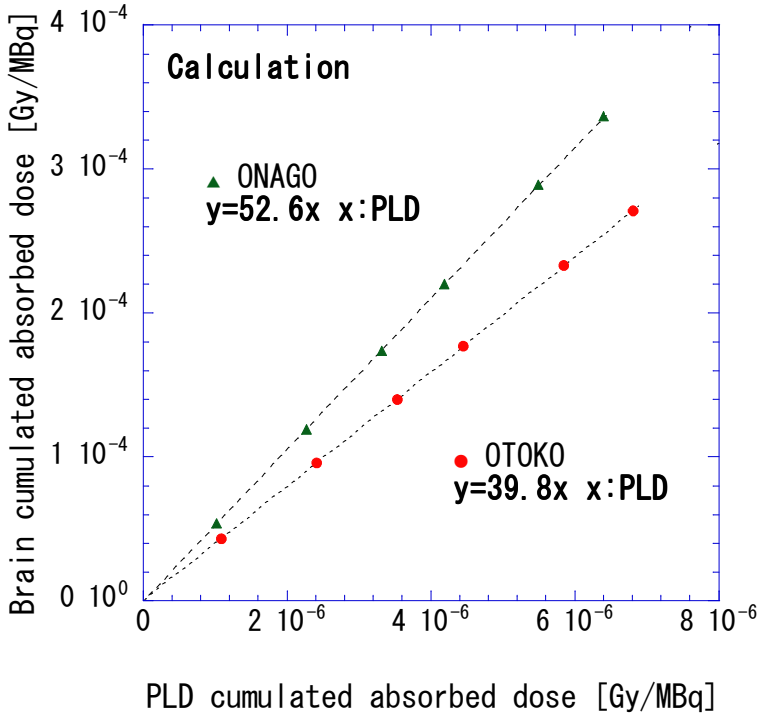

Figure 6. Relationship between calculated PLD absorbed dose and brain absorbed dose.

Estimation of internal dose distribution of ^{90}Y beta-ray source implanted in a small phantom simulated mice

Y. Sato [1], H. Yamabayashi [1], T. Nakamura [1,2]

[1] *Oarai Research Center, Chiyoda Technol Corporation, Oarai-machi, Higashi-ibaraki-gun, Ibarak, 311-1313, Japan*
[2] *Cyclotron and Radioisotope Center, Tohoku University, Aoba, Aramaki, Aoba-ku, Sendai, 980-8578, Japan*

Abstract

The Medical Internal Radiation Dosimetry (MIRD) method assumes that the beta particle energy is absorbed completely in the source organ. However, the organs of mice used in fundamental experiments for internal radiotherapy are relatively small compared to the range of high-energy ^{90}Y beta particles. Therefore, it is well known that the high-energy beta particle can escape the source organ, resulting in large cross-organ doses. The more realistic geometric model such as a voxel-phantom based on Computed Tomography scans for the mouse has been needed for accurately estimating internal doses from administered beta particle emitters. Then it becomes important to simulate the beta particle transport precisely using the Monte Carlo code. The purpose of this study is to validate a user code to simulate the beta particle transport in mice in the Monte Carlo code system (EGS5) by comparing with the absorbed dose measured using a number of small Fluorescent Glass Dosimeters and one capsule of $^{90}YCl_3$ solution (6.6 MBq) implanted in a small phantom (Tough-Water of 30mm x 30mm x 42mm) simulating a simplified form of mice.

It was found that the absorbed dose distribution in this phantom calculated with this user code gave rather good agreement with the measured results.

1. Introduction

Radioimmunotherapy with ^{90}Y-ibritumomab tiuxetan (Zevalin; Biogen Idec Inc., San Diego, CA, and Schering AG, Berlin, Germany), monoclonal antibody conjugated to radioisotopes such as high-energy beta emitters, yttrium-90, has recently been introduced as a therapeutic modality for B-cell non-Hodgkin's lymphoma in the United States and in Europe. Meanwhile, in Japan, it is said to be near production approval of medical supplies by Ministry of Health, Labour and Welfare. For this authorization, it is expected that pre-clinical studies for developing the other radiopharmaceuticals , ^{90}Y-radiolabeled other monoclonal antibodies, thrive more and more to examine the therapeutic efficacy on tumor growth and the radio-toxicity of the drugs with the considerably smaller animals such as mice, in place of the human body.

The Medical Internal Radiation Dosimetry (MIRD) method assumes that the beta particle energy is absorbed completely in the source organ [1]. However, the organs of mice used in fundamental experiments for internal radiotherapy are relatively small compared to the range of high-energy ^{90}Y beta particles, which causes that the high-energy beta particle can escape the source organ, resulting in large cross-organ doses [2] [3]. The more realistic geometric model such as a voxel-phantom based on Computed Tomography scans for the mouse has been needed for accurately estimating internal doses from administered beta particle emitters [4]. Then it becomes important to simulate the beta particle transport in mice precisely using the Monte Carlo code.

The purpose of this study is to validate a user code to simulate the beta particle transport in the Monte Carlo code system (EGS5) [5] in a small phantom simply simulating a mouse by comparing with the measured absorbed dose.

2. Materials and Methods

2.1 Phantom

A small physical phantom simply simulating a mouse was used in this experiment. The phantom is made of Tough Water Phantom produced by Kyoto Kagaku Co., Ltd. consisting of a water equivalent material. The phantom is composed of three blocks (each block of 30 mm x 30 mm x 14 mm), and has a hole in the central area for embedding a cylindrical Tough-Water capsule (outer diameter; 10mm, outer length;16mm, inner diameter; 6mm, inner length;11mm) as shown in Figure 1. The source is $^{90}YCl_3$ solution (267.7 mg) of 6.6 MBq activity. Each phantom block has eight holes for embedding a number of small Fluorescent Glass Dosimeters in the surrounding part of the source region.

2.2 Measurement

The dosimeters used in this experiment are a number of small Radiophotoluminescent Glass Dosimeters (Dose Ace ; GD-302M, Asahi Techno Glass Corporation (ATG)) as shown in Figure 1. These dosimeters are now widely used for measuring patient dose and for radiotherapy planning with phantom irradiated by gamma and X rays. However, they have not been applied for beta-ray dosimetry because it is difficult to measure the absorbed doses separately from beta-rays and bremsstrahlung X-rays in a very small dosimeter. Here in this study, we first tried to measure them using the GD-302M. Those dosimeters were embedded in Tough Water Phantom and then a source capsule was embedded as shown in Figure 2. Those dosimeters were irradiated for four days and the absorbed doses were measured by ATG.

2.3 Calculation with the EGS5 code

The internal dose distribution in this phantom was calculated with the EGS5 code to validate the calculation by comparing with the experiment. In this calculation, the user code must be prepared. A computational geometry simulating this phantom used in the experiment was made by using the Combinatorial Geometry (CG)as shown in Figure 3.

The method how to discriminate beta rays and bremsstrahlung X-rays was examined with the flag set by utilizing variable LATCH included in the EGS5 subroutine "AUSGAB" of our user-code as shown in Figure 4. The Method (A) is that 1000 was added to the LATCH whenever Compton event or photoelectric event or pair production event occurred by the interaction of photons in a matter. The Method (B) is that 1 was added to the LATCH whenever Bremsstrahlung event occurred by the interaction of electrons in a matter.

Method (A)

```
if ((iarg.eq.15).or.(iarg.eq.17).or.(iarg.eq.19)) then
    latch(np)=latch(np) +1000
    return
end if
```

Method (B)

```
If (iarg.eq.7) then
    If (iq(np).eq.0) then
        latch(np) =latch(np) + 1
    else if (iq(np-1).eq.0) then
        latch(np-1) = latch(np-1) +1
    end if
    return
end if
```

The energy of the transported particle was absorbed as photon in the region of interest if the value of LATCH was assumed to be equal to 1000 or greater than 1000 in the method (A) (equal to 1 or greater than 1 in the method (B)), and the energy of the transported particle was assumed to be absorbed as beta ray in the region of interest if the value of LATCH was equal to zero.

```
if (irl.ge.1.and.irl.le.nreg-1) then
    idet=irl
    if ((idet.ge.1).and.(idet.le.ndet)) then
        depe (idet) = depe (idet) + edepwt
        if (latch(np).eq.0) then
            eede(idet)=eede(idet)+ edepwt        !  As  Electrons
        else if (latch(np).ge.1000) then         !    In the case of method (A)
```

```
(       else if (latch(np).ge.1) then                    !  In the case of method (B)    )
                epde (idet)=epde (idet)+ edepwt          !  As  Photons
            end if
        end if
    end if
```

Information obtained for each step of the interaction of beta-ray in matter with the use of subroutine SWATCH was utilized to discriminate the beta-ray event and bremsstrahlung X-ray event. As the result, Figure 4 shows that the flag of a bremsstrahlung interaction (iarg=7) should be set by the Method (B) and the EGS5 Monte Carlo calculation is proceeded afterward by utilizing the Method (B).

3. Results and Discussions

Figure 5 shows the absorbed doses in mGy per Bq of ^{90}Y measured with GD-302M glass dosimeters by comparing with the EGS5 calculation. The comparison is divided into three parts corresponding to three blocks, Blocks 1 to 3, shown in Figure 2. It is clearly found from Figure 8 that the calculated values are in good agreement with the measured values at No.1 position of Block 1 and 3, and rather good agreement at No.1 of Block 2 where are close to the source capsule, but with increasing the distance from the source, the calculated values become more overestimated especially about three times at Nos. 5 to 8 at the corner of the phantom. It is considered that this discrepancy partly may come from the energy dependence of dose response of GD-302M to beta rays and photons, and partly from the inadequate simulation of the internal dose estimation. The energy dependence of dose response of GD-302M to beta rays and photons is therefore shown in Figures 6 and 7, respectively. Considering this energy dependence, the EGS5 calculated results of photon and beta-ray energy spectra crossing the dosimeter area are exemplified at (a) No.1 of Block 2 and (b) at No. 5 of Block 2 indicated in Figure 2, respectively, in Figure 8 (a) and (b). The similar spectra are obtained at other positions. Comparing Figure 6 and 7 with Figure 8, the dose response of GD-302M to beta-ray energy is almost constant in the energy spectrum of Figure 8, but the dose response of GD-302M to photons steeply increases below 200 keV where is the dominant part of the energy spectrum of Figure 8. This means that the correction of dose response of GD-302M to photon energy is essentially important to get more accurate dose value. It may be concluded that the measured doses at the positions close to the source where the beta-ray doses occupy dominant values could give good agreement to the calculated doses. It is also necessary to improve the simulation method for beta-ray and photon transport in small phantom.

4. Conclusions

In this study, we measured the internal dose distribution of ^{90}Y-labelled source in Tough water phantom simulating a mouse with small glass dosimeters. The measured absorbed doses were compared with the simulated results with the EGS5 code. In this simulation, we developed the method to discriminate beta-ray events and bremsstrahlung photon events considering the beta particle transport in small phantom. Rather good agreement between measurement and calculation could be obtained at the positions close to the source, but large discrepancy at the positions away from the source. We have started to improve this discrepancy in the simulation..

Acknowledgments

The authors would like to thank Dr. H. Hirayama and Dr. Y. Namito for their very helpful comments and discussions.

This study was supported by Asahi Techno Glass Corporation and Chiyoda Technol Corporation. The authors would like to thank Mr. T. Ikegami and Mr. H. Mori for measurement of RPD and to thank Mr.

Kawauchi, Mr. Mikami and Mr. Yoneda for the preparation of a source-capsule.

References

1) R. Loevinger, M. Berman, "A schema for absorbed-dose calculations for biologically-distributed radionuclides," New York: Society of Nuclear Medicine, MIRD pamphlet No. 1, 1968.
2) T. E. Hui, D. R. Fisher, J. A. Kuhn, L. E. Williams, C. Nourigat, C. C. Bbadger, B. G. Beatty and J. D. Beatty, "A mouse model for calculating cross-organ beta-doses from yttrium-90-labeled immunoconjugates," Cancer 73, 951-957 (1994).
3) A. A. Flynn, A. J. Green, R. B. Pedly, G. M. Boxer, R. Boden and R. H. J. Begent, "A Mouse Model for Calculating the Absorbed Beta-Particle Dose from ^{131}I- and ^{90}Y-Labeled Immunoconjugates, Including a Method for Dealing with Heterogeneity in Kidney and Tumor, " Radiation Research 156, 28-35 (2001).
4) M. G. Stabin, T. E. Peterson, G. E. Holburn and M. A. Emmons, "Voxel-Based Mouse and Rat Models for Internal Dose Calculation," J Nucl Med. 47, 655-659 (2006).
5) H. Hirayama, Y. Namito, A.F. Bielajew, S.J. Wilderman and W.R. Nelson, "The EGS5 Code System," SLAC-R-730 (2005) and KEK Report 2005-8 (2005).

(a) Three small physical phantom blocks made of Tough Water

(b) Laminated phantom simulating a mouse

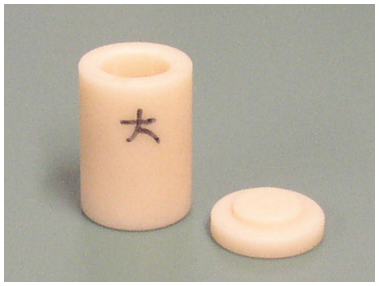

(c) Source capsule inserting $^{90}YCl_3$ solution

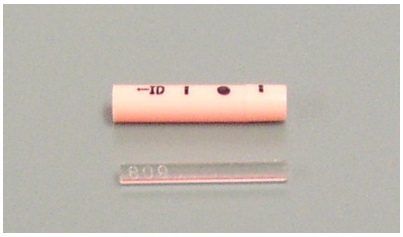

(d) Glass dosimeter, GD-302M

Figure 1. Photographs of phantom blocks, phantom simulating a mouse, source capsule and GD-302M glass dosimeter

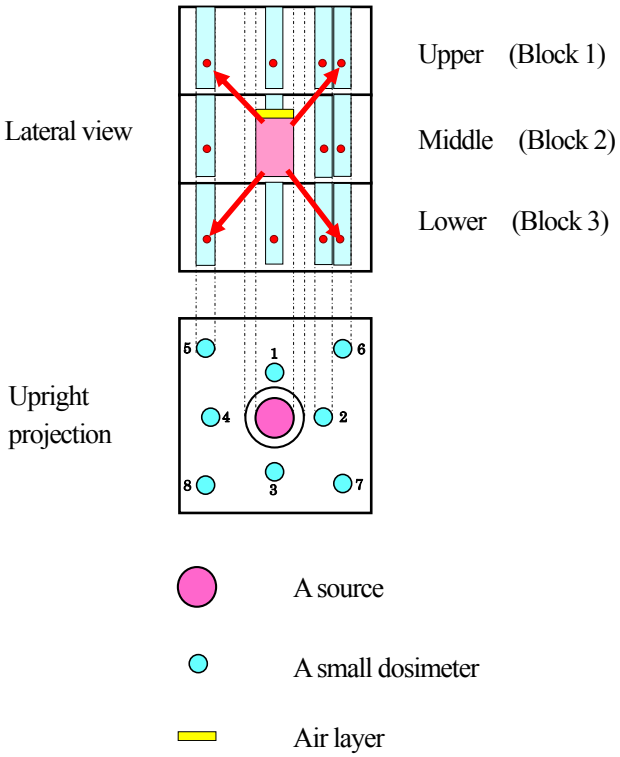

Figure 2. Geometrical configuration of dosimeters and a source

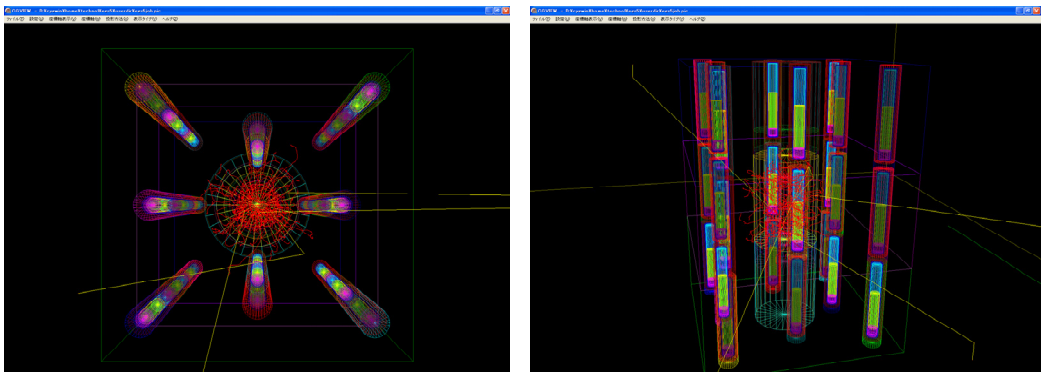

Figure 3. Geometry for the calculation

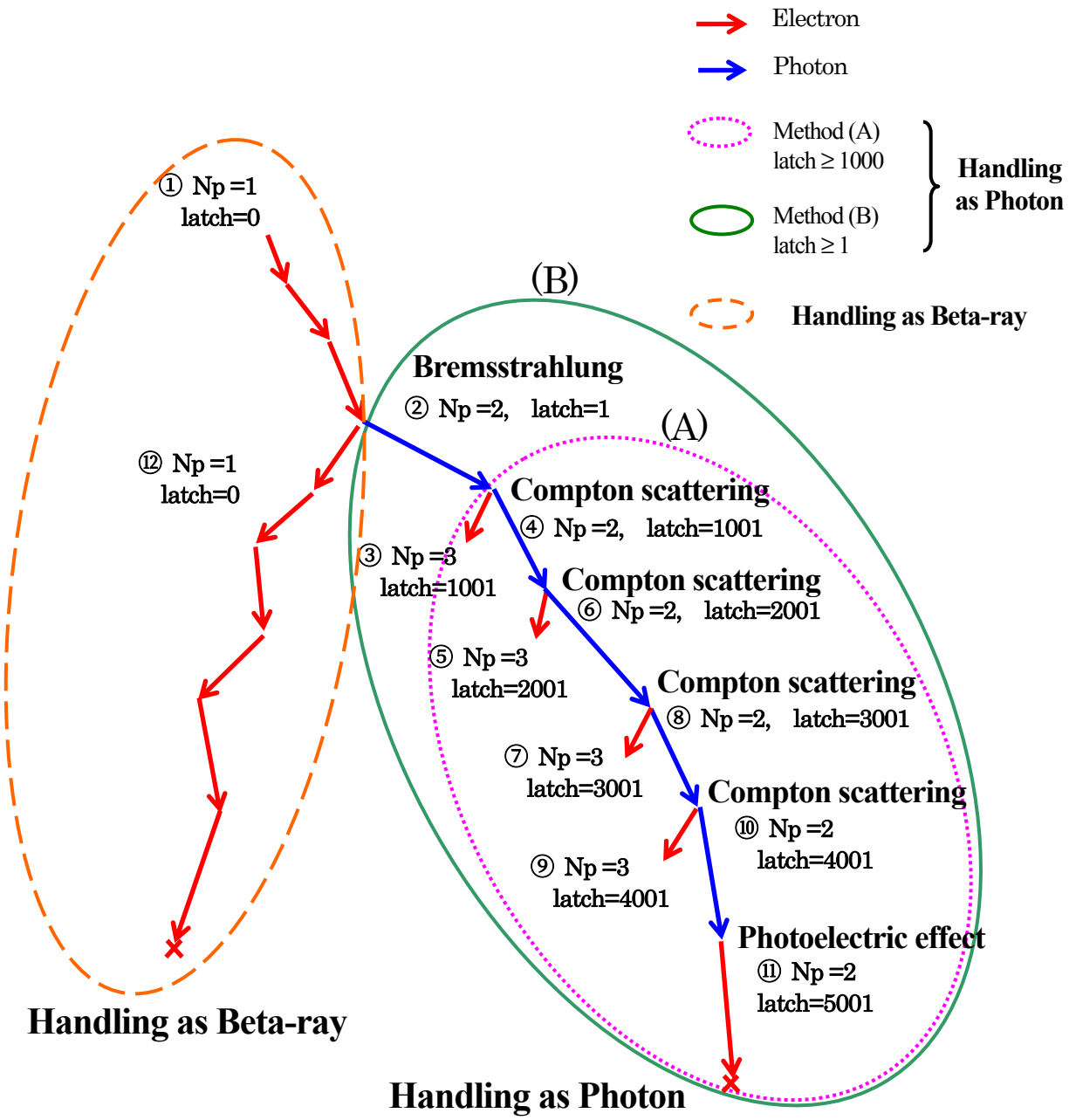

Figure 4. The schematic diagram of ray tracing method to discriminate beta-ray and bremsstrahlung X-ray events

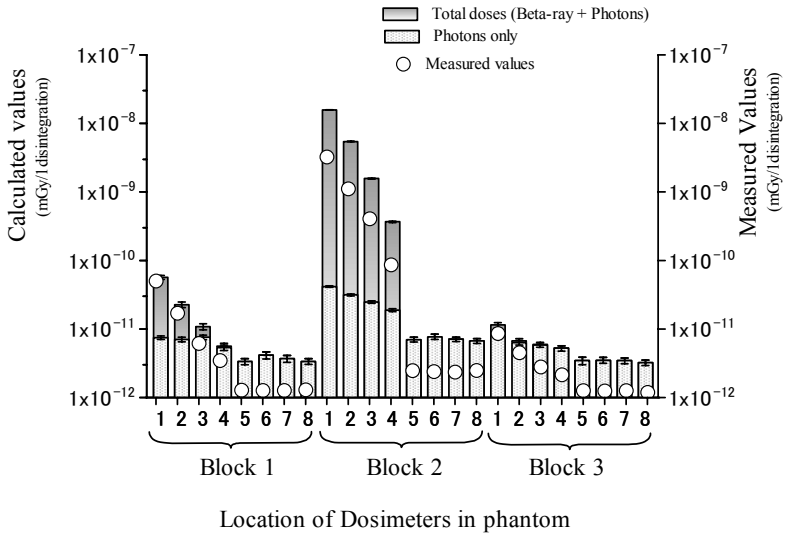

Figure 5. Comparison of calculated and measured values of absorbed doses at various positions of GD-302M dosimeters

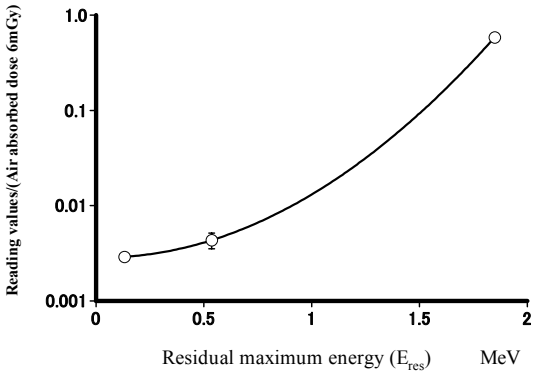

Figure 6. Energy dependence of GD-302M dose response to beta rays as a function of residual maximum energy

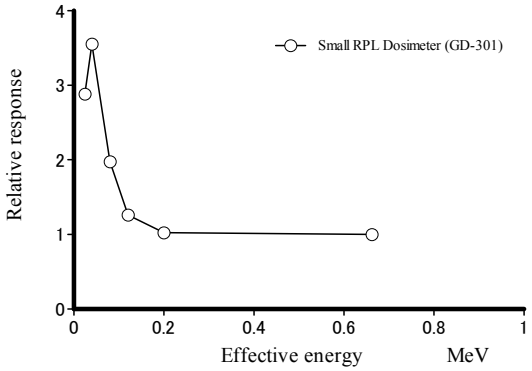

Figure 7. Energy dependence of GD-302M dose response to photons normalized at ^{137}Cs 662 keV photons

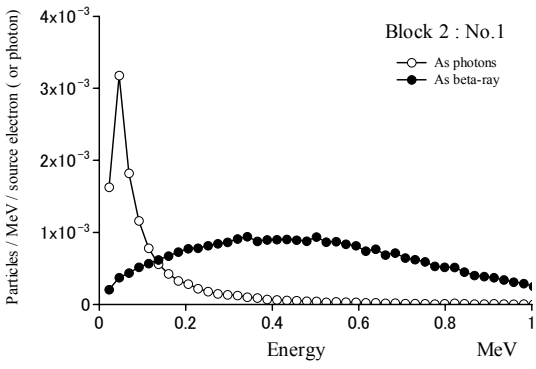

(a) at No.1 of Block 2

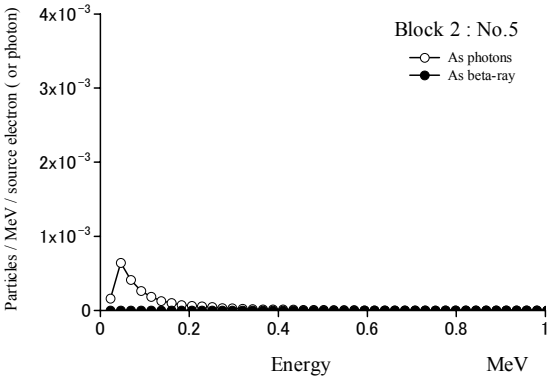

(b) at No. 5 of Block 2

Figure 8. Photon and beta-ray energy spectra crossing the dosimeter area at (a) No.1 of Block 2 and (b) at No. 5 of Block 2 indicated in Fig. 2, respectively. Photon spectra are shown in white circles and beta-ray spectra in black circles

EVALUATION OF EXTERNAL RADIATION EXPOSURE OF HUMAN INVOLVED IN EQUINE BONE SCINTIGRAPHY

K. Oono[1], M. Fujii[1], T. Sano[1], Y. Namito[2], H. Hirayama[2], N. Ito[1]

1 School of Veterinary Medicine, Kitasato University,
Higashi,23-35-1,Towada, Aomori,034-8628,Japan
2 High Energy Accelerator Research Organization,
Tsukuba, Ibaraki,305-0801,Japan

Abstract

The purpose of this study is to obtain the basic data for radiation safety in the veterinary nuclear medicine. Therefore, human external radiation dose in equine bone scintigraphy was evaluated by using EGS4. Using CGview, we made mathematical phantoms of a horse and an injection syringe to use for Radiation control. The horse mathematical phantom have heart, liver, kidney, bladder, lungs, muscle, bone, soft tissue, and fat. The phantom radiation detectors were set up in a position of 0m, 0.5m, 1m and 2m from surface of the body. The detector area was assumed to be air. An effective dose was calculated using a conversion factor by the energy and the fluence of the photon which pass through a detector.

The radiation exposures of the veterinarian and the stableman were calculated by setting the distance from horse body surface, and the duration of examination as parameters. The exposed dose of the general public was calculated by assumption that a public would keep standing for a long time till extinction of radioactivity at one meter from body surface of a horse. Consequently, radiation exposure of general public is overevaluated.

The overestimate radiation exposure of the veterinarian was 16.8 micro Sv, and similarly the exposure of the stableman was 93.6 micro Sv. The exposure of the stableman who would be nearer to a horse grew bigger than a veterinarian. Therefore, the educational training for shortening of working duration and taking distance from a horse is important to reduce radiation exposure. The dose rate after 24 hrs of administering at 1m from the body surface of a horse was 0.86μSv/hr, and that after 48 hours of administering was 0.05μSv/h. The accumulation dose of the general public from a horse when the horse was released in 24 hours of the radiopharmaceutical administering was estimated 4.8 μ Sv.

1. Introduction

Now the equine bone scintigraphy using ^{99m}Tc is carried out in Europe, USA and some Asian countries. If a horse showed minor claudication. it is difficult to be settled in causal locus by only using X-ray examination and echography. In addition, examinations of CT and MRI are difficult because of the size of a horse. In general, bone scintigraphy is extremely useful procedure for a horse, because the examination can be carried out simply without anesthetization. However, equine bone scintigraphy is not carried out because the legal specification of radiopharmaceutical use for animals is not enough in Japan now. Therefore a guideline including usage of radiopharmaceutical and leaving basis of horses after radiopharmaceutical administration must be made to do equine bone scintigraphy in the near future in Japan. We require the data relating to exposure dose of the persons concerned with equine bone scintigraphy, so we lack the data. Consequently human external exposure dosage to be concerned with equine bone scintigraphy was evaluated by using EGS4 for the purpose of getting a database of the safe use of radiopharmaceutical in veterinary nuclear medicine.

2. Materials and Methods

Mathematical equine phantom was made by using CGview. (Fig.1) Mean of 16 head of 4 years old thoroughbred horses was used for the size of the phantom. [5] The position and the weight of organs were quoted from a book of anatomy. [2] Elemental composition and density of each internal organ were based on the documents about human data. [1] The nine kinds of organs and tissues – heart, liver, kidney, bladder, lungs, muscle, bone, soft tissue and fat – were considered for this calculation.

Next, we made mathematical phantom of an injection syringe to use for administration of radiopharmaceutical. It was assumed that the capacity of the syringe was 10ml.Outside of the tube was made by polypropylene and inside of the tube was made by polyethylene. The syringe circumference was covered in lead of 1.5mm.

The detectors were installed in the position of 0m, 0.5m, 1m and 2m from the body surface of the horse. (Fig.2) The area of detectors assumed it air. An effective dose was calculated using a conversion factor by the energy and the fluence of the photon which passed a detector.

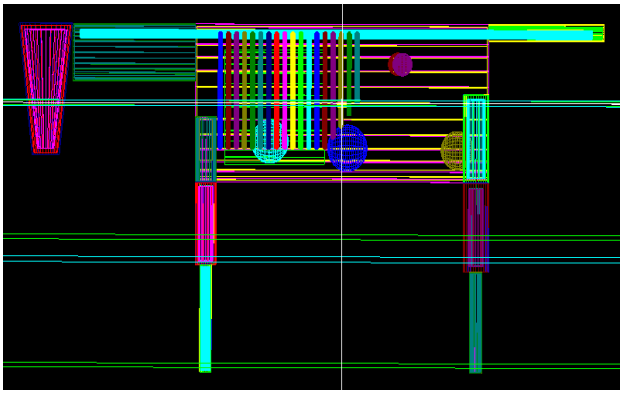

Fig.1 Equine mathematical phantom

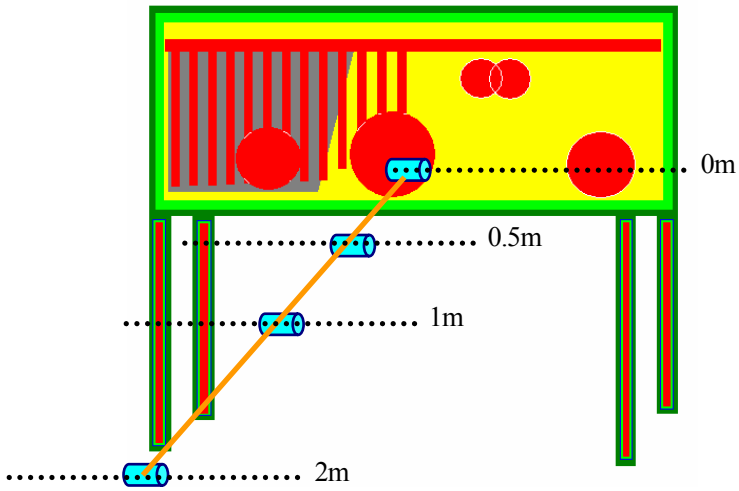

Fig.2 Locations of the detectors from the phantom surface

The dosage of ^{99m}Tc assumed it 5.1GBq. This is maximal quantity among quantity used at Tennessee University. It was supposed that the administered RI was distributed over a whole body through a blood vessel equally just after administration. At 2 hours after administration, it was supposed to distribute according to the following list (Table.1). After the two hours next, it was assumed to attenuate followed by physical half life without excretion and redistribution. This distribution data was based on the data of the distribution of rats which were administrated ^{99m}Tc-MDP.

Table.1 The distribution of ^{99m}Tc at 2 hours after administration (%)

liver	0.29	right forearm	0.68
right kidney	0.35	right armend	0.67
left kidney	0.35	left femoris	1.62
bladder	38.8	left cruris	0.75
spine	4.15	left footend	0.94
left humerus	1.35	right femoris	1.62
left forearm	0.68	right cruris	0.75
left armend	0.67	right footend	0.94
right humerus	1.35	others	44.1

It was assumed that the veterinarian worked at the position of 0.4m from the injection syringe in the first 2 minutes, at 1m or 2m from a horse in the next 20 minutes and for 1 hour from 2 hours to 3hours after administration. It was assumed that the stableman worked at the position of 1m from the injection syringe in the first 2 minutes, at 0m, 0.5m or 1m from a horse in the next 20 minutes and for 1 hour from 2 hours to 3hours after administration. About the general public, radiation exposure from a horse after the release was assumed, and dose rate in a position of 1m from a horse was calculated. Furthermore, accumulated exposure dose was estimated at a position of 1m from a horse till all inner radioactivity was decayed after release of a horse.

3. Results and Discussion

3.1 Veterinarian

An exposure dose of the veterinarian was 16.8μSv at 1m from a horse and 6.2μSv at 2m. (Tabie.2)

Table.2 An exposure dose of the veterinarian (μSv)

	1m	2m
first 2 minutes	0.28	0.28
next 20 minutes	6.23	2.09
2 hours post	10.25	3.29
total	16.8	6.24

3.2 Stableman

An exposure dose of the stableman was 93.6μSv at 0m from a horse, 31.9μSv at 0.5m and 16.5μSv at 1m. (Tabie.3) An exposure dose of the stableman who was at a near position by a horse grew bigger than that of the veterinarian.

Table.3 An exposure dose of the stableman (μSv)

	0m	0.5m	1m
first 2 minutes	0.04	0.04	0.04
next 20 minutes	45.1	13.0	6.23
2 hours post	48.4	18.9	10.3
total	93.6	31.9	16.5

3.3 General publics

Fig.3 and Fig.4 show the dose rate at the position of 1m from the surface of a horse which requested to estimate the radiation exposure of general publics. The dose rate after RI administration 48 hours was 0.05μSv /h. This is an approximately equal value of background (B.G.) (0.64mSv/year = 0.07μSv/h). [4] Dose rate after administration 24 hours was 0.86μSv/h, and this was about 12 times of B.G. In addition, the integrating exposure dose was 4.8μSv released 24 hours after administration and 0.30μSv released 48 hours after administration.

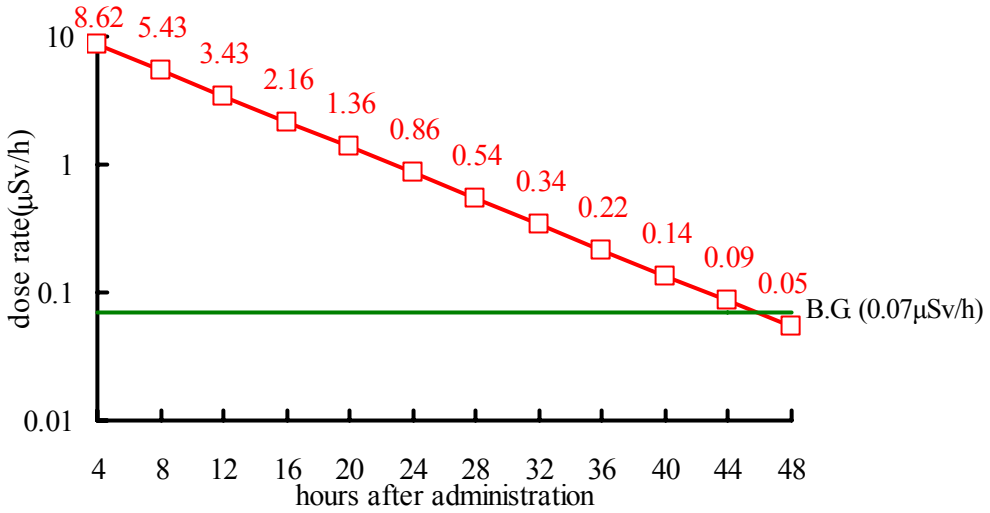

Fig.3 Dose rate (μSv/h) at 1m from the surface of the phantom

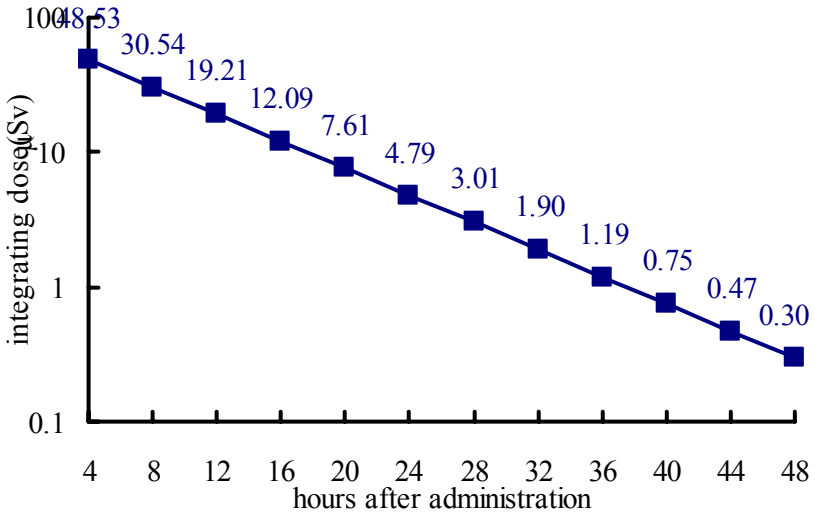

Fig.4 Integrating dose (μSv) at 1m from the surface of the phantom

4. Conclusions

This study shows that the dose per one examination of a practitioner was at most 16.8 Sv of the veterinarian and 93.6 Sv of the stableman. They were very low values. However, exposed dose of the stableman who is at the position that is nearer to a horse grows higher than the veterinarian by all means. Therefore a human concerned with examinations requires wearing the protection clothes, taking distance from a horse as much as possible and shortening working time. Enough educational training is effective to exposed dose reduction. As a result, radiation exposure of the person concerned is reduced, and the person concerned can carry out bone scintigraphy safely.

We calculated in the requirements that did not wear protection clothes this time. However, it is known that wearing of protection clothes reduces radiation exposure from a quarter to around a one-third. [3]

the accumulated dose of a public was 0.30 μ Sv after release of 48 hrs after administration. Both became very small values. Therefore, it is supposed that risk of exposure of general public is very low if we discharge a horse from hospital at 2 days after radiopharmaceutical administration.

Acknowledgments

This work was supported by High Energy Accelerator Research Organization. And numerous advices are gratefully acknowledged.

References

1) ICRU Report 46, Photon, Electron, Proton and Neutron Interaction Data for Body tissues.
2) JRA Equine Research Institute, 1996, "The book of medical science of horses", pp.90-92, JRA, Tokyo
3) P. F. Steyn, J. Uhrig, "The role of protective lead clothing in reducing radiation exposure rates to personnel during equine bone scintigraphy", Vet Radiol Ultrasound, 46(6), 529-532 (2005).
4) S. Abe, 1989, Natural radiation exposure in Japan, National Institute of Radiological Sciences
5) Y. Nagata, "Development and nutrition of racing horses", pp.166-174, Japan Racing Association PR center, Tokyo (1999).

Photoneutron Yield in Steel Shield by Electron Beam from Medical Linear Accelerator

Yukio Fujita, Hidetoshi Saitoh and Atsushi Myojoyama

Graduate School of Health Sciences, Tokyo Metropolitan University

Abstract

In recent years, many medical linear accelerators do not equip a beam stopper and such linacs generate not only high energy photons but high energy electrons. Therefore, there is possibility of shield necessity against bremsstrahlen and photoneutron generated by high energy electron beam. However, there are a few physical data or no recommendation. In this report, yield efficiency and leakage dose of bremsstrahlen and photoneutron was calculated using EGS Monte Carlo simulations. Then, to verify result by calculation, leakage dose by photoneutron was measured with a rem counter. The result clearly shows that leakage dose of bremsstrahlen and photoneutron generated by 15 MeV electron beam is negligible.

1. Introduction

When the old 6 MV linac equipped with a beam stopper would be replaced, we settled to install the new linac system which generates 6 MV photons and 15 MeV maximum electrons and does not equip beam stopper. Therefore, redesign to reinforce the shield was required. A radiation shield of linac room has been designed in accordance with the "Manual of Practical Shield Calculation of Radiation Facilities (2000)" (calculation manual) [1] in Japan. According to the "calculation manual", first shield plan was designed by means of adding steel boards to the inside wall and ceiling of the room. However, a government official of the competent authorities pointed out the necessity to shield against bremsstrahlung and photoneutrons from the steel boards by the 15 MeV electron beam. The shield plan was immediately changed to add 8 cm plasterboard in front of the steel board without any claim since we had no physical data for counterargument and worried delay of construction and contract.

The aim of this report is to clarify yield efficiency and dose leakage of bremsstrahlung and photoneutrons from steel board impinged by high energy electron beam for radiotherapy since the

"calculation manual" does not expound to that. And the plasterboard as a countermeasure for that problem was validated.

2. Methods and Materials

Fig. 1 shows the final design of the linac room. A steel board, instead of the beam stopper, was added to reinforce shield, and a thickness of 8 cm plaster boards was placed in front of the steel board to reduce bremsstrahlen from the steel boards. After this, simulation geometries were modeled after this shield design.

2.1 Leakage dose of bremsstrahlung

First of all, dose leakage of bremsstrahlung was calculated by EGS Monte Carlo simulation. Fig. 2 shows the simulation geometry which was simplified Fig. 1 of actual design to calculate energy spectrum and fluence of the bremsstrahlung. Simulations were performed with next two models, there is steel board in front of concrete wall and plasterboard layer was placed in front of the aforementioned geometry. Incident electron energy was assumed to be monoenergy of 12 MeV and 15 MeV. Table 1 shows the condition of simulation. Table 2 shows composition of the shielding materials for PEGS cross section data calculation. The BEAMnrc code [2] was used in this simulation.

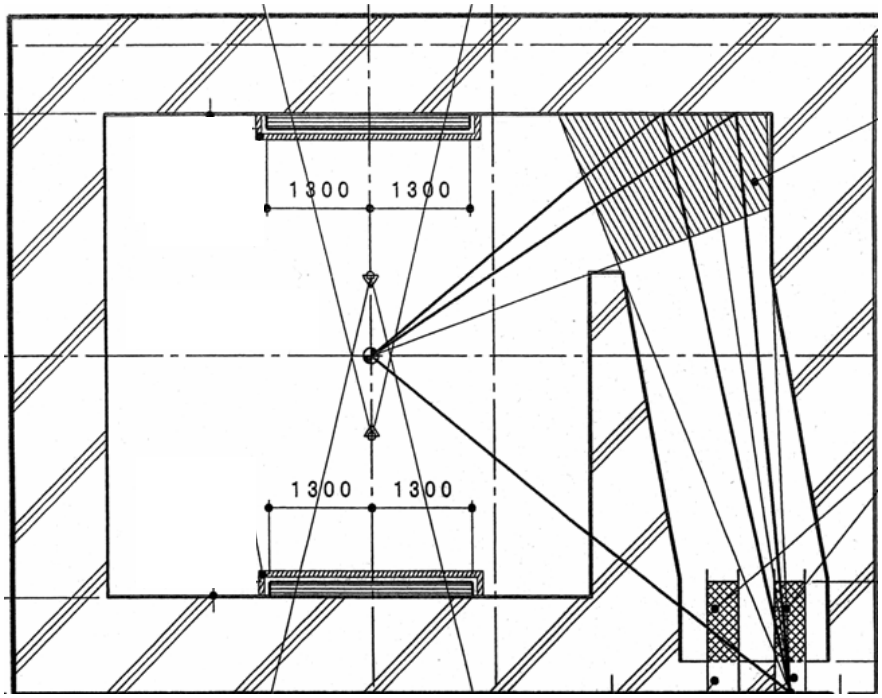

Fig. 1 Shield design of the linac room

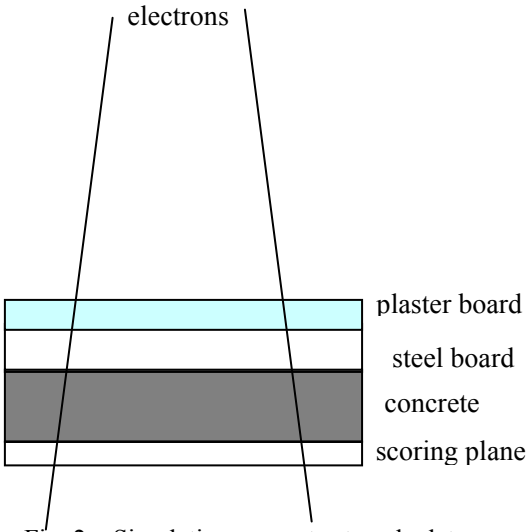

Fig. 2 Simulation geometry to calculate energy fluence distribution of the bremsstrahlung which passed through the shielding wall.

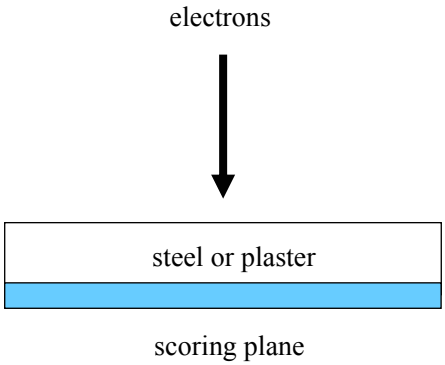

Fig. 3 Simulation geometry to calculate bremsstrahlung which contribute to photo-nuclear reaction.

Table 1 Simulation conditions for leakage dose calculation of bremsstrahlung

Incident particles	electrons
Energy of beam [MeV]	12 or 15 (monoenergy)
Number of histories	1×10^8

Table 2 Composition of shielding material for PEGS calculation

	Fe	Plasterboard	Concrete
density	7.87	1.20	2.10
[g/cm^3]	weight per cent	weight per cent	weight per cent
H		0.0234	0.0103
C			0.0010
O		0.5575	0.5446
Mg			0.0022
Al			0.0348
Si			0.3460
S		0.1863	
Ca		0.2328	0.0446
Fe	1.0		0.0143

Electron fluence rate ϕ_{elec} at isocenter at the maximum dose rate was calculated with next equation.

$$\phi_{elec} = \dot{D}_{water} \frac{\rho}{S_{col}} \quad (1)$$

where, D_{water} is maximum absorbed dose rate of water and S_{col}/ρ is collision stopping power for the water[3]. And collision kerma rate K_{col} which may leak from the shielding wall was given by next;

$$\dot{K}_{col} = \phi_{elec} \left(\frac{d_{IC}}{d_{wall}} \right)^2 \int \frac{\mu_{en}(E)}{\rho} \Psi(E) \, dE \quad (2)$$

where, d_{IC} is a source to isocenter distance and d_{wall} is source to wall distance, $\Psi(E)$ is the energy fluence at energy E per incident electron, $\mu_{en}(E)/\rho$ is mass energy absorption coefficient at energy E for the water [4].

2.2 Leakage dose of photoneutron

Table 3 shows photonuclear reaction threshold energy of several materials [5]. According to table 3, photonuclear reaction can take place in only iron by 15 MeV electron - brensstrahlung. The EGS code unfortunately is impossible to simulate photo-nuclear interaction. Therefore, leakage dose of photoneutron was determined by next phased procedure.

The energy fluence distribution of the bremsstrahlen which contribute to photonuclear reaction (photons above 11.2 MeV) was simulated with the geometry as shown in Fig. 3.

Table 3 Threshold energy of photonuclear reaction (IAEA Photonuclear Data Library [5])

Material	Threshold Energy [MeV]
C	18.72
O	15.66
Mg	16.53
Al	13.06
Si	17.18
S	15.04
Ca	15.64
Fe	11.20

The number of interaction Φ is given by;

$$\Phi = \Phi_0 \left\{1 - e^{-(\mu/\rho)}\right\} \tag{3}$$

where Φ_0 is primary photon fluence, μ/ρ is total mass attenuation coefficient. The μ/ρ data by J.H. Hubbell and S.M. Seltzer [4] contain photonuclear reaction $\sigma_{\text{ph.n.}}$. Therefore the number of photoneutron $\Phi_{\text{ph.n.}}$ can be given by;

$$\Phi_{\text{ph.n.}} = \Phi_0 \left\{1 - e^{-(\mu/\rho)}\right\} \frac{\sigma_{\text{ph.n.}}}{\sigma_{\text{tot}}} \tag{4}$$

where σ_{tot} is total cross section. And energy of the photoneutron generated by the photo-nuclear reaction is given by;

$$E_{\text{n}}(\theta) = \frac{M(E_\gamma + Q)}{m + M} + \frac{E_\gamma \left[(2mM)(m + M)(E_\gamma + Q)\right]^{1/2}}{(m + M)^2} \cos\theta \tag{5}$$

where, θ is angle between primary photon to recoil neutron direction, E_γ is photon energy (assumed << 931 MeV), M and m is the rest mass of recoil nucleus and neutron in MeV.

Finally, photoneutron kerma rate K was calculated by the following equation;

$$\dot{K} = \int \Phi_{\text{ph.n.}}(E)\, k_{\text{f}}(E)\, F_{\text{n}}(E)\, \mathrm{d}E \tag{6}$$

where, k_{f} is kerma factor which is given by ICRU report 26 [6] and F_{n} is effective dose transmission coefficient.

2.3 Measurement of leakage dose

To verify result by calculation, leakage dose by neutron was measured with rem counter (2202D, ALONOR) when a shield wall was irradiated with 15 MeV electron beam at maximum dose rate.

3. Results

3.1 Leakage dose of bremsstrahlung

Fig. 4 shows energy fluence distribution of the bremsstrahlen which passed through a shield wall by electron beam irradiation. Table 4 shows the air collision kerma rate of bremsstrahlen that calculated from the energy fluence distribution as shown in Fig. 4 and equation (1) and (2). The air collision kerma rate decreased to about a half by using plasterboard.

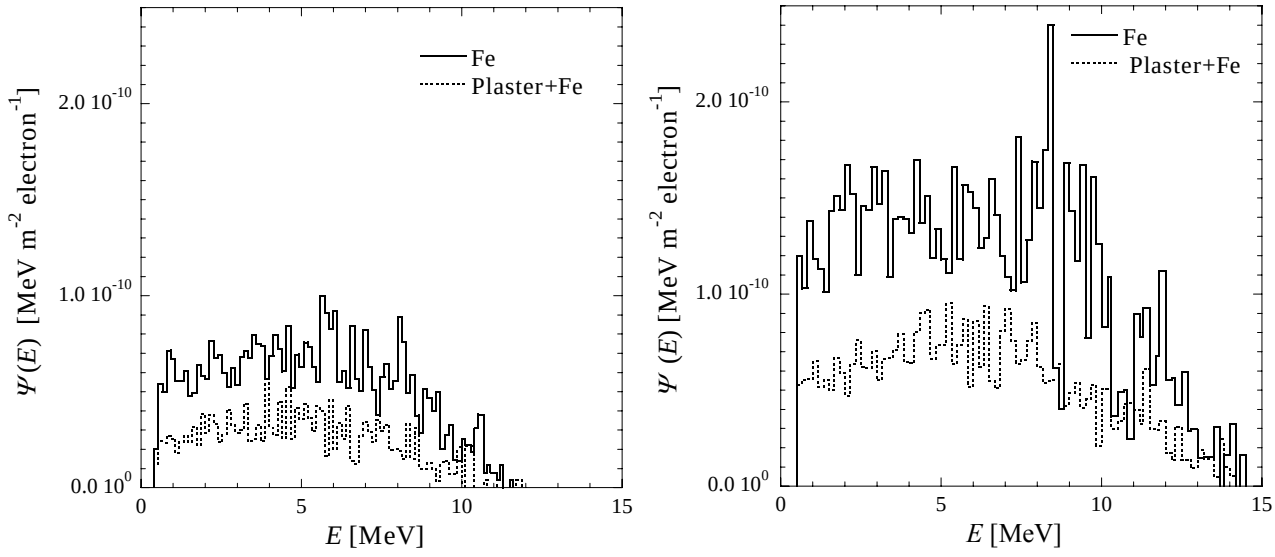

(a) 12MeV (b) 15MeV

Fig. 4 Energy fluence distribution of bremsstrahlen which passed through a shield wall

Table 4 Air collision kerma rate of bremsstrahlen

Energy [MeV]	Fe [Gy min^{-1}]	Plaster + Fe [Gy min^{-1}]
12	3.80×10^{-8}	1.72×10^{-8}
15	6.71×10^{-8}	3.18×10^{-8}

3.2 Leakage dose of photoneutron

Fig. 5 shows energy fluence distribution of the bremsstrahlen which were generated and pass through steel boards. Table 5 shows leakage dose of photoneutron that calculated from energy fluence shown in Fig. 4 and equation (4), (5) and (6). From table 5, the leakage dose of a photoneutron decreased to about a half in 15 MeV and to about a one-tenth in 12 MeV.

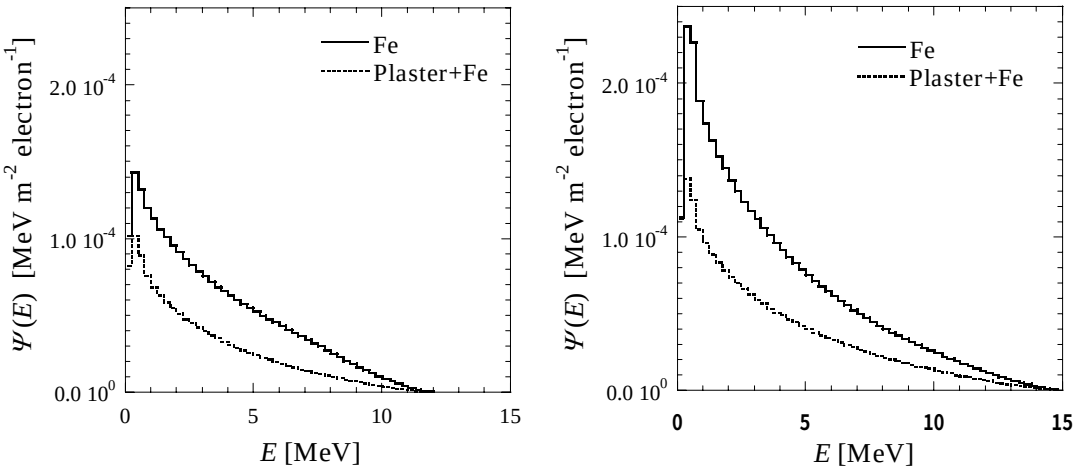

(a) 12MeV (b) 15MeV

Fig. 5 Energy fluence distribution of the bremsstrahlen which pass through steel boards

Table 5 Leakage dose rate of photoneutron

Energy [MeV]	Fe [Gy min^{-1}]	Plaster + Fe [Gy min^{-1}]
12	1.13×10^{-21}	1.06×10^{-22}
15	8.54×10^{-16}	3.91×10^{-16}

3.3 Comparison between measured and calculated leakage dose

Table 6 shows calculated and measured leakage dose which was due to bremsstrahlung and photoneutron. The calculated dose was quite less than the range of rem counter, from 1 μSv/h to 100 mSv/h and leakage dose of photoneutron and bremsstrahlung was not detected as expected.

Table 6 Comparison between calculated and measured leakage dose

	Electron Energy [MeV]	Fe [Sv h^{-1}]	Plaster + Fe [Sv h^{-1}]
bremsstrahlen (calculated)	12	2.28×10^{-3}	1.03×10^{-3}
	15	4.03×10^{-3}	1.91×10^{-3}
photoneutron (calculated)	12	1.35×10^{-12}	1.26×10^{-13}
	15	1.03×10^{-6}	4.70×10^{-7}
measured	12		not detected
	15		not detected

Table 7 Leakage dose per 3 months

Energy [MeV]	Fe [mSv / 3 months]	Plaster + Fe [mSv / 3 months]
12	3.79×10^{-2}	1.72×10^{-2}
15	6.71×10^{-2}	3.18×10^{-2}

4. Discussion

The dose limit of controlled area is 1.3 mSv per each 3 months in Japanese regulation. Table 7 shows the calculated results of leakage dose per 3 months for our institution. According to the table 7, it is obvious that the leakage dose was quite less than the dose limit for restricted area in all conditions whether plaster boards were placed in front of steel board or not. And it is confirmed by actual measurement using rem counter.

5. Conclusions

To clarify yield efficiency and dose leakage of bremsstrahlung and photoneutrons from steel board impinged by high energy electron beam for radiotherapy, leakage dose calculation was done using EGS Monte Carlo simulation and theoretical calculation.

When shield reinforcement were required by removing a beam stopper and electron energy is up to 15 MeV, it is adequate that shield designed by means of adding only steel boards to the inside wall and ceiling of the room. The results endorse the “calculation manual” which has not expounded to bremsstrahlen and photoneutron generated in steel boards by electron irradiation.

References

1) Nuclear Safety Technology Center: Manual of Practical Shield Calculation of Radiation Facilities, Nuclear Safety Technology Center, Tokyo, 2000.

2) D.W.O. Rogers, B.A. Faddegon, G. X. Ding, *et al.*: BEAM: A Monte Carlo code to simulate radiotherapy treatment units, Med. Phys. 22, 503-524, 1995.

3) M. J. Berger and S. M. Seltzer: Stopping power and ranges of electrons and positrons, NBS Report, NBSIR, 82-2550-A (second edition), 1983.

4) Seltzer, S.M.: Calculation of Photon Mass Energy-Transfer and Mass Energy-Absorption Coefficients, Rad. Res. 136**,** 147-170, 1993.

5) Y.-O. Lee: Photonuclear Data File (PDF) of the JENDL Library, private communication, 1999

6) ICRU: Neutron Dosimetry for Biology and Medicine, ICRU Report 26, Washington, International Committee on Radioactive Units and Measurements, 1977.